INAUGURAL - DISSERTATION
zur
Erlangung der Doktorwürde
der
Naturwissenschaftlich-Mathematischen
Gesamtfakultät
der
Ruprecht-Karls-Universität
Heidelberg

Vorgelegt von
Diplom-Mineraloge Christian Weikusat
aus: Eppelheim

Tag der mündlichen Prüfung: 16.04.2010

Modifications of natural minerals by irradiation with relativistic heavy ions with and without external pressure

Gutachter: Prof. Dr. Ronald Miletich-Pawliczek
Prof. Dr. Rainer Altherr

Und wovon man nicht sprechen kann, darüber muß man schweigen.
L.J.J. Wittgenstein

Erklärung

Hiermit erkläre ich, dass ich die vorgelegte Dissertation selbst verfasst und mich dabei keiner anderen als der von mir ausdrücklich bezeichneten Quellen und Hilfen bedient habe. Ich erkläre weiterhin, dass ich bei keiner anderen Stelle ein Prüfungsvorhaben beantragt habe, dass ich die Dissertation nicht in dieser oder anderer Form anderweitig als Prüfungsarbeit verwendet habe und dass ich sie an keiner anderen Fakultät als Dissertation vorgelegt habe.

Eppelheim, 18.02.2010

Contents

Summary

Irradiations with swift heavy ions have been performed using different crystalline target materials and various pressure and irradiation conditions. Changes in the crystal lattice, *e.g.* the production of point defects and amorphisation, have been characterised by Raman spectroscopy.
The cordierite lattice is very resistant against radiation-induced damage, while the amount of volatile phases in the structural channels is significantly changed. Furthermore, a direct conversion from CO_2 to CO could be evidenced. Irradiations along the different crystallographic axes did not yield sytematic differences regarding the monitored parameters.
In contrast to cordierite, apatite is substantially more sensitive to radiation damage. With increasing fluence, the overall amount of amorphisation increases. However, even for the highest fluences, complete amorphisation could not be achieved. Irradiations along the different crystallographic axes show larger amounts of damage for samples irradiated parallel (0001). The application of external pressure during irradiation stabilises the lattice and can prevent amorphisation.
The suitability of large-volume Paris-Edinburgh presses for in-situ irradiation with swift heavy ions could be proven.

Zusammenfassung

Unterschiedliche kristalline Materialien wurden mit schnellen Schwerionen unter verschiedenen Druck- und Bestrahlungsbedingungen bestrahlt. Die Veränderungen im Kristallgitter, wie z.B. Entstehung von Punktdefekten und Amorphisierung, wurden mittels Ramanspektroskopie untersucht.
Die Kristallstruktur des Cordierits ist sehr beständig gegenüber Strahlenschäden, wohingegen sich Gehalt und Art der volatilen Phasen in den strukturellen Kanälen durch die Bestrahlung signifikant ändern. Desweiteren konnte eine direkte Umwandlung von CO_2 nach CO nachgewiesen werden. Bestrahlungen entlang der verschiedenen kristallografischen Achsen zeigten keine systematischen Unterschiede bezüglich der betrachteten Parameter.
Im Gegensatz zu Cordierit ist Apatit deutlich empfindlicher gegenüber Strahlenschäden. Der Grad der Amorphisierung steigt mit steigender Fluenz. Allerdings konnte keine vollständige Amorphisierung erreicht werden, auch nicht für die höchsten Fluenzen. Bestrahlungen entlang der verschiedenen kristallografischen Achsen zeigten generell stärkere Schäden bei Bestrahlung parallel (0001). Die Anwendung externen Drucks während der Bestrahlung stabilisiert das Kristallgitter und kann die Amorphisierung verhindern.
Die Tauglichkeit von Paris-Edinburgh Pressen für die in-situ Bestrahlung mit schnellen Schwerionen wurde bewiesen.

List of Publications Submitted for this Thesis

- Publication I (Appendix A)

  Raman spectroscopy of heavy ion induced damage in cordierite

  C. Weikusat, U.A. Glasmacher, R. Miletich, R. Neumann, C. Trautmann (2008)

  Nuclear Instruments and Methods in Physics Research Section B, Vol. 266, Issues 12-13, pp. 2990-2993.

  own contributions:

  - Orientation and preparation of the samples
  - Preparation and conduction of the irradiation experiments at GSI
  - Development of a technique for depth-resolved linescans
  - Acquisition, analysis and interpretation of the Raman spectra
  - Preparation of the manuscript for publication

- Publication II (Appendix B)

  Heavy-ion irradiation on crystallographically oriented cordierite and the conversion of molecular CO_2 to CO: a Raman spectroscopic study

  C. Weikusat, R. Miletich, U.A. Glasmacher, C. Trautmann, R. Neumann (2009)

  Physics and Chemistry of Minerals, doi:10.1007/s00269-009-0343-x.

  own contributions:

  - Orientation and preparation of the samples
  - Preparation and conduction of the irradiation experiments at GSI
  - Acquisition, analysis and interpretation of the Raman spectra
  - Preparation of the manuscript for publication

- Publication III (Appendix C)

  Experimental heavy-ion irradiation in the Paris-Edinburgh press: first results (*abstract*)

  C. Weikusat, M. Burchard, S. Klotz, R. Miletich, U.A. Glasmacher, C. Trautmann, R. Neumann

  International Conference on High Pressure Science and Technology
  Joint AIRAPT-22 & HPCJ-50, Odaiba, Tokyo, JAPAN
  Review of High Pressure Science and Technology, Vol. 19

  own contributions:

  - Preparation and conduction of the irradiation experiments at GSI
  - Acquisition, analysis and interpretation of the Raman spectra
  - Preparation of the abstract
  - Preparation and performance of an invited talk at *Joint AIRAPT-22 and HPCJ-50*, Tokyo, Japan

- Publication IV (Appendix D)

  Raman study of apatite amorphised with swift heavy ions under various irradiation conditions

  C. Weikusat, U.A. Glasmacher, R. Miletich, B. Schuster, C. Trautmann, R. Neumann (submitted February 2010)

  Submitted to Physics and Chemistry of Minerals, January 2010.

  own contributions:

  - Loading of the samples into Diamond Anvil Cells
  - Preparation and conduction of the irradiation experiments at GSI
  - Acquisition, analysis and interpretation of the Raman spectra
  - Preparation of the manuscript for publication

- Publication V (Appendix E)

  Lattice compression and structural behavior of $NaVSi_2O_6$ clinopyroxene to 11 GPa

  A. Ullrich, R. Miletich, F. Nestola, C. Weikusat, H. Ohashi (2009)

  American Mineralogist, Vol. 94, pp. 557-564.

  own contributions:

  - Assistance with acquisition and interpretation of the Raman spectra
  - Help with preparation of the related chapter of the publication

Confirmation of author's contribution

It is confirmed, that C. Weikusat's contribution to the papers presented in this thesis is true, accurate and justified.

Prof. Dr. Ronald Miletich-Pawliczek

Dipl. Phys. Beatrice Schuster

Acknowledgement

I thank my supervisors, Apl. Prof. Dr. Ulrich A. Glasmacher and Prof. Dr. Ronald Miletich-Pawliczek for the possibility to write this PhD thesis. I also thank Prof. Dr. Rainer Altherr for agreeing to referee this thesis. Furthermore, many thanks go to the Materials Research group at the GSI Helmhotz center for Heavy Ion research, especially to Robert Klein, Markus Krause, Elko Schubert and Bea Schuster. Thomas Pippinger and Pascal Schouwink of the mineral physics section of the University of Heidelberg are thanked for the nice times at the office.
I express my deepest gratitude to my families, especially to my parents. Without your long-standing support, this work would not have been possible.
Last and most, I thank my wife Ilka for absolutely everything.

1

Background and motivation

Irradiations with the high-energetic swift heavy ions available from modern accelerator facilities provide unique possibilities for creating extremely high energy densities inside various targets. The study of the changes caused by such experiments gives unprecedented insights into basic physical properties of the irradiated substances.

Besides being extensively used in many fields of physics, this method has also become more and more important in materials research. Problems such as the urgent need for materials capable of inactivating radioactive wastes or, in geoscience, the analysis and prediction of nuclear tracks forming inside actinide-bearing minerals (*e.g.* apatite or zircon) have benefitted from experiments with swift heavy ions. The latter has also motivated experiments combining swift heavy ion irradiation with the high pressures available from modern pressure generating technologies, such as diamond anvil cell techniques. The need for larger sample volumes, that are essential for many types of analytical methods, has led to the very first irradiation experiments using large-volume Paris-Edinburgh presses, which had hitherto mainly been used for neutron scattering.

All of these experiments require suitable and reliable methods for a characterisation of the radiation-induced changes of the sample. Raman spectroscopy, a non-destructive and very versatile spectroscopic technique, is a fast and easy method for such investigation and can be applied to a wide range of gaseous, liquid and solid materials.

2

Introducing the Minerals

2.1 Cordierite

The mineral cordierite, $(Mg,Fe)_2Al_4Si_5O_{18} \cdot n(H_2O,CO_2,\ldots)$, is a common product of regional- or contact metamorphosis, but can also occur in various igneous rocks. The structure consists of six-membered rings of corner-sharing $(Si,Al)O_4$ tetrahedra. The rings are stacked along the c axis and are connected by further corner-sharing $(Si,Al)O_4$ tetrahedra, forming a continouus framework. Besides replacing Si in the tetrahedra, aluminium also exists in octahedral coordination, which makes cordierite a member of the alumosilicate group. At room temperature, $^{[4]}$Al concentrates in the $T_2 6$ positions in the $(Al,Si)_6O_{18}$ rings (*cf.* Fig. 2.1) and the $T_1 1$ positions in the linking chains, resulting in orthorombic symmetry (*Cccm*, $a > b > c$). Above a temperature of ∼500 °C, depending on the iron content, the distribution of Al and Si starts to change until it becomes completely stochastic (*e.g.* Kitamura and Hiroi, 1982). The resulting high-temperature phase (*indialite*) has hexagonal symmetry *P6/mcc* and is isostructural with beryll. The mechanisms and dynamics of this phase transition have been studied by a wide variety of analytical methods (*e.g.* Mirwald, 1982; Gibbs, 1966; Armbruster and Bloss, 1981; Putnis, 1980; Putnis et al., 1987; Salje, 1987; Güttler et al., 1989; Poon et al., 1990, *and references therein*).

The resulting continouus channels form rather large cavities between the rings (d ∼6 Å). The ′bottlenecks′ of the channels can be occupied by alkali cations (*e.g.* Na, K), which are centered in the rings at $0, 0, 0$. The cavities can be host for various volatile components (*e.g.* H_2O, CO_2, CO, N_2, Ar, hydrocarbons, etc.), where each cavity contains a single molecule. The location and behaviour of the volatiles is dependent on the content of alkali atoms in the channels. Nature and concentrations of these channel constituents, as well as the interactions between them, have been subject to a large number of studies (*e.g.* Goldmann and Rossman, 1977; Armbruster and Bloss, 1982; Aines and Rossman, 1984; Armbruster, 1985; Kolesov and Geiger, 2000; Kaindl et al., 2006). The volatiles are usually

incorporated during crystal growth. Analysis of these channel constituents can therefore yield valuable information about fluid evolution during metamorphism and anatexis (*cf.* Vry et al., 1990; Santosh et al., 1993, *and references therein*). It has also been shown, that volatiles can be inserted into the channels by the application of external pressure (*e.g.* Johannes and Schreyer, 1981).

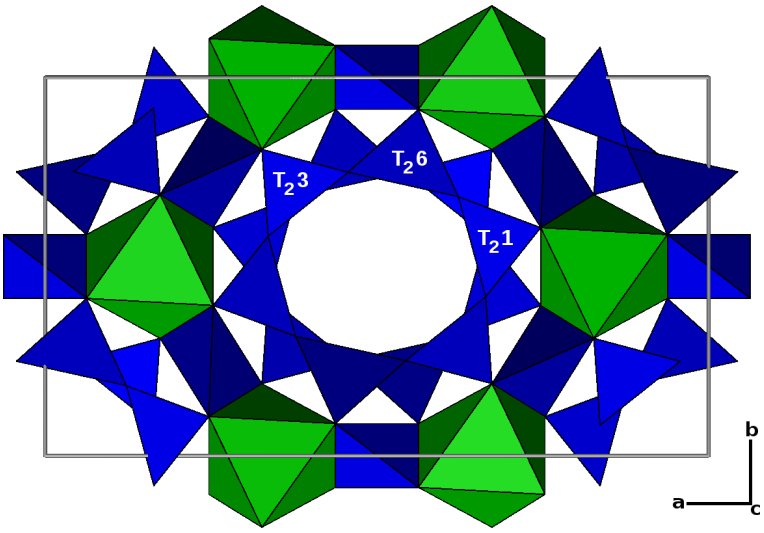

Figure 2.1: Cordierite viewed along the c-axis. Denomination of the tetrahedra after Armbruster and Bloss (1982)

Apart from structural investigations and the analysis of channel components, cordierites have also received considerable attention due to their remarkable optical and mechanical properties. Their intense blue/violet colouration and macroscopically visible distinct pleochroism have not only made cordierite a much coveted and valuable material for the gem and mineral market (trade name *Iolith*), but have also sparked scientific interest in their origin. In this context, the possiblity of the existence of iron in different charge states and according intervalence charge transfer processes have gained much attention. While most of the iron in cordierites is Fe^{2+}, the existence of minor amounts of three-valent iron has been confirmed by Mössbauer spectroscopy (*cf.* Parkin et al., 1977; Vance and Price, 1984; Geiger et al., 2000). The possible locations of Fe^{2+}/Fe^{3+} in the cordierite structure have been subject to various experimental and analytical investigations (*e.g.* Faye et al., 1968; Vance and Price, 1984; Geiger et al., 2000; Khomenko et al., 2001). The unusually strong pleochroism has also made cordierite a major candidate for the mythical *sunstones*, which supposedly enabled the Vikings to navigate their boats even through dense fogs by evaluating the skylight polarization (Hegedüs et al., 2007).

The unusual thermal properties of cordierites, *i.e.* the low thermal expansion

coefficients and the excellent resistance against thermal shock, make it a valuable material for the construction of various ceramic compounds (*e.g.* for catalytic converters or heat shielding).

Especially its great resistance to thermal shock makes cordierite a promising material to investigate under swift heavy-ion irradiation, which was one of the main topics of this work. As the traverse of swift heavy ions through matter can, at least to some extent, be described as a very localized production of immense heat (thermal spike, *cf.* Chap. 3.1), the reaction of cordierite to this process is very interesting.

2.2 Apatite

The minerals of the apatite group have the general chemical formula $Ca_5(PO_4)_3X$ (with X=*F,OH,Cl*). Depending on the type of anion in the X position, the endmembers are commonly termed fluorapatite, hydroxylapatite and chlorapatite respectively. Fluor- and hydroxylapatites usually have hexagonal symmetry $P6_3/m$ (*cf.* Fig. 2.2). The pure chlorapatite endmember should theoretically obtain only monoclinic symmetry ($P11\bar{2}_1/b$), but already very small amounts of fluor in the lattice lead to a macroscopically hexagonal crystal.

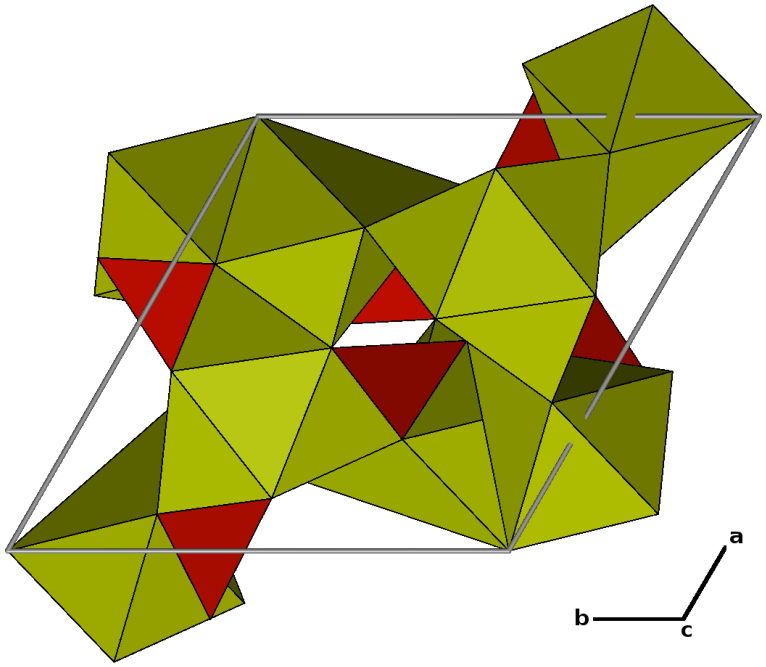

Figure 2.2: Polyhedral view of apatite along the c-axis. *red:* PO_4 tetrahedra, *green:* Ca polyhedra

Apatite has been subject to a plethora of investigations, because it is not only the main inorganic component in osseous tissue (*i.e.* teeth or bones), but also relevant for a wide variety of scientific and commercial fields, ranging from its importance in the global phosphorous cycle via the use of fission tracks inside the apatites for thermochronological dating (*e.g.* Wagner and van den Haute, 1992) to its role in the search for materials capable for the inactivation of radioactive wastes (*e.g.* Weber et al., 1998). The last mentioned applications derive from the apatite structure's ability to accomodate a wide variety of metal and heavy-metal cations, substituting for *Ca* (*e.g.* Sr, Ba, Y, REE, Pb, U, Th).

Thermochronology is an absolute dating method for the thermal history of rocks and is becoming increasingly important in the geosciences. Until very recently, many assumptions concerning the underlying processes, especially the production and recovery of nuclear tracks, could not be validated experimentally. The combination of high pressures and relativistic heavy ions gives exciting new possibilities for the scientific analysis of these processes and has therefore been part of this project (*cf.* App. D).

3

Experimental and Analytical Techniques

3.1 Relativistic Heavy Ions

The irradiation with relativistic heavy ions gives the possibility to create uniquely high energy densities in a controlled and strictly localized way. Besides the near-endless possibilities for particle physics (*e.g.* Kalmus, 1985; Gelletly, 2001, *and references therein*), it has long since become a valuable technique for materials science (*cf.* Conlon, 1985). For geoscience, especially the possibilities for experimental evaluation of fission-track production have gained increasing interest over the last years.

The term *relativistic* denotes ions with velocities close to the speed of light. For such particles, the classical mechanical and electro-dynamical models are no longer applicable and they have to be treated by relativistic calculations. As a matter of fact, for most of their trajectories they should not be considered as particles at all, but rather as energy waves.

An important parameter for the interaction of relativistic particles with matter is the differential energy loss dE/dx (also *stopping power*), which describes the amount of energy per unit-length that is transferred to the target material. The stopping power is dependent on many factors, including the velocity of the impinging ion as well as the mass and density of the target material. Two different regimes have to be taken into account (Fig. 3.1):

Electronic stopping The velocity of the incident ion is high enough, that it is not perceived as a discrete particle by the target atoms. This is the case for the major part of the ion trajectory. The ions can only interact with and transfer energy to the electronic system of the target. Electrons that have gained enough kinetic energies can leave their atoms and interact with their neighbours, releasing secondary electrons. The induced electron cascade couples to lattice vibrations and

the kinetic energy of the electrons is converted into atomic motion (heat). The heat is confined to a very small volume inside the crystal and leads to localized melting or even evaporation (*thermal spike*). Transfer of the heat to the cool lattice happens very fast, quenching the atomic disorder induced by melting. This results in clustered defects or amorphization along the ion track.

Nuclear stopping Approaching the end of its flight (the last few μm), the ion has been slowed down enough to directly interact with the nuclei of the target atoms. The kinetic energy of the ion is transferred to the nuclei by direct collisions and the resulting collision cascades. This leads to the production of interstitial atoms and lattice vacancies. Depending on the amount of disorder induced (measured in *displacements per atom (dpa)*), this can also lead to small-scale zones of complete amorphization.

The energy loss of a relativistic particle in solid matter can principally be calculated by the *Bethe-Bloch* formalism (Eq. 3.1)

$$-\frac{\mathrm{d}E}{\mathrm{d}x} = \frac{4\pi n z^2}{m_e c^2 \beta^2} \cdot \left(\frac{e^2}{4\pi\varepsilon_0}\right)^2 \cdot \left[\ln\left(\frac{2m_e c^2 \beta^2}{I \cdot (1-\beta^2)}\right) - \beta^2\right] \tag{3.1}$$

E	ion energy
x	length of the ion path
m_e	mass of the electron (9.109×10^{-31}kg)
c	speed of light (2.998×10^{8} m/s)
n	target electron density
z	charge of the ion
β	$\frac{v}{c}$
v	ion velocity
e	elementary charge (1.602×10^{-19}C)
ε_0	vacuum permittivity (8.854×10^{-12} C^2/Jm)
I	mean excitation potential of the target

where the electron density n of the target material can be derived from mass and density (Eq. 3.2). However, for a true treatment of all relativistic implications a lot of correction factors have to be applied which make the matter rather complicated. Furthermore, a full quantum-mechanical treatment of a complex composite system is not always possible. Therefore, an approach combining quantum-mechanical calculations, Monte Carlo simulations and experimentally determined tables for *e.g.* excitation potentials of different materials is used to predict energy losses, penetration depths and other parameters for the experiments. The standard tool for this type of predictions is the free software SRIM (Stopping and Range if Ions in Matter, Ziegler et al. (2008))(*cf.* Fig. 3.2).

$$n = \frac{N_A Z \varrho}{A} \tag{3.2}$$

N_A	Avogadro constant (6.022×10^{23} mol^{-1})
Z	atomic number of the target
ϱ	density of the target
A	mass number of the target

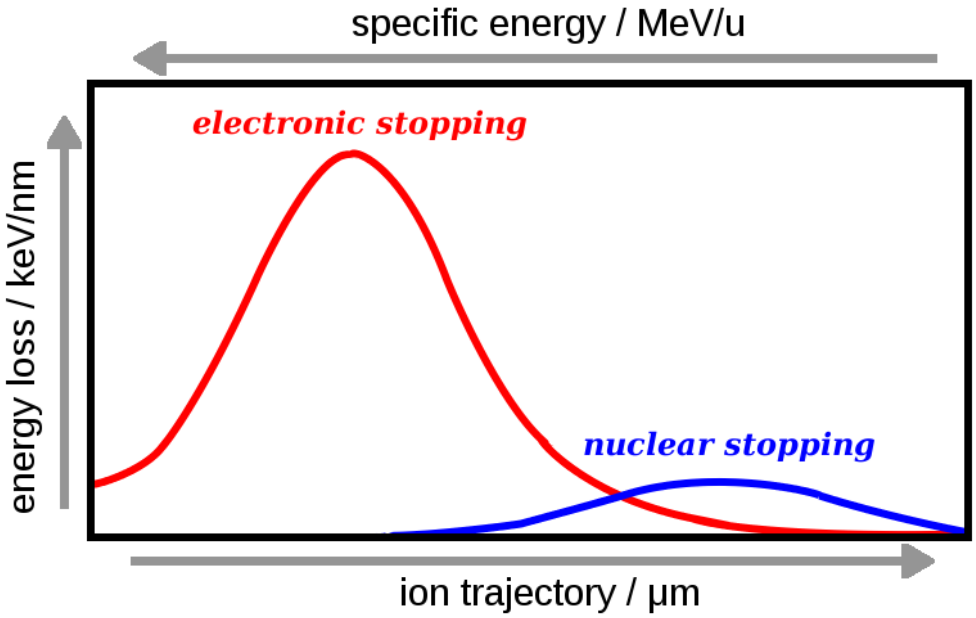

Figure 3.1: Schematic diagram of the relations of electronic and nuclear energy loss, ion energy and trajectory length. Grey arrows point towards higher values

3.2 High Pressure Techniques

3.2.1 Diamond Anvil Cell

The generation and use of high pressures for materials research and geosciences can be achieved by a wide variety of different techniques. For this work, diamond-anvil cells (DAC) have been used as the main device for pressure creation. The DAC was developed in the 1960s and combines the possibilities for pressure generation up to the multimegabar range with a unique manageability (Miletich et al.,

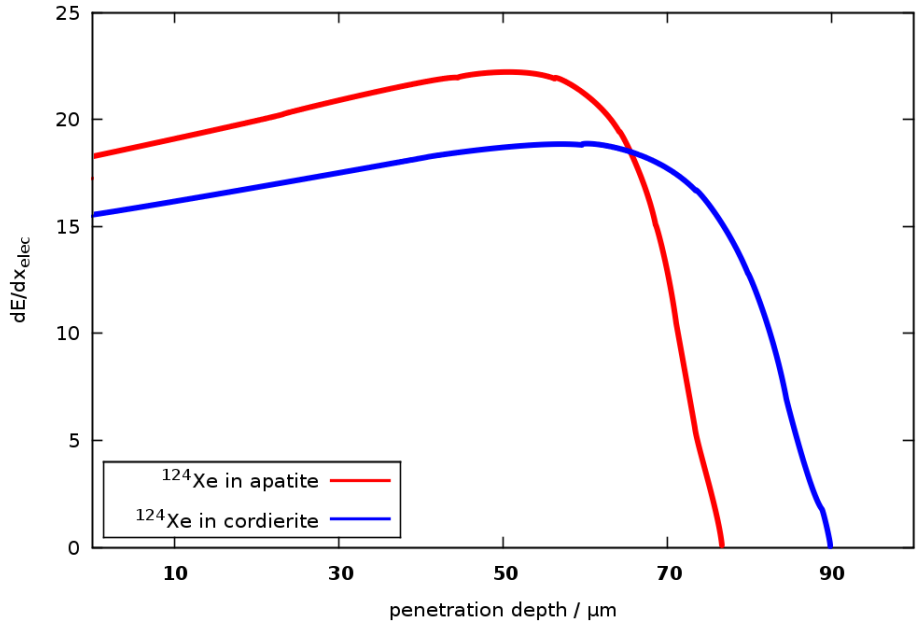

Figure 3.2: Electronic energy loss and penetration depths for ^{124}Xe ions (*initial energy:* 11 MeV/u) in different targets, calculated with SRIM2008 (Ziegler et al., 2008)

2000). For a sketch of the basic principles please see Figure 3.3. A metal foil (*e.g.* hardened steel, rhenium) is placed between the flat and parallel culet faces of two diamonds with a modified brilliant cut. This gasket is then pre-indented to provide stabilisation for the diamond tips, which, although being very hard, could easily break due to shearing forces. Inside this pre-indentation, a hole is drilled which represents the actual sample chamber (diameter ~200 μm, depending on culet size and aspired pressure). The sample is placed inside the sample chamber, together with some standard for pressure calibration (*e.g.* ruby or quartz) and the chamber is then filled with a pressure transmitting medium (*e.g.* methanol/ethanol/water mixtures, gasses like argon or solid media like NaCl or MgO). The choice of the pressure medium depends on the planned maximum pressure and the decision for hydrostatic or non-hydrostatic conditions.

The use of gem-quality diamonds (transparent for a wide range of electromagnetic radiation) as anvils enables the in-situ application of various analytical techniques. The possibility of spectroscopic measurements inside the pressurized sample chamber also enables the use of rubies for pressure calibration, monitoring the pressure-induced shifts of the ruby luminescence lines. This is a well established and extremely fast technique (*e.g.* Mao et al., 1986).

The feasibility of DACs for heavy-ion irradition under high-pressure conditions has first been shown by Lang et al. (2005). The diamond anvils are very resistant

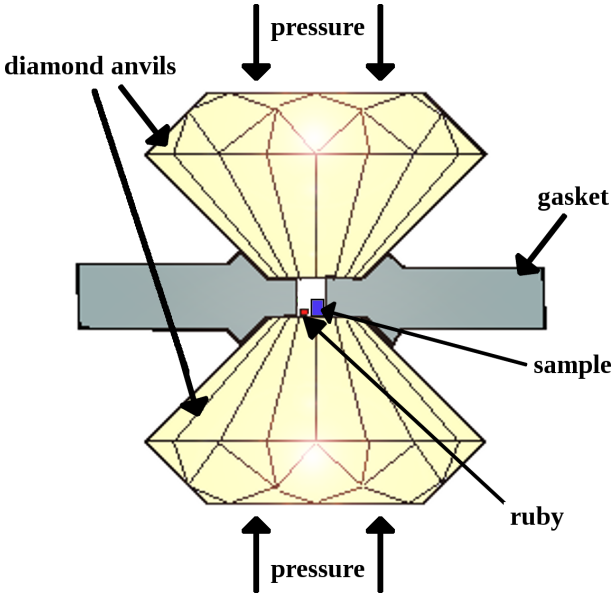

Figure 3.3: Basics of the diamond-anvil cell (DAC). The ruby chip is used for pressure calibration

against heavy-ion induced damage, yet they also show signs of increasing accumulation of point-defects: After several experiments, the diamonds develop a green colouration wich intensifies with increasing total fluence. The energy of the ions is usually calibrated so that the ions come to a stop inside the bottom diamond, thus assuring the maximum electronic energy loss inside the sample (*cf.* Chap. 3.1). The top diamond, which is traversed completely by the incident ions, is coloured homogeneously. Because the actual penetration depth into the bottom diamond is dependent on the experimental parameters, the bottom diamond shows a zonation of different shades of green after several experiments. This change in colour is probably connected to the production of vacancies and related defect centers (Weikusat, 2005, *and references therein*).

One major drawback of the diamond-anvil cells is the severe limitation of the sample volume. It demands prodigous skill and accuracy during loading and unloading of the cell lest the sample be lost. And even after succesful recovery of the sample, the available volumes are often too small, *e.g.* for any kind of destructive analysis. A pressure apparatus allowing the use of larger samples is therefore desirable.

3.2.2 Paris-Edinburgh Press

The Paris-Edinburgh press is a simple squeezer apparatus which has originally been developed for neutron scattering (*cf.* Besson et al., 1995; Klotz et al., 1996,

and references therein). It allows for sample volumes in the range of ∼100 mm^3 while applying pressures up to ∼12 GPa, dependent on the actual setup.

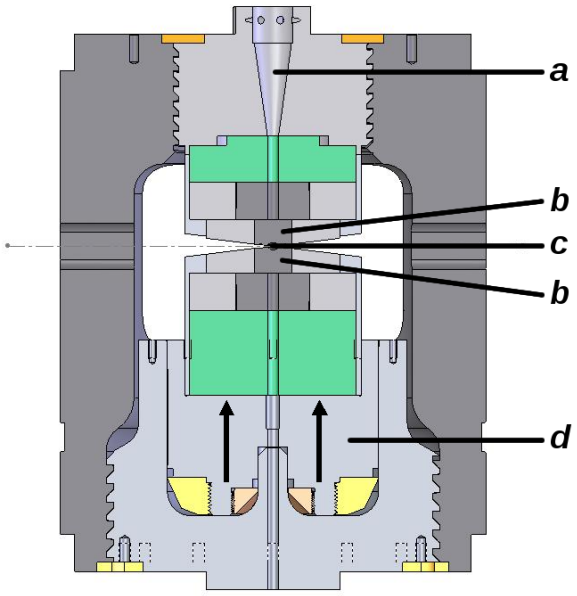

Figure 3.4: Schematic view of the VX4 Paris-Edinburgh press. *a*: irradiation channel, *b*: cBN anvils, *c*: sample chamber, *d*: hydraulic piston

For the irradiation experiments, we chose a model VX4 press (Fig. 3.4) with modified cubic boron nitride (cBN) anvils. cBN is the second hardest material after diamond, and both are isostructural. Sintered cBN also shows an excellent resistivity against heavy-ion induced damage (Klein, 2010). Yet it has a high-potential for radioactive activation, as the sintering process usually includes metallic binders with cobalt, which is known to be susceptible for activation. To reduce the amount of induced radioactivity of the press after the experiments (which could otherwise prevent the extraction of the samples for several months), the crossing of the relativistic ions through any materials of the gasket or anvils had to be minimized. The press was shielded and the cBN anvils were modified to provide the maximum free pathlength of the ions before entering the sample chamber.

3.3 Raman Spectroscopy

Raman spectroscopy is a non-destructive method for the analysis of vibrational states of gasses, liquids and solid matter. The Raman effect, describing the inelastic scattering of light in matter, has been postulated in 1923 (Smekal, 1923) and was experimentally observed for the first time in 1928 (Raman and Krishnan, 1928).

When light hits matter, it interacts with the electrons of the target atoms. If the energy of the incident light matches the energy of an electronic transition, an electron is transferred to the excited state and the light of this frequency is absorbed. This is the case for IR spectroscopy, with frequencies ranging from $10^{12} - 10^{14}$ Hz. If no absorption occurs, the electron cloud of the target atom is distorted by the incoming wave and, upon relaxation, re-emits diffuse light with the same frequency as the incident light (elastic or *Rayleigh* scattering, $\omega = \omega_0$). This normal case is also responsible for the blue colour of the sky. In some rare cases however, the induced distortion of the electron cloud can interact with a motion of the atomic nucleus. Energy is transferred and the frequency of the scattered light is changed (inelastic or *Raman* scattering). Two cases are possible:

1. Energy is transferred from the incident light to the nucleus, creating a vibrational phonon. This is called the *Stokes scattering* ($\omega = \omega_0 - \omega_{vib}$).

2. Energy is transferred from the already moving nucleus to the scattered light, a vibrational phonon is destroyed (*anti-Stokes scattering*, $\omega = \omega_0 + \omega_{vib}$).

For both cases, ω_{vib} represents the difference in energy between two vibrational states of the molecular or structural group. A necessary precondition for *anti-Stokes* scattering is the existence of molecular or structural groups that are already in an excited state. The ratio of ground state to excited state (and thus the ratio of *Stokes-* and *anti-Stokes* scattering) can be calculated by the Boltzmann equation:

$$\frac{N_n}{N_m} = \frac{g_n}{g_m} \exp\left[\frac{-(E_n - E_m)}{k_B T}\right] \tag{3.3}$$

N_n	number of molecules in the excited state (n)
N_m	number of molecules in the ground state (m)
g	degeneracy of states n and m
$(E_n - E_m)$	difference between the vibrational energy levels
k_B	Boltzmann constant (1.3807×10^{-23} JK^{-1})
T	temperature in Kelvin

It is immediately obvious, that *Stokes* scattering is the dominant process at normal conditions and that the amount of *anti-Stokes* scattering increases with rising temperature. It is actually possible to use experimentally determined ratios as a temperature probe, but this is tedious work and only possible for a well-known and thoroughly calibrated system.

Raman spectroscopy provides information about vibrational energy levels of a molecule or structural group. A vibration is Raman-active, if it includes a change of the polarizability tensor of the molecule or structural group. The number and type

of possible vibrations for a given system can be calculated using group theory. An in-depth treatment of group theory and the selection rules which make a vibrational mode Raman-active is beyond the scope of this thesis. The reader is refered to the plentifully available literature (*e.g.* Lewis and Edwards, 2001; Smith and Dent, 2005, *and references therein*).

The vibrational modes are usually referred to by their energies given as wavenumbers

$$\overline{\nu} = \nu_{vib}/c \tag{3.4}$$

where ν_{vib} is the frequency of the vibration and c is the speed of light. $\overline{\nu}$ is directly obtainable from the Raman spectrum as the shift of the scattered light (Fig. 3.5).

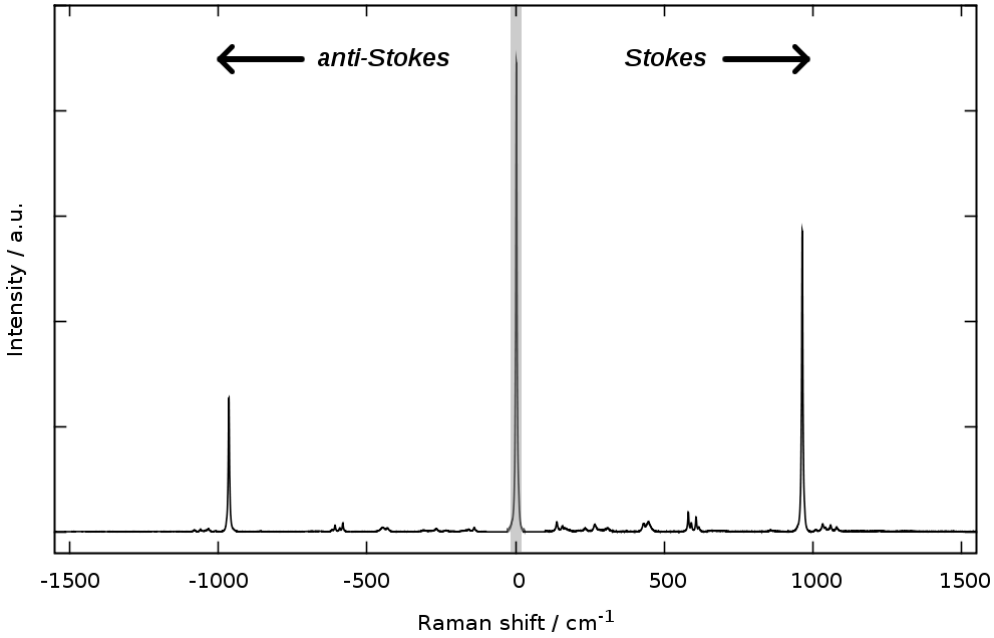

Figure 3.5: Sketch of a typical Raman spectrum. The grey area at *0* shows the *Rayleigh* scattering. Intensity ratios between *Rayleigh*, *Stokes* and *anti-Stokes* scattering are not to scale.

In geoscience, Raman spectroscopy has mainly been used as a tool for fast fingerprint analyses of mineral phases. For anisotropic (*i.e.* non-cubic) structures, the number, intensity and width of the various Raman bands is strongly dependent on crystal orientation relative to the field vectors of the incident laser (*cf.* Figs. 3.6 and 3.9). Therefore, the use of samples cut in well-known orientations is a mandatory prerequisite for a sensible comparison of spectra taken from different samples.

Raman spectroscopy can also be used for *in-situ* measurements of pressurized samples (*e.g.* Ullrich et al., 2009, *cf.* App. E). When measuring inside the DAC, the laser has to pass the top diamond twice, losing intensity on each way. Significantly

increased accumulation times and stronger background luminescence are the direct consequence of this. While this may still be acceptable for strong Raman scatterers, *e.g.* apatite, it can effectively prevent the acquisition of spectra from minerals such as cordierite, which already require much higher accumulation times in the first place.

3.3.1 Spectrum of cordierite

An unambigous assignment of the Raman bands to specific lattice vibrations has not yet been achieved. Nonetheless, a few authors have made sensible assumptions based on considerations and analysis of other minerals containing silicate rings (*e.g.* McMillan et al., 1984; Poon et al., 1990; Łodziński et al., 2005).

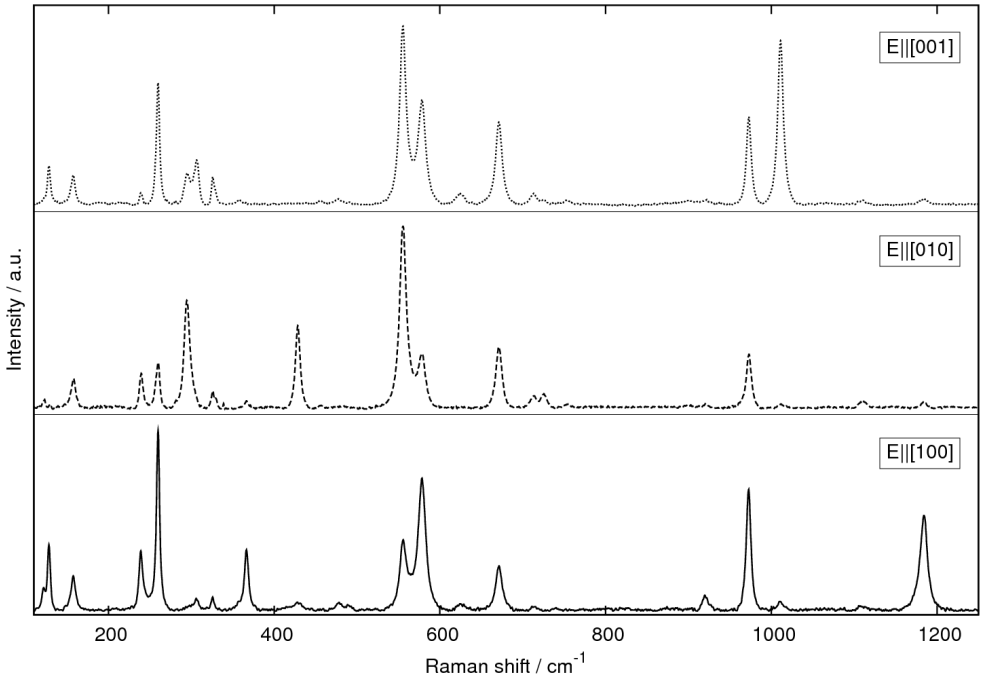

Figure 3.6: Raman spectra of oriented cordierite with the electric field vector of the incident laser polarized parallel to the crystallographic *a* (*bottom*), *b* (*middle*) and *c* (*top*) axis respectively

Channel constituents

Most of the volatile phases inside the structural channels of cordierite can be identified by Raman spectroscopy. Single gas molecules fit conveniently into the large cavities along the channels, so that the Raman modes can be interpreted

as slightly modified versions of the basic vibrational modes of the free gas phases (Fig. 3.7).

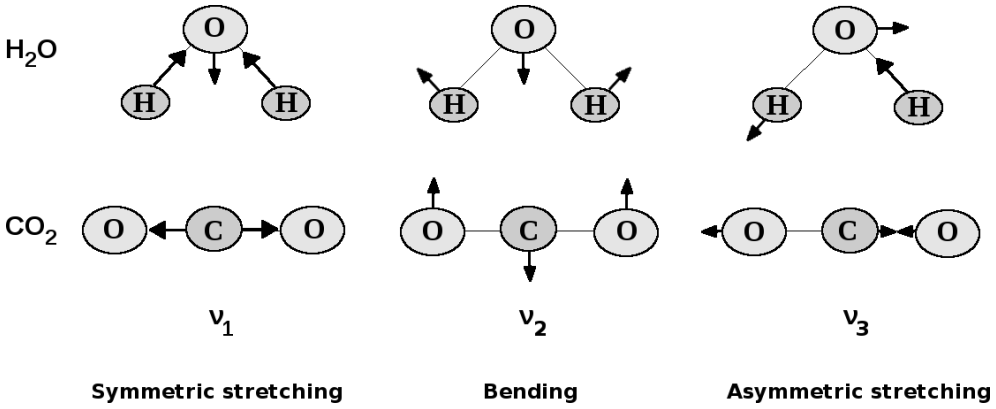

Figure 3.7: Fundamental vibrational Raman modes for H_2O and CO_2 (after Smith and Dent, 2005, *modified*)

The H_2O molecules can have different types of orientation, depending on the presence of alkali atoms in the center of the rings (Fig. 3.8). Each of these types can be identified from the Raman spectrum (*e.g.* Armbruster and Bloss, 1982; Kolesov and Geiger, 2000).

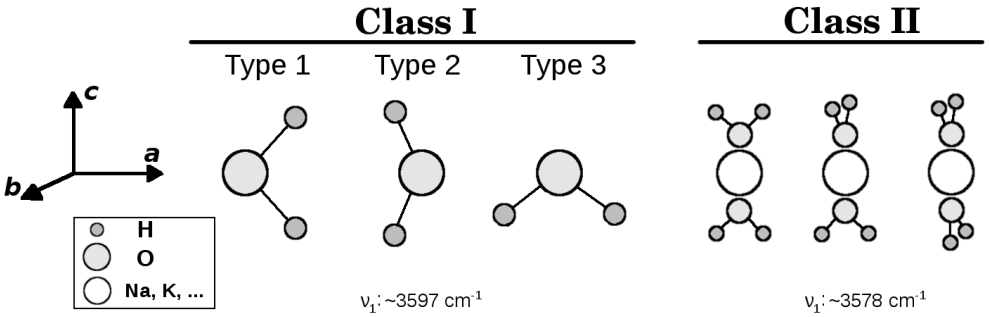

Figure 3.8: Orientations of H_2O in cordierite channels and wavenumbers of the respective Raman modes (after Kolesov and Geiger, 2000, *modified*)

For CO_2, there have also been attempts on a quantitative Raman analysis. Kaindl et al. (2006) developed a semi-quantitative method, where the CO_2 contents are calibrated against the ratios of bands related to SiO_4 vibrations. This method seems to work well for most natural cordierites. However, as heavy-ion irradiation changes the intensities of the bands (*cf.* Chap. 4.1), this approach might lead to biased results for irradiated samples.

3.3.2 Spectrum of apatite

The Raman spectrum of apatite is better understood by far than the spectrum of cordierite. Raman spectra of apatites have been investigated by researchers from many different fields of science (*e.g.* Kravitz et al., 1968; Boyer and Fleury, 1974; Tsuda and Arends, 1994; Williams and Knittle, 1996; Penel et al., 1998; Comodi et al., 2001; Liu et al., 2008).

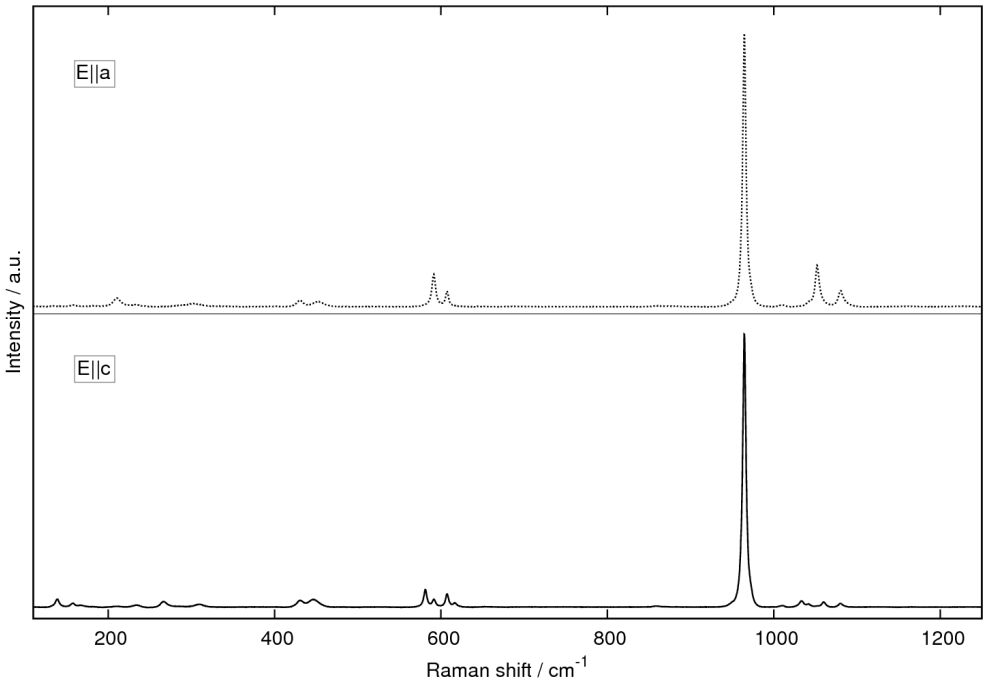

Figure 3.9: Raman spectra of oriented apatite with the electric field vector of the incident laser polarized parallel to the crystallographic c (*bottom*) and a (*top*) axis respectively

The most prominent features in the Raman spectra of apatite are related to vibrations of the PO_4 tetrahedra. The bands can be attributed to the following phonon modes: ∼964 cm^{-1} to the ν_1 symmetric stretching vibration of phosphate anions (this is the most intense mode in the apatite spectrum, cf. Fig. 2), ∼430 and ∼453 cm^{-1} to the ν_2 symmetric out-of-plane bending modes, ∼1052 and ∼1081 cm^{-1} to the ν_3 antisymmetric stretching modes, and ∼591 and ∼608 cm^{-1} to ν_4 antisymmetric bending (e.g. Comodi et al. 2001). The very weak bands below 400 cm^{-1} are most probably related to lattice modes.

3.3.3 Depth profiling with linescans

The use of a confocal system for Raman spectroscopy gives the possibility for measurements inside sufficiently transparent samples. While it would be very desirable to use this capability for depth-resolved linescans, it is unfortunately not straightforward. If the exact depth inside the sample is required, one has to account for various optical effects, especially the differences in refraction indices between objective, air and sample. The use of special objectives and immersion liquids can solve these problems, but their applicability critically depends on shape and surface constitution of the sample.

A new method, which was developed during this project, may help in cases, where the above mentioned protocols can not be used. The only requirement is a sample with two, preferably polished, sides that are perpendicular to each other. One of these sides is then irradiated. It is important to ensure a homogeneous dose distribution across the surface. Subsequently, the sample is tilted by 90°, and the linescans are carried out on the non-irradiated side, starting at the irradiated surface (*cf.* Figure 3.10). Given a well-calibrated automated sample stage, this method enables the acquisition of accurate depth profiles with resolutions on the micrometer scale (Weikusat et al., 2008, 2009b, *cf.* App. A and B). While the concept of this method is rather simple, experience shows that it nonetheless bears a great potential for misunderstandings.

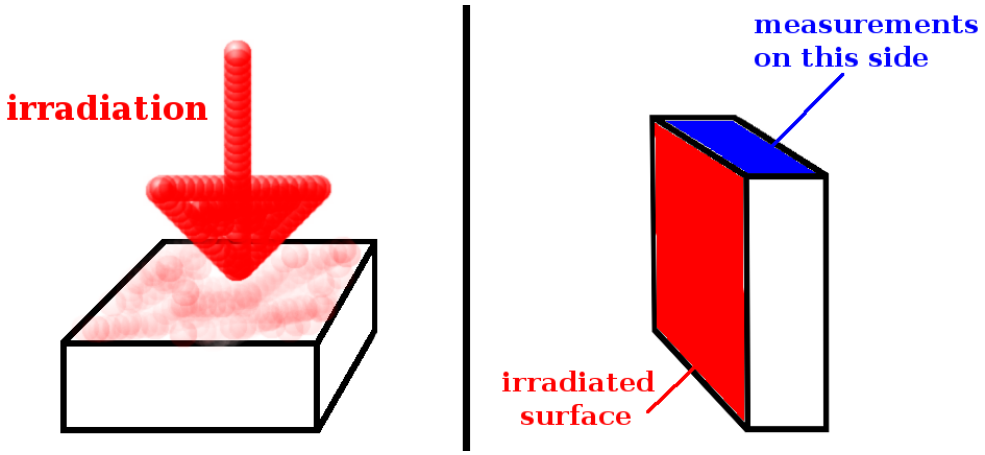

Figure 3.10: Sketch of the technique for depth-profiling with linescans. One surface is irradiated (*left*), the sample is tilted by 90°, linescans are carried out on the non-irradiated side, starting from the irradiated surface (*right*)

4

Results

4.1 Irradiation of Cordierite

The most obvious macroscopic effects of heavy-ion irradiation on cordierite are the development of cracks perpendicular to the irradiation direction and a significant change in colour (see Fig. 4.1). While the pristine cordierites used for these studies exhibit an intense deep-blue colour, the irradiated specimen are brownish-yellow. This effect is visible in each of our irradiated samples and becomes more distinct with increasing fluence. Regarding the Raman spectra, the intensities of the Ra-

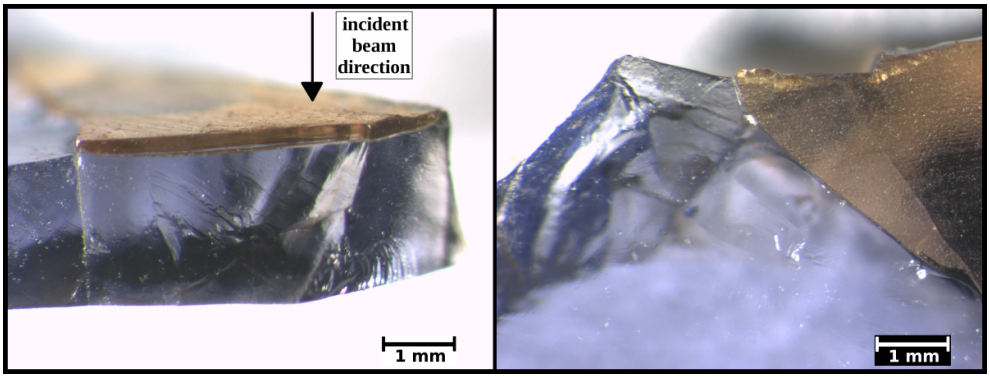

Figure 4.1: Changes in the macroscopic appearance of cordierite after irradiation with 1×10^{12} Xe ions (energy 1.465 GeV). A distinct colour change as well as cracking and chipping perpendicular to the incident beam are clearly visible. The width of the discoloured layer is a good estimate of the penetration depth of the ions.

man modes decrease while the widths of the bands increase with increasing fluence (Fig. 4.1). While these trends are visible and show clearly after mathematical fit-

ting of functions to the peaks (Weikusat et al., 2008, 2009b, *cf.* App. A and B), they are almost neglectable when compared to the huge changes in crystallinity seen for other minerals (*e.g.* apatite, Chap. 4.2).

Even at the highest fluences achieved during my experiments (2×10^{12} ions/cm^2), the main bands are still distinguishable and the broadening of the full-width-at-half-maximum ($FWHM$) remains quite moderate. This proves the extraordinary stability of cordierites under heavy-ion irradiation.

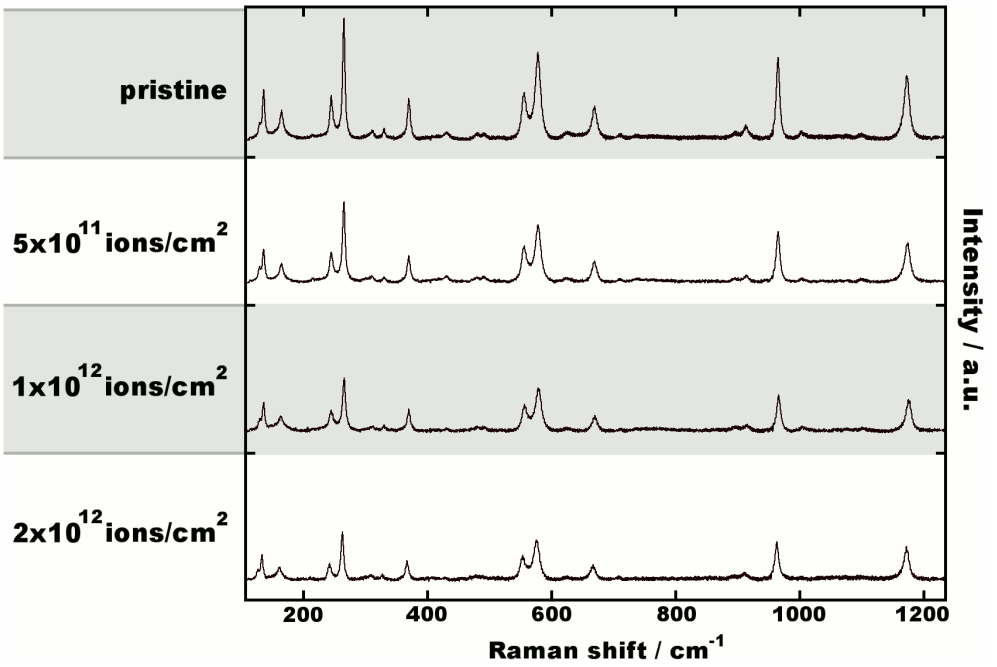

Figure 4.2: Raman spectra of oriented cordierite, irradiated parallel to [100] with different fluences of Pb ions (energy 1.6 GeV). (Weikusat et al., 2009b, *cf.* App. B)

While the temperatures during the thermal part of the energy transfer process should be high enough to induce reordering of Si and Al, none of the samples investigated during this project showed signs of a phase transition to the high-temperature phase.

4.1.1 Channel Volatiles

On evaluation of the data gathered from the first experiment, significant changes in the amount and composition of the channel volatiles became obvious (Weikusat et al., 2008). The concentration of the main components in our cordierites (*i.e.* CO_2 and H_2O) had decreased dramatically, while a weak new band appeared at

$\sim$2135 cm^{-1}, which is not detectable in any of the pristine samples. This band reveals the presence of single CO molecules in the channels, which must have developed from former CO_2 molecules. A conversion of CO_2 to CO is not achievable in heating experiments (*cf.* Aines and Rossman, 1984), but had previously been identified in the damaged halos around radioactive inclusions in natural cordierites (Nasdala et al., 2006).

The samples used in the first experiment were unoriented, which makes the comparison of spectra from different samples or even different areas of the same sample rather difficult. Therefore, only crystallographically oriented samples were used for all subsequent irradiations. An in-depth analysis of the data gained from the oriented samples shows distinct correlations between the amounts of channel volatiles and the electronic energy loss of the relativistic ions (Fig. 4.3).

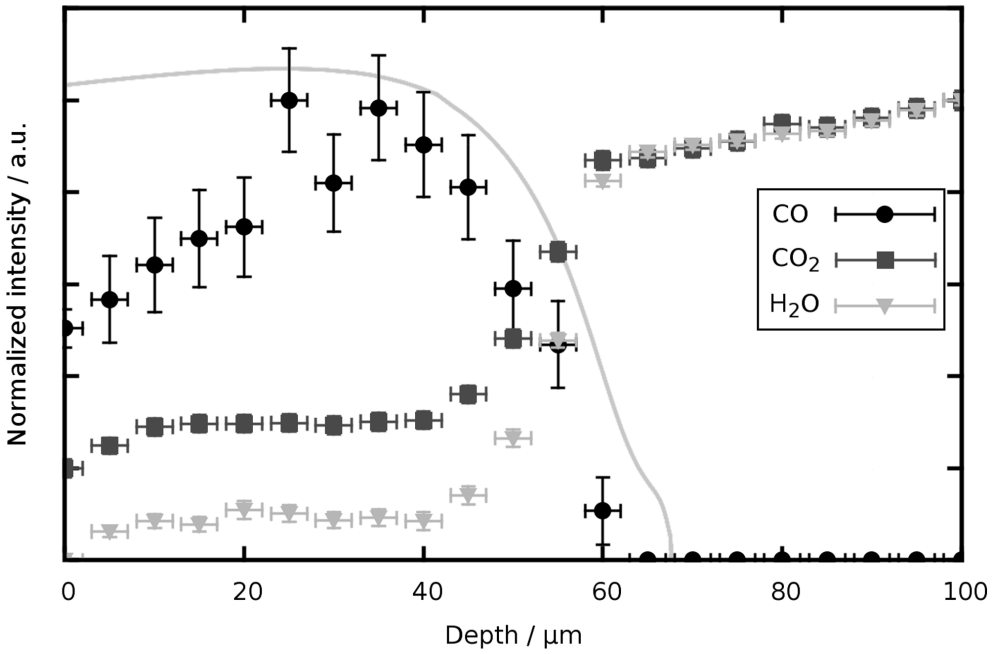

Figure 4.3: Normalised intensity of the symmetric stretching modes of CO (2135 cm^{-1}), CO_2 (1382 cm^{-1}) and class I H_2O (3198 cm^{-1}) as a function of depth (distance from the irradiated surface). The trends are similar for all fluences and orientations. The sample (CORMB1) was irradiated with 1 $\times$ 10^{12} Pb ions/cm^2 (energy 1.6 GeV). *Solid line* Electronic energy loss dE/dx of the ions calculated with SRIM2008. (Weikusat et al., 2009b, *cf.* App. B)

The conversion of CO_2 to CO produces excess oxygen. Single O molecules may diffuse into the lattice forming point defects (*interstitials*). These defects would probably contribute to the increase of luminecence background, which is also correlated to the electronic energy loss of the relativistic ions (Weikusat et al.,

2009b). On the other hand, the production of O_2 molecules from free oxygen radicals seems rather likely. Molecular oxygen can also be detected by Raman spectroscopy. However, the characteristic band at 1550 cm^{-1} can not be detected in any of our irradiated samples.

4.2 Irradiation of Apatite with and without Pressure

The changes in the apatite lattice after irradiation with heavy ions are much more pronounced than for cordierite. In addition to the broadening and decreasing intensity of the bands, a new broad band at ∼950 cm^{-1} appears and grows with increasing fluence (Fig. 4.4). This ν_{1b} band results from amorphous domains inside the lattice, most probably the cores of the induced ion tracks (*cf.* Liu et al., 2008; Schouwink et al., 2009). Irradiations with different ions (and thus different energy

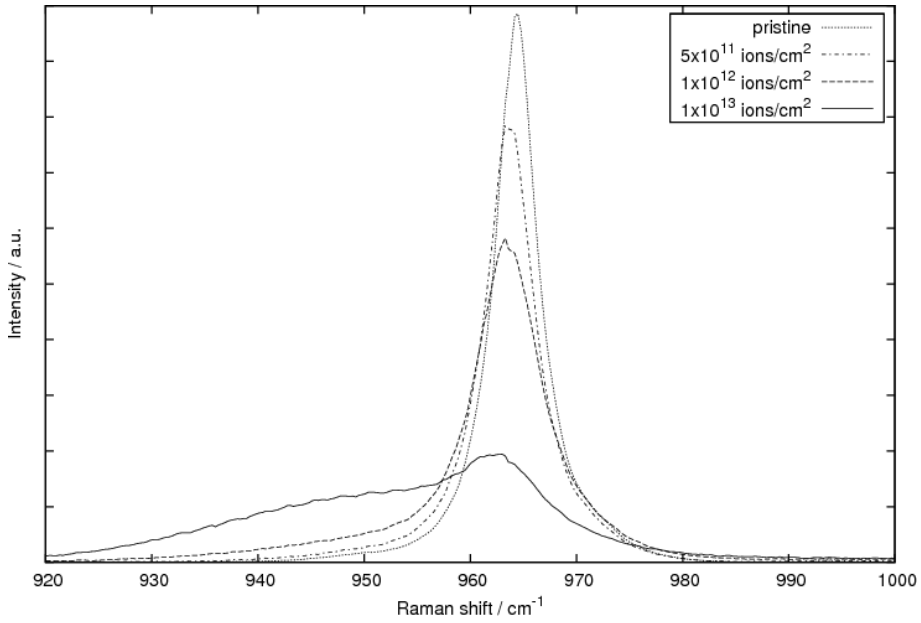

Figure 4.4: Changes of the 964 cm^{-1} band and the radiation-induced amorphous broad band at ∼950 cm^{-1} of apatite irradiated with different fluences of Xe ions ($dE/dx_0 \approx 18\ keV/nm$) (Weikusat et al., 2010, *cf.* App. D)

loss dE/dx_0, *cf.* Chap. 3.1) show that the amount of amorphisation scales not only with fluence, but also the electronic energy loss (Fig. 4.5). Liu et al. (2008) irradiated apatites with uranium ions ($\frac{dE}{dx} = 34keV/nm, 8 \times 10^{12}$ ions/cm^2), However, even the samples irradiated with the highest energy loss and fluence (34 keV/nm, $8{\times}10^{12}$ ions/cm^2, *cf.* Liu et al., 2008) are not completely amorphised and their

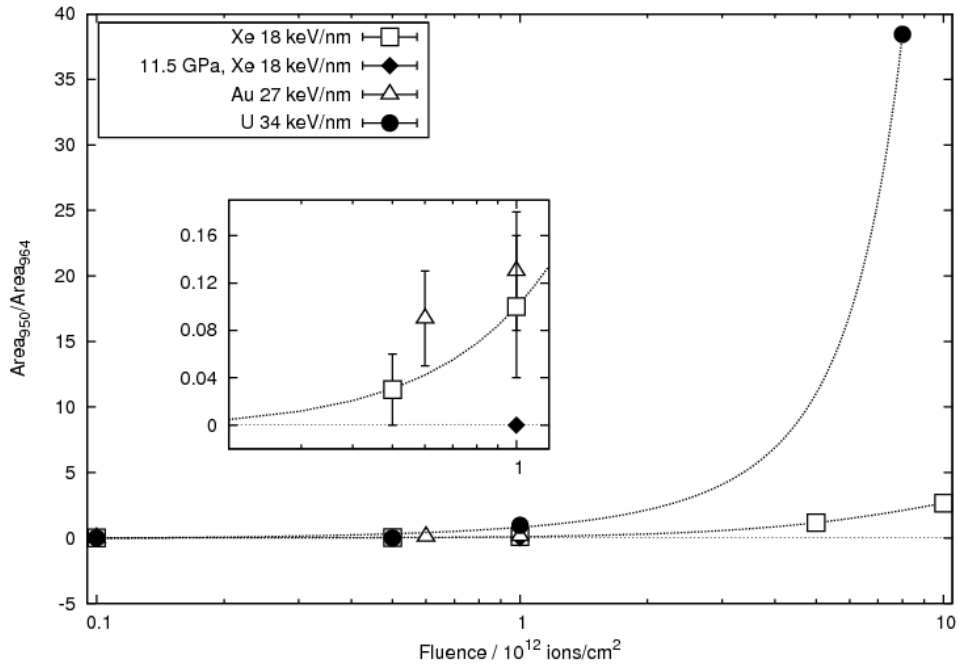

Figure 4.5: Amorphous fraction, depicted as area ratio of the radiation-induced broad band at ∼950 cm^{-1} to the 964 cm^{-1} band as a function of fluence and energy loss. Data of irradiation with U is taken with kind permission from Liu et al. (2008). The lines are visual guides (Weikusat et al., 2010, *cf.* App. D)

Raman spectra still show the bands of crystalline apatite. This can be explained by the competing process of heat-induced recrystallisation (*cf.* Tisserand et al., 2004; Miro et al., 2005).

The application of external pressure during the irradiation stabilizes the crystal lattice and the broad band at ∼950 cm^{-1} is not detectable, at least not up to a fluence of 1×10^{12} ions/cm^2 (Fig. 4.5, *inset*). Regarding the changes of widths and peak positions of the bands, two cases have to be considered, depending on the crystallographic orientation of the sample. After irradiation along the *c*-axis, the pre-pressurized samples seem less damaged than the samples irradiated at ambient conditions. The bands are less broadened and the shift of peak positions is smaller. This indicates a lower amount of defects, resulting in lower stress and distortion of the lattice. The samples irradiated along the *a*-axes show increased peak shifts and larger FWHM broadening compared to the reference samples. Apparently, these samples have accumulated more damage. The reason for this behaviour is still under discussion. A relation to the differences in track-healing velocities for the different orientations seems plausible.

4.3 Irradiations in the Paris-Edinburgh Press

The pressurized cell was successfully irradiated at the heavy-ion synchrotron of GSI. The induced radioactivity in the press was rather large and delayed the extraction of the samples by ∼7 months. This experience led to an optimized shielding and an adapted anvil design (*cf.* Chap. 3.2.2). Zircon was chosen as sample material for the first experiment, because of its well-known sensitivity for radiation damage. After recovering of the sample, the Raman spectra show clear signs of irradiation-induced damage (Fig 4.6). This proves the feasibility of our setup for heavy-ion irradiation experiments.
The results have been presented as an invited talk at the combined *AIRAPT-22 & HPCJ-50* in Tokyo, Japan (Weikusat et al., 2009a, *cf.* App. C). A regular publication, also featuring the second successful experiment, is in preparation.

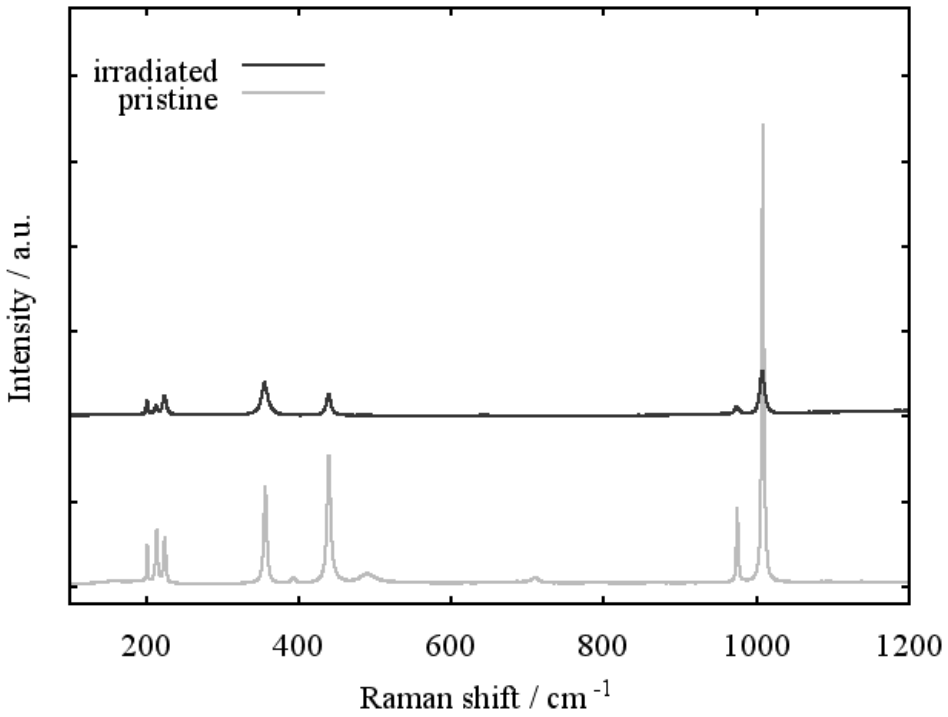

Figure 4.6: Raman spectra of zircon, pristine (*bottom*) and after irradiation with 1.5×10^{12} ^{124}Xe ions/cm^2 at a pressure of ∼6 GPa in the Paris-Edinburgh press (*top*). The spectra are stacked for clarity. (Weikusat et al., 2009a, *cf.* App. C)

5

Conclusions

The irradiation experiments conducted during the course of this thesis have shown significant differeneces in the response of the used crystals to changes caused by swift heavy ions.

The cordierite lattice is quite resistant against radiation-induced damage. While the number of point defects in the lattice increases with the ion fluence, no signs of large scale amorphisations could be found. Comparisons of irradiations along the different crystallographic axes did not yield systematic changes in terms of crystallinity or defect production. The most interesting are the changes imposed on the volatile phases in the structural channels along the c-axis. A general decrease of the amounts of channel constituents has also previously been reported for heating experiments, but the conversion of carbon dioxide to carbon monoxide can not be achieved by heating. It has to be considered as a unique effect of irradiation.

The irradiation experiments with apatites under various conditions, which were mainly motivated by its importance for fission-track dating, could show an increasing amount of amorphisation in the sample with higher ion fluences. In agreement with previous experiments, complete amorphisation could not be achieved. Irradiations along the different crystallographic axes show distinct differences between the orientations and generally larger amounts of damage in the crystals irradiated parallel to the principal axis (0001). The application of external pressure during irradiations stabilises the lattice and can prevent amorphisation. While the pressures used in this thesis exceed the pressures relevant for track formation under geologic conditions, these results still show the demand for a better understanding of the underlying processes.

First irradiations of the large-volume Paris-Edinburgh press were succesfully conducted and have shown the feasibilty of this setup. The possibilities of irradiating substantially larger samples volumes compared to DAC techniques will motivate many promising experiments in the future.

References

Aines, R. D. and Rossman, G. R. (1984). The high temperature behavior of water and carbon dioxide in cordierite and bervl. *American Mineralogist*, 69:319–327.

Armbruster, T. (1985). Ar, N_2 and CO_2 in the Structural Cavities of Cordierite, an Optical and X-ray Single-Crystal Study. *Physics and Chemistry of Minerals*, 12:233–245.

Armbruster, T. and Bloss, F. D. (1981). Mg-Cordierite: Si/Al Ordering, Optical Properties, and Distortion. *Contributions to Mineralogy and Petrology*, 77:332–336.

Armbruster, T. and Bloss, F. D. (1982). Orientation and effects of channel H_2O and CO_2 in cordierite. *American Mineralogist*, 67:284–291.

Besson, J. M., Klotz, S., Hamel, G., Makarenko, I., Nelmes, R. J., Loveday, J. S., Wilson, R., and Marshall, W. G. (1995). High pressure neutron diffraction. present and future possibilities using the paris-edinburgh cell. *High Pressure Research*, 14:1:1–6.

Boyer, L. L. and Fleury, P. A. (1974). Determination of interatomic interactions in $Ca_{10}(PO_4)_6F_2$ (fluorapatite) from structural and lattice dynamical data. *Physical Review B: Condensed Matter and Materials Physics*, 9:2693–2700.

Comodi, P., Liu, Y., and Frezzotti, M. L. (2001). Structural and vibrational behaviour of fluoroapatite with pressure. part ii: in situ micro-raman spectroscopic investigations. *Physics and Chemistry of Minerals*, 28:225–231.

Conlon, T. W. (1985). Nuclear physics for materials technology accelerator based methods. *Contemp Phys*, 26:621–558.

Faye, G. H., Manning, P. G., and Nickel, E. H. (1968). The polarized optical absorption spectra of tourmaline, cordierite, chloritoid and vivianite: ferric-ferrous electron interaction as a source of pleochroism. *American Mineralogist*, 53:1174–1201.

Geiger, C. A., Rager, H., and Czank, M. (2000). Cordierite III: the site occupation and concentration of Fe^{3+}. *Contributions to Mineralogy and Petrology*, 140:344–352.

Gelletly, W. (2001). Science with radioactive beams: the alchemist's dream. *Contemp Phys*, 42:285–314.

Gibbs, G. V. (1966). The polymorphism of cordierite I: The crystal structure of low cordierite. *American Mineralogist*, 51:1068–1087.

Goldmann, D. S. and Rossman, G. R. (1977). Channel constituents in cordierite. *American Mineralogist*, 62:1144–1157.

Güttler, B., Salje, E., and Putnis, A. (1989). Structural States of Mg Cordierite III: Infrared Spectroscopy and the Nature of the Hexagonal-Modulated Transition. *Physics and Chemistry of Minerals*, 16:365–373.

Hegedüs, R., Åkesson, S., Wehner, R., and Horváth, G. (2007). Could Vikings have navigated under foggy and cloudy conditions by skylight polarization? On the atmospheric optical prerequisites of polarimetric Viking navigation under foggy and cloudy skies. *Proc R Soc A*, 463:1081–1095.

Johannes, W. and Schreyer, W. (1981). Experimental introduction of CO_2 and H_2O into Mg-cordierite. *American Journal of Science*, 281:299–317.

Kaindl, R., Tropper, P., and Deibl, I. (2006). A semi-quantitative technique for determination of CO_2 in cordierite by Raman spectroscopy in thin sections. *European Journal of Mineralogy*, 18:331–335.

Kalmus, P. I. P. (1985). Experimental techniques in particle physics. *Contemp Phys*, 26:217–239.

Khomenko, V. M., Langer, K., and Geiger, C. A. (2001). Structural locations of the iron ions in cordierite: a spectroscopic study. *Contributions to Mineralogy and Petrology*, 141:381–396.

Kitamura, M. and Hiroi, Y. (1982). Indialite from Unazuki Pelitic Schist, Japan, and Its Transition Texture to Cordierite. *Contributions to Mineralogy and Petrology*, 80:110–116.

Klein, R. (2010). *Swift Heavy Ion Irradiated Boron Nitride With and Without the Application of High Pressure*. PhD thesis, Ruperto-Carola University of Heidelberg.

Klotz, S., Besson, J. M., Hamel, G., Nelmes, R. J., Loveday, J. S., and Marshall, W. G. (1996). High pressure neutron diffraction using the paris-edinburgh cell: Experimental possibilities and future prospects. *High Pressure Research*, 14:4:249–255.

Kolesov, B. A. and Geiger, C. A. (2000). Cordierite II: The role of CO_2 and H_2O. *American Mineralogist*, 85:1265–1274.

Kravitz, L. C., Kingsley, J. D., and Elkin, E. L. (1968). Raman and Infrared Studies of Coupled ${PO_4}^{3-}$ Vibrations. *Journal of Chemical Physics*, 49:4600–4610.

Lang, M., Glasmacher, U. A., Neumann, R., Trautmann, C., Schardt, D., and Wagner, G. A. (2005). Energy loss of 50-GeV uranium ions in natural diamond. *Appl Phys A*, 80:691.

Lewis, I. R. and Edwards, H. G. M., editors (2001). *Handbook of Raman Spectroscopy: From the research Laboratory to the Process line.* Marcel Dekker, Inc.

Liu, J., Glasmacher, U. A., Lang, M., Trautmann, C., Voss, K.-O., Neumann, R., Wagner, G. A., and Miletich, R. (2008). Raman spectroscopy of apatite irradiated with swift heavy ions with and without simultaneous exertion of high pressure. *Applied Physics A*, 91:17–22.

Łodziński, M., Wrzalik, R., and Sitarz, M. (2005). Micro-Raman spectroscopy studies of some accessory minerals from pegmatite of the Sowie Mts and Strzegom-Sobótka massif, LowerSilesia, Poland. *J Mol Struc*, pages 744–747.

Mao, H., Xu, J., and Bell, P. (1986). Calibration of the ruby gauge to 800 kbar under quasihydrostatic conditions. *Journal of Geophysical Research*, 91:4673–4676.

McMillan, P., Putnis, A., and Carpenter, M. A. (1984). A Raman Spectroscopic Study of Al-Si Ordering in Synthetic Magnesium Cordierite. *Physics and Chemistry of Minerals*, 10:256–260.

Miletich, R., Allan, D., and Kuhs, W. (2000). High-pressure single-crystal techniques. *Rev Mineral Geochem*, 41:445–519.

Miro, S., Grebille, D., Chateigner, D., Pelloquin, D., Stoquert, J.-P., Grob, J.-J., Costantini, J.-M., and Studer, F. (2005). X-ray diffraction study of damage induced by swift heavy ion irradiation in fluorapatite. *Nucl. Instrum. Methods Phys. Res., Sect. B*, 227:306–318.

Mirwald, P. W. (1982). A high-pressure phase transition in cordierite. *American Mineralogist*, 67:277–283.

Nasdala, L., Wildner, M., Wirth, R., Groschopf, N., Pal, D. C., and Möller, A. (2006). Alpha particle haloes in chlorite and cordierite. *Mineralogy and Petrology*, 86:1–27.

Parkin, K. M., Loeffler, B. M., and Burns, R. G. (1977). Mössbauer spectra of kyanite, aquamarine, and cordierite showing intervalence charge transfer. *Physics and Chemistry of Minerals*, 1:301–311.

Penel, G., Leroy, G., Rey, C., and Bres, E. (1998). MicroRaman Spectral Study of the PO_4 and CO_3 Vibrational Modes in Synthetic and Biological Apatites. *Calcif Tissue Int*, 63:475–481.

Poon, W. C.-K., Putnis, A., and Salje, E. (1990). Structural states of Mg cordierite: IV. Raman spectroscopy and local order parameter behaviour. *Journal of Physics: Condensed Matter*, 2:6361–6372.

Putnis, A. (1980). Order-modulated structures and the thermodynamics of cordierite reactions. *Nature*, 287:128–131.

Putnis, A., Salje, E., Redfern, S. A. T., Fyfe, C. A., and Strobl, H. (1987). Structural States of Mg-Cordierite I: Order Parameters from Synchrotron X-Ray and NMR Data. *Physics and Chemistry of Minerals*, 14:446–454.

Raman, C. V. and Krishnan, K. S. (1928). A new type of secondary radiation. *Nature*, 121:501.

Salje, E. (1987). Structural States of Mg-Cordierite II: Landau Theory. *Physics and Chemistry of Minerals*, 14:455–460.

Santosh, M., Jackson, D. H., and Harris, N. B. W. (1993). The Significance of Channel and Fluid-Inclusion CO_2 in Cordierite: Evidence from Carbon Isotopes. *Journal of Petrology*, 34:233–258.

Schouwink, P., Miletich, R., Ullrich, A., Glasmacher, U. A., Trautmann, C., Neumann, R., and Kohn, B. P. (2009). Ion tracks in apatite at high pressures. the effect of crystallographic track orientation on the elastic properties of fluorapatite under hydrostatic compression. *Physics and Chemistry of Minerals*, accepted.

Smekal, A. (1923). Zur Quantentheorie der Dispersion. *Naturwissenschaften*, 43:873.

Smith, E. and Dent, G. (2005). *Modern Raman Spectroscopy - A Practical Approach*. John Wiley & Sons, Ltd.

Tisserand, R., Rebetez, M., Grivet, M., Bouffard, S., Benyagoub, A., Levesque, F., and Carpena, J. (2004). Comparative amorphization quantification of two apatitic materials irradiated with heavy ions using XRD and RBS results. *Nucl. Instrum. Methods Phys. Res., Sect. B*, 215:129–136.

Tsuda, H. and Arends, J. (1994). Orientational micro-raman spectroscopy on hydroxyapatite single crystals and human enamel crystallites. *J Dent Res*, 73:1703–1710.

Ullrich, A., Miletich, R., Nestola, F., Weikusat, C., and Ohashi, H. (2009). Lattice compression and structural behavior of $NaVSi_2O_6$ clinopyroxene to 11 GPa. *American Mineralogist*, 94:557–564.

Vance, E. R. and Price, D. C. (1984). Heating and Radiation Effects on Optical and Mössbauer Spectra of Fe-bearing Cordierites. *Physics and Chemistry of Minerals*, 10:200–208.

Vry, J. K., Brown, P. E., and Valley, J. W. (1990). Cordierite volatile content and the role of CO_2 in high-grade metamorphism. *American Mineralogist*, 75:71–88.

Wagner, G. A. and van den Haute, P. (1992). *Fission track dating*. Ferdinand Enke Verlag, Stuttgart.

Weber, W. J., Ewing, R. C., Catlow, C. R. A., Diaz de la Rubia, T., Hobbs, L. W., Kinoshita, C., Matzke, H., Motta, A. T., Nastasi, M., Salje, E. H., Vance, E. R., and Zinkle, S. J. (1998). Radiation effects in crystalline ceramics for the immobilization of high-level nuclear waste and plutonium. *Journal of Materials Research*, 13:1434–1484.

Weikusat, C. (2005). Spektroskopische Charakterisierung von Diamant. Master's thesis, Johannes Gutenberg-Universität, Mainz, Germany. (*Diplomarbeit*).

Weikusat, C., Burchard, M., Klotz, S., Miletich, R., Glasmacher, U. A., Trautmann, C., and Neumann, R. (2009a). Experimental heavy-ion irradiation in the Paris-Edinburgh press: first results (*abstract*). In Tsuji, K., editor, *International Conference on High Pressure Science and Technology - Joint AIRAPT-22 & HPCJ-50, Odaiba, Tokyo, JAPAN*, volume 19 of *Review of High Pressure Science and Technology*.

Weikusat, C., Glasmacher, U. A., Miletich, R., Neumann, R., and Trautmann, C. (2008). Raman spectroscopy of heavy ion induced damage in cordierite. *Nucl. Instrum. Methods Phys. Res., Sect. B*, 266:2990–2993.

Weikusat, C., Glasmacher, U. A., Miletich, R., Schuster, B., Trautmann, C., and Neumann, R. (2010). Raman study of apatite amorphised with swift heavy ions under various irradiation conditions. *Phys Chem Mineral*, submitted.

Weikusat, C., Miletich, R., Glasmacher, U. A., Trautmann, C., and Neumann, R. (2009b). Heavy-ion irradiation on crystallographically oriented cordierite and the conversion of molecular CO_2 to CO: a Raman spectroscopic study. *Physics and Chemistry of Minerals*, doi:10.1007/s00269-009-0343-x.

Williams, Q. and Knittle, E. (1996). Infrared and Raman spectra of $Ca_5(PO_4)_3F$-Fluorapatite at high pressures: compression-induced changes in phosphate site and Davydov splitting. *J Phys Chem Solids*, 57:417–422.

Ziegler, J. F., Biersack, J. P., and Ziegler, M. D. (2008). *The Stopping and Range of Ions in Matter*. Lulu Press Co.

Appendix A

Publication I - Raman spectroscopy of heavy ion induced damage in cordierite

C. Weikusat, U.A. Glasmacher, R. Miletich, R. Neumann, C. Trautmann (2008)
Nuclear Instruments and Methods in Physics Research Section B, Vol. 266, Issues 12-13, pp. 2990-2993.

Abstract

Natural cordierite crystals were irradiated with Xe ions of 1.465 GeV kinetic energy and fluences ranging from 10^8 to 10^{12} ions/cm^2. Raman spectra of the surface and line scans along the trajectory of the ions have been recorded. At a fluence of 10^{12} ions/cm^2 the colour of the originally blue sample changed to yellow and the Raman spectrum shows distinct band broadening. Irradiation also alters the content and nature of volatiles (CO_2, H_2O) incorporated into structural channels. Similar eects have been described for cordierite affected by natural irradiation from a decay processes.

1. Introduction

The mineral cordierite (general formula: (Mg, Fe^{2+})$_2$ $Al_4Si_5O_{18}$) is a common framework silicate. The main structural features are corner-sharing six-membered rings of SiO_4-tetrahedra which form channels along the crystallographic c-axis. During crystal growth, alkali atoms and various volatiles (*e.g.* CO_2, H_2O) are easily incorporated into these channels. The channel constituents are used in petrology to determine the chemical composition of the growth environment.

The physical properties of cordierite are useful for various applications. Its pleochroism (different colours along each of the crystallographic axes) is interesting for the gemstone industry (sale name Iolith). The blue colour is assigned to intervalence charge transfer between Fe^{2+} and Fe^{3+} along the crystallographic c-axis. The low thermal expansion and excellent resistance to thermal shock are mainly utilised in the manufacturing of technical ceramics, where cordierite is used as substrate material for catalytic converters and for various applications in aerospace industry.

In natural cordierite radiation damage has been observed as yellow to brownish rings formed around U- or Th-bearing mineral inclusions (*e.g.* monazite) [1]. These zones are ascribed to defects induced by α-decay events and the recoil of heavy daughter nuclei subsequent to the emission of an α particle. Close to the inclusion, also structural changes and nearly complete amorphisation have been identified by transmission electron microscopy measurements [1]. Amorphisation of cordierite has also been reported for irradiation with Xe ions of low energy (1.5 MeV) [2].

This study was guided by the question how cordierite reacts to swift heavy ions and whether these changes are detectable by means of Raman spectroscopy.

2. Experimental

As material we used natural cordierite single crystals from Mt. Tsilaizina (Madagascar). Small pieces of thickness $\sim$1.7 mm were exposed to Xe ions of 1.465 GeV kinetic energy at the UNILAC linear accelerator of GSI. The irradiation experi-

ments were performed at room temperature, applying fluences between 10^8 and 10^{12} ions/cm^2. The flux was limited to 2×10^8 ions/cm^{2}s to avoid beam-induced sample heating. The penetration depth and energy loss of the ions were calculated with the SRIM2006 code [3], assuming the standard chemical composition ($(Mg,Fe^{2+})_2Al_4Si_5O_{18}$) and a density of 2.65 g/cm^3. The calculated penetration depth was about 90 μm and thus considerably smaller than the sample thickness. The energy loss is almost exclusively based on electronic stopping amounting to 15 keV/nm at the sample surface [3].

Raman spectra of the irradiated crystals were recorded in the range between 100 and 4000 cm^{-1} with a LabRam HR800 UV spectrometer equipped with an OLYMPUS BXFM-ILHS optical microscope, automated xy stage, a grating with 1800 grooves per millimeter and Peltier-cooled CCD detector. The microscope has an objective with 100× magnification and a numerical aperture of 0.9. The spectra were excited using the 632.8 nm line of a He-Ne laser. The lateral resolution was ~2 μm, the wavenumber accuracy was 0.5 cm^{-1} and the spectral resolution was 1 cm^{-1}.

Spectra were recorded normal to the crystal surface. The sample was tilted afterwards by 90° and the automatic x-y stage was used to collect point measurements with a stepwidth of 1 μm on the side of the crystal perpendicular to the irradiated surface. With this method it is possible to accurately trace the beam-induced changes along the length of the ion trajectory without the need for the tedious and inherently imprecise optical depth calibration. Since the intensity ratios of the various Raman bands are known to depend on the crystal orientation, great care was taken to avoid tilting when translating the lateral sample position.

3. Results

While there are only minimal alterations up to a fluence of 10^{11} ions/cm^2, the sample irradiated with 10^{12} ions/cm^2 shows significant differences. Therefore only data of the sample irradiated with the highest fluence will be discussed. Macroscopic investigation of the irradiated sample revealed cracks along the interface between the irradiated and non-irradiated part. After irradiation, the colour of the irradiated layer has changed to yellowish-brown. To clarify whether this colour change is due to ionization-induced change of the Fe^{3+} trace amount or the formation of electron colour centers (F-centers) [4], optical absorption measurements on prethinned crystals are in preparation.

Fig. 1 shows the Raman spectrum in the area of the main lattice vibrations (100-1600 cm^{-1}) before and after irradiation. The most obvious change is the decrease in the signal-to-noise ratio, which is ascribed to radiation-induced defects resulting in a decrease of band intensities and simultaneous increase of defect-induced background luminescence. While the positions of the bands remain constant, most bands show a slight but distinct broadening of the full width at half maximum (Table 1). This demonstrates deteriorating short-range order of the

crystal structure [5] and could also be an indicator for amorphisation, which has been reported for cordierite irradiated with Xe ions of lower energy (1.5 MeV) [2]. However, as the energy loss of low energetic particles is dominated by elastic collision processes (nuclear instead of electronic stopping), the possibility of amorphisation has to be checked with further measurements (*e.g.* TEM). Other minor changes in the spectra might result from slight differences in the crystallographic orientation of the samples and were thus not analysed quantitatively.

The Raman band at 1382 cm^{-1} is due to the symmetric O-C-O stretching of structurally bound CO_2 [6]. After irradiation, the intensity of this band is reduced and a new band at 2135 cm^{-1}, which can be assigned to carbon monoxide [1,7,8], appears. It is reasonable to assume, that the carbon monoxide resides in similar cavities of the structural channels as the carbon dioxide [9], however, the exact structural relations are yet unknown and remain subject to further investigations.

Analysis of the intensity of these two bands recorded along a line perpendicular to the irradiated surface shows a clear correlation with the penetration depth of the ions (Figs. 2 and 3). This observation suggests that there has been a radiation-induced conversion of CO_2 to CO.

The O-H stretching band of molecular H_2O at 3598 cm^{-1} [6] shows a similar evolution with depth (Figs. 2 and 3). The loss of OH species as a result of natural irradiation damage has also been described for other silicate minerals [10].

In both cases, the spectra taken at 100 μm depth (i.e. beyond the calculated range of the ions) are identical to those of the non-irradiated sample.

4. Conclusions

Natural cordierites have been subjected to swift heavy ion irradiation. Raman spectroscopy of samples irradiated with a rather high fluence of 10^{12} ions/cm^2 indicates a change of the short-range order of the crystal structure. Based on experience with many other minerals [12], it is reasonable to assume that the ion tracks in cordierite consist of locally amorphised regions.

Volatile molecules incorporated in structural channels also experience significant changes. The contents of H_2O and CO_2 are decreased after irradiation and the appearance of a new band suggests the conversion of CO_2 to CO.

Experiments with crystallographically oriented samples are in preparation to further complement our results.

Acknowledgement

Data were fitted using the free software FITYK 0.8.1
(http://www.unipress.waw.pl/fityk/).

References

[1] L. Nasdala, M. Wildner, R. Wirth, N. Groschopf, D.C. Pal, A. Möller, Alpha particle haloes in chlorite and cordierite, Miner. Petrol. 86 (2006) 1.

[2] S.X. Wang, L.M. Wang, R.C. Ewing, R.H. Doremus, Ion beam- induced amorphization of MgO-Al_2O_3-SiO_2. I: Experimental and theoretical basis, J. Non-Cryst. Solids 238 (1998) 198.

[3] J.F. Ziegler, J.P. Biersack, U. Littmark, The Stopping and Range of Ions in Solids, Pergamon, New York, 1985.

[4] E.R. Vance, D.C. Price, Heating and Radiation Effects on Optical and Mössbauer Spectra of Fe-bearing Cordierites, Phys. Chem. Miner. 10 (1984) 200.

[5] W.C.-K. Poon, A. Putnis, E. Salje, Structural states of Mg cordierite IV: Raman spectroscopy and local order parameter behaviour, J. Phys.: Condens. Matter 2 (1990) 6361.

[6] B.A. Kolesov, C.A. Geiger, Cordierite II: The role of CO_2 and H_2O, Am. Mineral. 85 (2000) 1265.

[7] J.D. Pasteris, B.J. Wanamaker, Laser Raman microprobe analysis of experimentally re-equilibrated fluid inclusions in olivine: Some implications for mantle fluids, Am. Mineral. 73 (1988) 1074.

[8] M. Lipp, W.J. Evans, V. Garcia-Baonza, H.E. Lorenzana, Carbon monoxide: spectroscopic characterisation of the high-pressure polymerized phase, J. Low Temp. Phys. 111 (1998) 247.

[9] R.D. Aines, G.R. Rossmann, The high temperature behavior of water and carbon dioxide in cordierite and beryl, Am. Mineral. 69 (1984) 319.

[10] L. Nasdala, Raman mapping - a tool for revealing internal structures of minerals, Acta Univ. Carolinae Geol. 46 (2002) 61.

[11] M. Łodziński, R. Wrzalik, M. Sitarz, Micro-Raman spectroscopy studies of some accessory minerals from pegmatite of the Sowie Mts and Strzegom-Sobótka massif, LowerSilesia, Poland, J. Mol. Struct. 744-747 (2005) 1017.

[12] M. Toulemonde, W. Assmann, C. Dufour, A. Meftah, F. Studer, C. Trautmann, in: P. Sigmund (Ed.), Ion Beam Science: Solved and Unsolved Problems, Invited Lectures Presented at a Symposium in Copenhagen, 1-5 May 2006, The

Royal Danish Academy of Science and Letters, 2006, Part I (p. 376), Part II (p. 384).

Band position (cm^{-1})	before irradiation	after irradiation	band assignment
	FWHM (cm^{-1})	FWHM (cm^{-1})	
128	4.9 (0.1)	6.3 (0.2)	-
260	5.4 (0.3)	7.9 (0.3)	-
555	9.9 (0.2)	10.5 (0.4)	-
578	11.5 (0.3)	13.7 (0.3)	-
671	9.6 (0.2)	10.6 (0.2)	-
973	7.3 (0.1)	8.3 (0.1)	-
1011	8.3 (0.2)	9.0 (0.1)	ν_3 anti-symmetric stretching Si-O [11]
1382	3.2 (0.2)	7.4 (0.5)	symmetric stretching CO_2 [6]
2135	not detectable	1.5 (0.6)	stretching CO [1,7,8]
3589	3.5 (0.1)	not detectable	stretching H_2O [6]

Table 1 FWHM of selected bands of the cordierite Raman spectrum before and after irradiation with 10^{12} Xe ions/cm^2 and band assignments taken from literature. To the best of our knowledge, there are no further reliable band assignments available in literature.

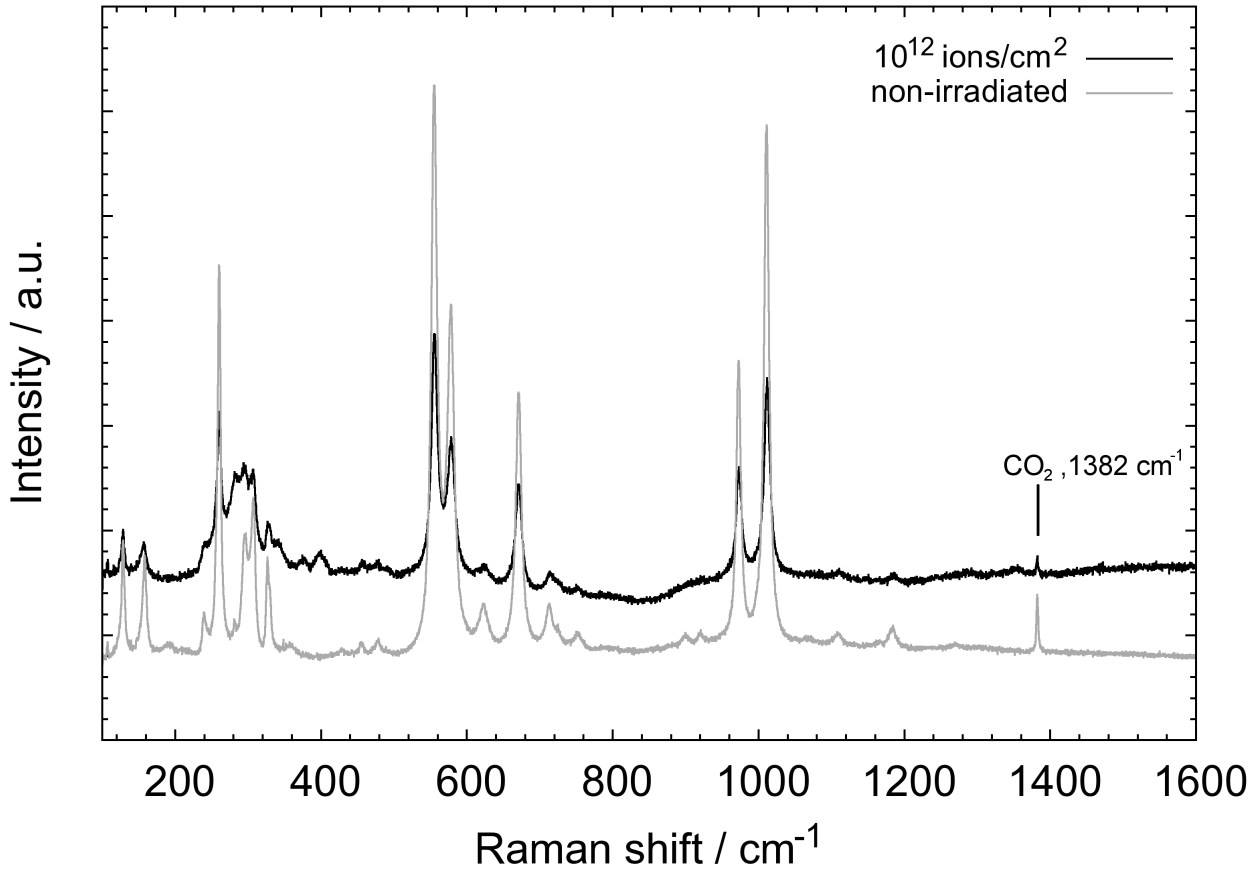

Fig. 1 Raman spectra of the main crystal lattice vibrations of cordierite, pristine and after irradiation with 10^{12} Xe ions/cm^2. The spectra are presented as recorded, without any stacking or background correction.

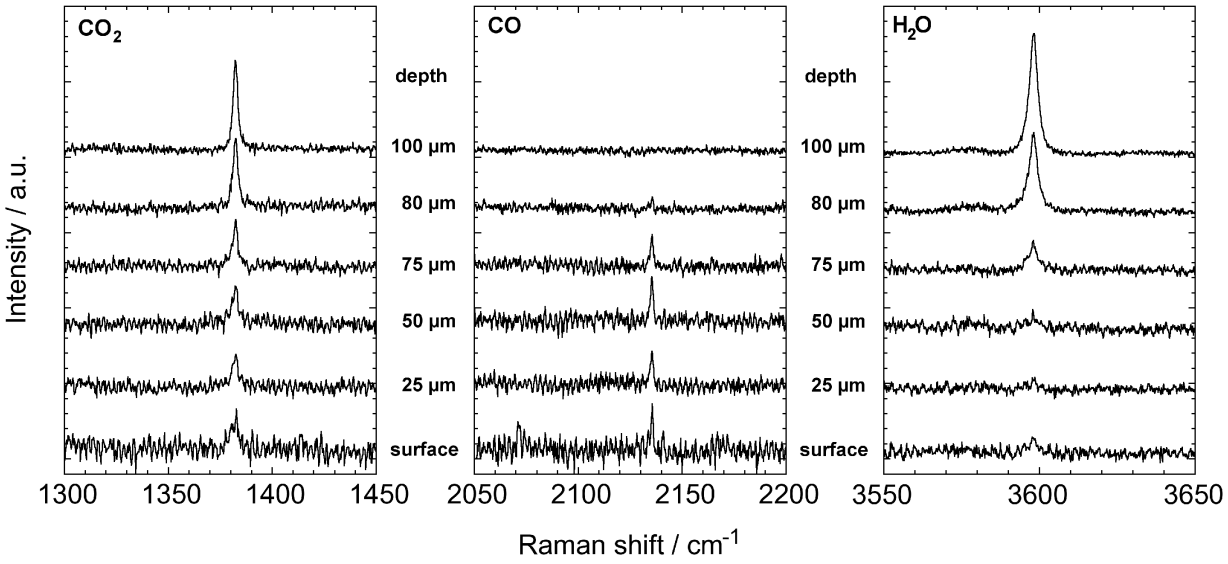

Fig. 2 Raman spectra recorded perpendicular to the irradiated crystal surface, illustrating the evolution of the CO_2 (1382 cm^{-1}), CO (2135 cm^{-1}) and H_2O (3589 cm^{-1}) bands as a function of penetration depth of the ion beam. The spectra are background corrected and stacked for clarification.

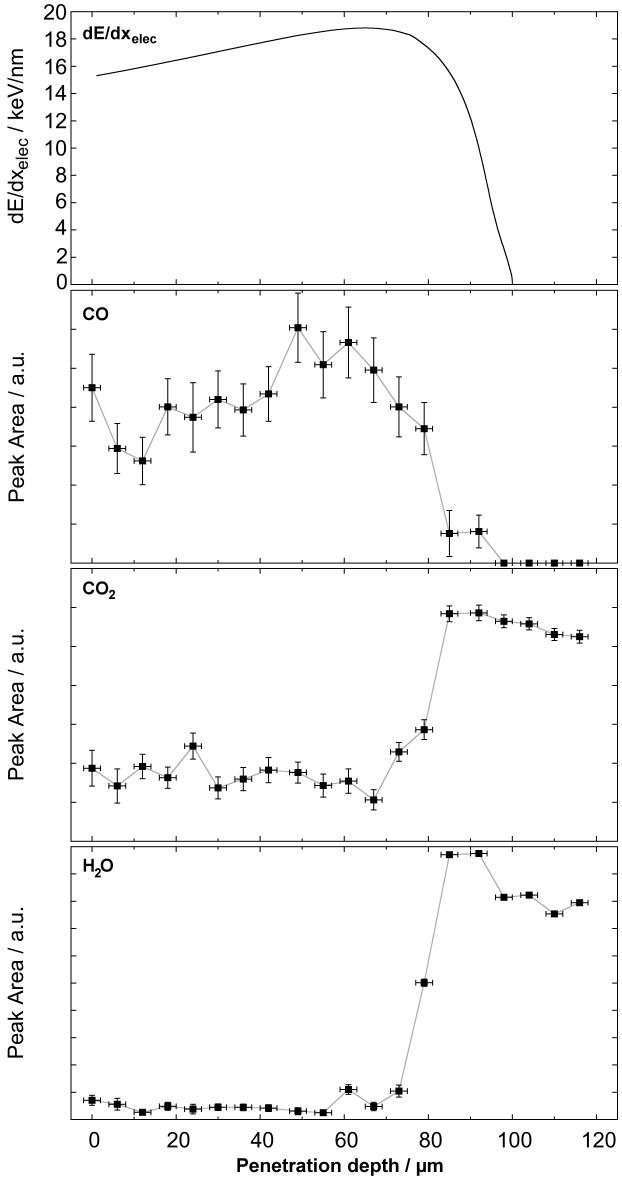

Fig. 3 The evolution of the electronic energy loss (as calculated with SRIM2006) and the band area (background corrected) at 1382 cm^{-1} (CO_2), 2135 cm^{-1} (CO) and 3589 cm^{-1} (H_2O) as a function of penetration depth of the ion beam.

Appendix B

Publication II - Heavy-ion irradiation on crystallographically oriented cordierite and the conversion of molecular CO_2 to CO: a Raman spectroscopic study

C. Weikusat, R. Miletich, U.A. Glasmacher, R. Neumann, C. Trautmann (2009)
Physics and Chemistry of Minerals, doi:10.1007/s00269-009-0343-x.

Abstract

Crystallographically oriented sections of natural gemstone quality cordierite single-crystals have been irradiated with swift heavy ions of GeV energy and various fluences. Irradiation effects on the crystal lattice were investigated by means of Raman spectroscopy. Raman line scans along the trajectory of the ions reveal a close correlation of beam parameters (such as fluence and energy loss dE/dx along the ion path) to strain due to associated changes in lattice dimensions and defect concentration. The luminescence background also scales with the ion fluence and suggests the formation of point defects, which could also account for the macroscopically observable colouration of the irradiated samples. In addition, changes in the amount and nature of volatile species inside the structural channels are observed. They also scale with dE/dx and confirm the previously postulated irradiation-induced conversion of CO_2 to CO. Irradiations along the crystallographic a-, b- and c-axis reveal no significant anisotropy effect with respect to lattice alterations. The polarisation characteristics of the Raman-active modes confirm the preferred molecular alignment of CO and CO_2 along the a-axis direction.

Introduction

The silicate mineral cordierite, $(Mg,Fe)_2Al_4Si_5O_{18} \cdot n\ (H_2O,CO_2,...)$, is a common tectosilicate with six-membered $(Al,Si)_6O_{18}$ silicate rings forming continuous channels parallel to the crystallographic c-axis. Various fluid and volatile phases (*e.g.* H_2O, CO_2, CO, N_2, Ar, hydrocarbons, etc.) can be incorporated into these channels, either during growth or under the influence of external fluid pressure. The nature and concentration of the channel constituents are used in petrology to obtain information about fluid evolution during metamorphism and anatexis (*e.g.* Mirwald 1982; Vry et al. 1990; Santosh et al. 1993). Cordierite is also subject of a prominent phase transition to the hexagonal high-temperature phase indialite, which exhibits a random and disordered Si, Al distribution on the tetrahedral sites within the alumosilicate framework. The mechanisms and details of this cation ordering have been subject to a larger number of studies (*e.g.* Gibbs 1966; Armbruster and Bloss 1981; Putnis 1980; Güttler et al. 1989; Poon et al. 1990). Apart from having received considerable attention due to the low dielectric constants and thermal expansion coefficients of cordierite materials (*e.g.* Shannon et al. 1992), a further striking feature are the unusual optical properties, in particular the macroscopic colour and the distinct pleochroism. As they have been assigned to Fe^{2+}/Fe^{3+} charge transfer, the location and charge of iron in the lattice have been subject to various experimental and analytical investigations (*e.g.* Faye et al. 1968; Vance and Price 1984; Geiger et al. 2000; Khomenko et al. 2001). Content and nature of the volatile phases incorporated into the structural channels have been investigated by means of various techniques (*e.g.* Goldmann and Rossman

1977; Armbruster and Bloss 1982; Aines and Rossman 1984; Armbruster 1985; Kolesov and Geiger 2000; Kaindl et al. 2006).

Most recently, radiation-induced alterations of the cordierite host lattice have been investigated on radiohaloes, which originate from natural α-particle irradiation around actinide-bearing mineral inclusions (*e.g.* Monazite) in natural cordierite (Nasdala et al. 2006). Moreover, the effect of both artificial irradiation by α-particles (Krickl et al. 2008) and γ-ray irradiation (Vance and Price 1984) has been investigated in order to study effects which arise from radiation-induced defects. Weikusat et al. (2008) reported on various changes induced by irradiation with relativistic heavy ions, in particular on changes of the amount of channel constituents. One particular aspect of the analytical findings was the unambiguous spectroscopic evidence of ion irradiation-induced transformation of molecular carbon dioxide to carbon monoxide. Due to the fact that molecular CO_2 in the channel cavities is known to reveal a preferred orientation with the O-C-O vector being aligned along the [100] direction (*e.g.* Armbruster 1985; Malcherek et al. 2001), the investigation of oriented samples appeared to be an inevitable necessity in order to evaluate CO_2-CO transformation. Together with systematic variations of experimental conditions of irradiation, i.e. varied fluences applied to the sample, we present in this spectroscopic study the results of swift heavy-ion irradiation on oriented cordierite single-crystal samples.

Experimental

The samples were prepared from two specimens of natural gem quality cordierite single-crystals from Madagascar: one referred to as "CORTS" in this study, and one, purchased as a cut gemstone from a mineral trader, referred to as "CORMB1". Polished crystal sections were prepared after being oriented by optical microscopy using crossed polarisers and X-ray diffraction film methods. Oriented specimens embedded in epoxy resin were cut perpendicular to the crystallographic axes (a = 17.1 Å, b = 9.7 Å and c = 9.3 Å), and yield crystal platelets (size ∼5 mm × 5 mm × 100 μm) oriented parallel to (100), (010) and (001) plane directions, respectively, within a precision of about 0.3°. The average chemical composition obtained from electron microprobe analysis of both samples is shown in Table 1. The microprobe analyses of the major elements were carried out using a CAMECA SX-51 electron microprobe, operated at 15 kV accelerating voltage, 20 nA beam current, 20 s counting time for all elements, using natural and synthetic standards for calibration (albite, Na; periclase, Mg; anorthite, Al; wollastonite, Ca, Si; orthoclase, K; rhodonite, Mn; haematite, Fe). The CO_2 content before and after irradiation was estimated from Raman spectra using the relative intensities of Si-O and C-O stretching modes, applying the method described by Kaindl et al. (2006).

The samples were exposed to relativistic heavy ions (^{208}Pb, ^{197}Au) with kinetic energies up to 2.2 GeV (11.1 MeV per nucleon) at the UNILAC linear accelerator of GSI, applying fluences between 5×10^{11} and 2×10^{12} ions/cm^2. As cordierite

is known to develop cracks under heavy-ion irradiation (Weikusat et al. 2008), the samples were wrapped in a 10-μm thick aluminium foil, which is stable enough to prevent loss of sample fragments in case of chipping while being not too detrimental on the ion energy. To retain a pristine part for comparison, approximately half of the surface of the crystals was shielded from the ions by covering with a steel plate (thickness $\sim$2 mm). The irradiations were performed at room temperature and under normal beam incidence. Details of the individual irradiation parameters are compiled in Table 2.

Raman spectra in the range between 100 and 4,000 cm^{-1} were recorded under backscattering geometry with a LabRam HR800 UV spectrometer equipped with an OLYMPUS BXFM-ILHS optical microscope, automated x-y stage, a grating with 1,800 grooves/mm and an air-cooled CCD detector. The spectra were excited using the 632.8 nm line of a He-Ne laser. The width of the entrance slit was 100 μm. The lateral resolution of the system is $\sim$1 μm; wavenumber accuracy was estimated to be 0.5 cm^{-1} and spectral resolution 1 cm^{-1}. Spectra were acquired for each orientation with the electric field vector of the incident laser parallel to the respective crystallographic axes. To account for the structural and chemical fluctuations to be expected in natural samples, spectra of several different spots were acquired for each orientation. After manual polynomial background subtraction, Voigt functions were fitted to each peak. To trace the changes to the lattice and the volatile content along the entire path of the ions, line scans perpendicular to the irradiated surface (*i.e.* parallel to the trajectory of the incident ions) were acquired with a step width of 1 μm. Great care was taken to choose a crack-free part of the samples for the line scans. For comparison, we also recorded line scans of non-irradiated parts of the samples.

Results

Observation of macroscopic material changes

One of the most noticeable effects of irradiation is the colour change of irradiated parts of macroscopic cordierite crystals as already reported by Weikusat et al. (2008). The colour of the irradiated crystal volumes turns from pale violet-blue to yellowish-brown, an effect which is noticeable for all ions, fluences and irradiation directions. Apart from radiocolouration, cracks develop within the sample perpendicular to the incident beam and expand beyond the interface between irradiated and non-irradiated layers. Cracking occurred in all samples, independent on the crystal orientation and becoming more severe with increasing fluence. The cracks are irregular in shape and expand below the calculated penetration depth of the ions. In sample CORTS irradiated with the highest fluence (2×10^{12} ions/cm^2), the irradiated layer has separated completely from the non-irradiated part, so that it was impossible to perform a line scan across the interface. X-ray diffraction of these samples indicates a small but distinct quasi-isotropic decrease of the lat-

tice dimensions (Miletich, pers. comm.). The resulting volume mismatch and the emerging strain at the interface appear to yield a sufficient explanation for the mechanical chipping of the irradiated crystal fractions.

Raman spectroscopy

Lattice vibrations

Typical Raman spectra of the irradiated samples are shown in Fig. 1, comparing the spectra for equivalent sample orientation but different fluences (0, 5×10^{11}, 1×10^{12}, 2×10^{12} ions/cm^2). With increasing fluence, the intensity of all Raman bands decreases and the bands broaden due to the increasing amount of radiation-induced defects. The ion irradiation also leads to a pronounced increase of background luminescence. This effect was detectable for all measurements, although the exact shape of the luminescence spectra varies for the different orientations and even for different measurement spots on the same sample.

For Raman bands related to lattice vibrations of the silicate framework (100-1,200 cm^{-1}), the line scans along the ion trajectory show similar trends for all orientations and fluences. At the irradiated surface and along the major part of the irradiated layer, the intensities of all bands are decreased, until they gradually revert to the values of the non-irradiated sample towards the end of the ion trajectory. Simultaneously, the full widths at half maximum (FWHM) of the Raman modes increase with the amount of noticeable irradiation-induced changes. The values of FWHM gradually decrease with depth until they reach the values characteristic for non-irradiated cordierite. The depth evolution of the intensity and FWHM data are directly correlated with the energy loss dE/dx of the ions, as shown in Fig. 2. The extent of intensity loss and peak broadening seems to be independent on the orientation of the incident beam relative to the cordierite lattice.

The peak positions of the Raman bands are also changed after ion irradiation, but not consistently for all bands. The peak positions of most bands are shifted towards higher values in the irradiated part of the crystals, thus indicating compressive strain (Fig. 3a). However, some of the low-energy bands (*e.g.* ~128, ~157 and ~366 cm^{-1}) follow the opposite trend (Fig. 3b). While those two cases are also clearly correlated with dE/dx, few other bands (e.g. ~972 cm^{-1}) show rather arbitrary fluctuations.

Channel Volatiles

The intensities of the Raman bands representing ν_1 symmetric stretching vibrations of class I single H_2O molecules (3,589 cm^{-1}) and the ν_1 symmetric stretching vibration of single CO_2 molecules (1,382 cm^{-1}) decrease with increasing fluence, indicating a gradual loss of the respective species (Fig. 4). The CO_2 content of the CORMB1 sample before irradiation is 0.41 wt%, decreasing to 0.33 wt% after

irradiation with 8 MeV/u Pb ions (2×10^{12} ions/cm^2); for the CORTS sample, it amounts to 0.55 wt% (pristine) and 0.47 wt% (11.1 MeV/u Au ions, 2×10^{12} ions/cm^2). It is important to keep in mind that the intensities of the cordierite lattice modes are changed after irradiation, so that the intensity ratios used for this semi-quantitative technique might produce wrong values for the irradiated samples. In the high-frequency region of the Raman spectra, a new band at 2,135 cm^{-1} appears after irradiation, which is not detectable in any of the non-irradiated samples. This band has previously been detected in radiation-exposed cordierite and assigned to CO molecules formed by a radiation-induced conversion of CO_2 (Nasdala et al. 2006; Weikusat et al. 2008). Similar to the previous observations, the intensity increases with increasing fluence in all sample orientations (Fig. 4). The Raman line scans reveal a clear correlation between the volatile contents and the electronic energy loss dE/dx (Fig. 5). As the molecules of CO_2 and CO are preferentially aligned along the [100]-axis direction, Raman measurements with the electric field vector of the incident laser parallel to (100) yield the best signal to noise ratios. Irradiations in different orientations show no systematic differences for the 2,135 cm^{-1} band related to the CO stretching mode. A comparative line scan within the pristine sample showed, as expected, no systematic variations with depth, thus indicating the homogeneous concentration within the pristine sample.

Luminescence

The luminescence background clearly follows the evolution of the electronic energy loss dE/dx as a function of depth (Fig. 6). Yet as the shape and the intensity of the background are also influenced by various other factors (*e.g.* impurities, inclusions, pre-irradiation defects), this is difficult to quantify. To avoid influences from the omnipresent natural luminescence in the red spectral region, we chose the energy range 800-850 nm for our measurements, which was found to be completely flat in every pristine sample measured. The amount of background contribution varies slightly between different orientations, but we found no evidence for systematic changes with the irradiation direction.

Discussion

The general loss of intensity and the broadening of the bands in the spectra of irradiated samples indicate a decreasing short-range order in the lattice. However, both effects are rather small, compared to experimental ion irradiation of amorphisable minerals such as apatite or zircon (Zhang et al. 2000; Liu et al. 2008). Even for the highest fluence (2×10^{12} ions/cm^2), the main bands are still readily distinguishable above the background and there is no conclusive evidence for amorphisation, although electron beam induced phase decomposition and amorphisation of cordierite has been reported previously (Lee et al. 1986). The relative band intensities, which are significant to differentiate between the a-

and b-axis directions, do not indicate any change in the Al,Si ordering as known for the low-cordierite structure. Furthermore, the splitting of the bands in the 500-600 cm^{-1} region does not decrease, as would be expected for the Cccm-P6/mcc order-disorder transition (McMillan et al. 1984; Poon et al. 1990).

The shift of most Raman bands within the irradiated part of the crystals towards higher wavenumbers follows the trend for smaller lattice parameters, which would also be indicative for compressive strain on the lattice. Some bands, however, do not follow this trend. Several low-energy bands (possibly connected with rotations or translations, Łodziński et al. 2005) show decreasing Raman shifts. While the changes of those two groups are correlated with dE/dx, few other bands (*e.g.* ∼972 cm^{-1}, probably SiO_4 stretching, Łodziński et al. 2005) show only arbitrary fluctuations. The internal distribution of strain and pressure, and thus shift of the bands, is also influenced by several other mechanisms (*e.g.* clustered point defects, cracks and micro-cracks). A detailed investigation and discussion of their separate contributions is beyond the scope of this study. The origin of stress at the interface between the irradiated and non-irradiated layer is likely due to the volume and lattice-spacing mismatch and is most probably responsible for the extensive cracking that we observe. This could also have led to the development of micro-cracks throughout the sample. Hence, the resulting local release of internal strain might account for the erratic behaviour of the peak positions of some of the observed bands.

The reduction of volatile contents after irradiation has been described for a wide range of materials. In cordierite, it is known that all volatiles can be driven out of the channels by heating the samples to 900°C (Aines and Rossman 1984). Although the ion beam intensity was limited to avoid macroscopic heating of the sample during irradiation, the mobility of the H_2O molecules may be enhanced by a thermal spike process occurring when ions tracks are formed (Toulemonde et al. 2001). Accordingly, water molecules could, therefore, be driven out of the channels in a similar fashion as described for conventional heating experiments. However, this mechanism should yield significant anisotropies for irradiation along different crystallographic directions, which could not be observed in the spectra of available samples. On the other hand, the low molar enthalpy of 42 kJ/mol for cordierite dehydration (Carey and Navrotsky 1992), the high dynamics of H_2O molecules and their rotational disorder at the Ch1/4 position (Carson et al. 1982; Armbruster 1985; Winkler and Hennion 1994; Winkler et al. 1994a, b) and the significant weight loss below 200°C (Zimmermann 1981) together with the experimentally determined reversibility of hydration (Armbruster and Bloss 1982) suggest a high mobility of extra-framework channel constituents similar to those in microporous silicate framework structures. It is also reasonable to assume that some atoms, in particular oxygen atoms, diffuse from the track region into the surrounding crystal lattice and form oxygen interstitials. This may explain the increase of luminescence background as a function of ion fluence. The luminescence background may also originate from the formation and recombination of Frenkel and anti-Frenkel

defects, involving interstitial sites and structural vacancies. The latter have been supposed to account for the origin of the colour change of radiation-damaged cordierites, due to electronic charge transfer transitions between the Fe centres and electrons trapped at oxygen vacancies (Nasdala et al. 2006). Colour changes induced by γ-irradiation have been reported to be reversible on moderate heat treatment ($\sim$300°C), due to thermally induced electronic redistribution (Vance and Price 1984). The generation of F-centres as well as the observed behaviour of the luminescence background appears to be associated with the point defects concentration emerging from exposure to ionising radiation.

Due to the size of the CO_2 molecule, carbon dioxide was reported to be trapped inside the $\sim$6 Å structural cavities of the channels, preferentially aligned with its O-C-O vector parallel to the crystallographic a-axis (Armbruster and Bürgi 1982; Armbruster and Bloss 1982; Aines and Rossman 1984), and only minor fractions oriented parallel to the c-axis (Armbruster 1985). Given the high mobility of H_2O molecules (in particular, class I H_2O) within the channels, H_2O can be removed at relatively low temperatures (Zimmermann 1981; Vry et al. 1990; Carey and Navrotsky 1992; Kolesov and Geiger 2000), whereas heating to 900°C is required to expel all CO_2 molecules from the channels (Aines and Rossman 1984). Nevertheless, the decrease of its most prominent band in the Raman spectrum, *i.e.* the symmetric stretching mode at 1,382 cm^{-1}, significantly correlates with the applied ion fluence. The corresponding decrease of molecular CO_2 is evidently inversely proportional to the increase in the CO content, as given evidence by the intensity of the CO stretching mode at 2,135 cm^{-1}. The polarisation characteristics yield the largest intensities for E//a, thus agreeing with the findings of Khomenko and Langer (2005), who proposed the alignment of CO along the crystallographic a-axis. This orientation is energetically more favourable because the cavity diameter is longer in the a-axis direction ($\sim$6.0 Å) compared to the b-axis direction ($\sim$5.4 Å), thus giving a better stereochemical matching of the linear shape of both molecular species.

Radiation-induced conversion of molecular CO_2 inside the channels to molecular CO has been postulated previously for naturally occurring radiohaloes (Nasdala et al. 2006) and also for irradiation experiments with relativistic heavy ions (Weikusat et al. 2008). A transformation from CO_2 to CO has not been observed for heating experiments (Aines and Rossman 1984) and can thus be considered as a unique effect of irradiation. Most recently, first spectroscopic evidence for molecular O_2 has been reported to occur as a radio-chemical transformation following radiation-induced disproportionation of CO_2 into CO and O_2 (Krickl et al. 2009). None of the spectra acquired during this study show the additional Raman-active band at 1,550 cm^{-1}, which would be indicative for the presence of molecular oxygen. On the other hand, the significant luminescence contribution, which arises from the use of the red laser excitation in this study, may be the reason why the mode at 1,550 cm^{-1} has not been observed. In general, the recombination of oxygen to O_2 molecules appears very likely considering how easily O_2 molecules can

be accommodated inside the cavities with a similar alignment such as that of CO and N_2.

Acknowledgements

We thank Dr. Reinhard Kaindl and one anonymous reviewer for constructive comments. We acknowledge Marcus Schrauder, Vienna, for providing us with the crystal specimens from Madagascar (sample CORTS). We thank Ilona Fin and Oliver Wienand for their careful preparation of the crystal sections, and Sandra Panienka for her help with carrying out the electron microprobe analyses. Financial support within the BMBF Verbundprojekt and GSI research grant (Bundesministerium für Bildung und Forschung, grant 05KK7VH1 to UAG) is acknowledged. Fitting was performed with the free software FITYK 0.8.9 (http://www.unipress.waw.pl/fityk/).

References

Aines RD, Rossman GR (1984) The high temperature behavior of water and carbon dioxide in cordierite and beryl. Am Mineral 69:319

Armbruster T (1985) Ar, N_2 and CO_2 in the structural cavities of cordierite, an optical and X-ray single-crystal study. Phys Chem Miner 12:233-245

Armbruster T, Bloss FD (1981) Mg-cordierite: Si/Al ordering, optical properties, and distortion. Contrib Mineral Petrol 77:332-336

Armbruster T, Bloss FD (1982) Orientation and effects of channel H_2O and CO_2 in cordierite. Am Mineral 67:284-291

Armbruster T, Bürgi HB (1982) Orientation of CO_2 in cavity of cordierite: a single-crystal X-ray study at 100 K, 300 K, and 500 K. Fortschr Mineral 60(Beih 1):37-39

Carey JW, Navrotsky A (1992) The molar enthalpy of dehydration of cordierite. Am Mineral 77:930

Carson DG, Rossman GR, Vaughan RW (1982) Orientation and motion of water molecules in cordierite: a proton nuclear magnetic resonance study. Phys Chem Miner 8:14-19

Faye GH, Manning PG, Nickel EH (1968) The polarized optical absorption spectra of tourmaline, cordierite, chloritoid and vivianite: ferric-ferrous electron interaction as a source of pleochroism. Am Mineral 53:1174-1201

Geiger CA, Rager H, Czank M (2000) Cordierite III: The site occupation and concentration of Fe^{3+}. Contrib Mineral Petrol 140:344-352

Gibbs GV (1966) The polymorphism of cordierite I: the crystal structure of low cordierite. Am Mineral 51:1068-1087

Goldmann DS, Rossman GR (1977) Channel constituents in cordierite. Am Mineral 62:1144-1157

Güttler B, Salje EKH, Putnis A (1989) Structural states of Mg cordierite III: Infrared spectroscopy and the nature of the hexagonal-modulated transition. Phys Chem Miner 16:365-373

Kaindl R, Tropper P, Deibl I (2006) A semi-quantitative technique for determina-

tion of CO_2 in cordierite by Raman spectroscopy in thin sections. Eur J Miner 18:331

Khomenko VM, Langer K (2005) Carbon oxides in cordierite channels: determination of CO_2 isotopic species and CO by single crystal IR spectroscopy. Am Mineral 90:1913-1917

Khomenko VM, Langer K, Geiger CA (2001) Structural locations of the iron ions in cordierite: a spectroscopic study. Contrib Mineral Petrol 141:381-396

Kolesov BA, Geiger CA (2000) Cordierite II: the role of CO_2 and H_2O. Am Mineral 85:1265-1274

Krickl R, Nasdala L, Wildner M, Grambole D (2008) New insights into the formation of radiohaloes: effects of artificial alpha-irradiation on cordierites. In: Proceedings of the 86^{th} annual meeting of the German mineralogical society, Berlin, Germany, Book of Abstracts, no. 210

Krickl R, Nasdala L, Grambole D, Kaindl R (2009) Radio-induced alteration in cordieriteimplications for petrology, gemmology and material science. Geophys Res Abstr, vol 11, EGU2009-2657-2, EGU General Assembly 2009 (abstr.)

Lee WE, Mitchell TE, Heuer AH (1986) Electron beam-induced phase decomposition of cordierite and enstatite. Radiat Eff 97:115-126

Liu J, Glasmacher UA, Lang M, Trautmann C, Voss K-O, Neumann R, Wagner GA, Miletich R (2008) Raman spectroscopy of apatite irradiated with swift heavy ions with and without simultaneous exertion of high pressure. Appl Phys A 91:17-22

Łodziński M, Wrzalik R, Sitarz M (2005) Micro-Raman spectroscopy studies of some accessory minerals from pegmatites of the Sowie Mts and Strzegom-Sobótka massif, Lower Silesia, Poland. J Mol Struct 744-747:1017-1026

Malcherek T, Domeneghetti MC, Tazzoli V, Ottolini L, McCammon C, Carpenter MA (2001) Structural properties of ferromagnesian cordierites. Am Mineral 86:66-79

McMillan P, Putnis A, Carpenter MA (1984) A Raman spectroscopic study of Al-Si ordering in synthetic magnesium cordierite. Phys Chem Miner 10:256-260

Mirwald PW (1982) A high-pressure phase transition in cordierite. Am Mineral 67:277-283

Nasdala L, Wildner M, Wirth R, Groschopf N, Pal DC, Möller A (2006) Alpha particle haloes in chlorite and cordierite. Mineral Petrol 86:1

Poon WCK, Putnis A, Salje E (1990) Structural states of Mg cordierite IV: Raman spectroscopy and local order parameter behaviour. J Phys: Condens Matter 2:6361-6372

Putnis A (1980) Order-modulated structures and the thermodynamics of cordierite reactions. Nature 287:128-131

Santosh M, Jackson DH, Harris NBW (1993) The significance of channel and fluid-inclusion CO_2 in cordierite: evidence from carbon isotopes. J Petrol 34:233-258

Shannon RD, Mariano AN, Rossman GR (1992) Effect of water and carbon dioxide on dielectric properties of single-crystal cordierite and comparison with polycrystalline cordierite. J Am Ceram Soc 75:2395-2399

Toulemonde M, Dufour C, Meftah A, Paumier E (2001) Transient thermal processes in heavy ion irradiation of crystalline inorganic insulators. Nucl Instrum Methods Phys Res, Sect B 166:903-912

Vance ER, Price DC (1984) Heating and radiation effects on optical and Mössbauer spectra of Fe-bearing cordierites. Phys Chem Miner 10:200-208

Vry JK, Brown PE, Valley JW (1990) Cordierite volatile content and the role of CO_2 in high-grade metamorphism. Am Mineral 75:71-88

Weikusat C, Glasmacher UA, Miletich R, Neumann R, Trautmann C (2008) Raman spectroscopy of heavy ion induced damage in cordierite. Nucl Instrum Methods Phys Res, Sect B 266:2990

Winkler B, Hennion B (1994) Low temperature dynamics of molecular H_2O in bassanite, gypsum and cordierite investigated by high resolution incoherent inelastic neutron scattering. Phys Chem Miner 21:539-545

Winkler B, Milman V, Payne MC (1994a) Orientation, location, and total energy of hydration of channel H_2O in cordierite investigated by ab initio total energy calculations. Am Mineral 79:200-204

Winkler B, Coddens G, Hennion B (1994b) Movement of channel H_2O in cordierite observed with quasi-elastic neutron scattering. Am Mineral 79:801-808

Zhang M, Salje EKH, Farnan I, Graeme-Barber A, Daniel P, Ewing RC, Clark AM, Leroux H (2000) Metamictization of zircon: Raman spectroscopic study. J Phys: Condens Matter 12:1915- 1925

Ziegler JF, Biersack JP, Littmark U (1985) The stopping and range of ions in solids. Pergamon, New York

Zimmermann JL (1981) La libération de l'eau, du gaz carbonique et des hydrocarbures des cordierites. Cinétique des méchanismes, détermination des sites, intérêt pétrogénétique. Bull Miner 104:325-338

wt.%	CORTS	CORMB1	p.f.u.	CORTS	CORMB1
SiO_2	50.23	50.34	Si	4.995	4.998
Al_2O_3	33.83	33.93	Al	3.960	3.962
FeO	1.44	2.11	Fe	0.122	0.175
MnO	0.02	0.02	Mn	0.002	0.002
MgO	12.88	12.72	Mg	1.924	1.880
CaO	0.01	0.03	Ca	0.001	0.003
Na_2O	0.16	0.14	Na	0.031	0.026
K_2O	0.03	0.04	K	0.003	0.005
$\sum$	98.60	99.33	O	18.000	18.000
CO_2	0.55	0.41	CO_2	0.074	0.055
H_2O[a]	0.85	0.26	H_2O	0.562	0.172

Crystal chemical formulae: CORTS: $Na_{0.031}K_{0.003}Ca_{0.001}[^{[6]}(Mg_{1.924}Fe^{2+}_{0.122}Mn_{0.002})_{\Sigma 2.048}{}^{[4]}(Si_{4.995}Al_{3.960})_{\sum 8.995}O_{18}] \cdot (H_2O)_{0.562}(CO_2)_{0.074}$, CORMB1: $Na_{0.026}K_{0.005}Ca_{0.003}[^{[6]}(Mg_{1.880}Fe^{2+}_{0.175}Mn_{0.002})_{\Sigma 2.057}{}^{[4]}(Si_{4.988}Al_{3.962})_{\Sigma 8.950}O_{18}] \cdot (H_2O)_{0.172}(CO_2)_{0.055}$

[a] Calculated from $100 - (\Sigma + CO_2)$

Table 1 Chemical composition of samples obtained by microprobe analyses

Sample	Irradiation direction	Ion	Fluence (ions/cm^2)	Initial ion energy (MeV/u)	Initial energy loss (keV/nm)	Ion range (μm)
CORMB1	//[100]	^{208}Pb	5×10^{11}	8	25	72
			7×10^{11}			
			1×10^{12}			
			2×10^{12}			
CORTS	//[100]	^{197}Au	6×10^{11}	11.1	23	90
			2×10^{12}			
	//[010]	^{197}Au	6×10^{11}	11.1	23	90
			2×10^{12}			
	//[001]	^{197}Au	6×10^{11}	11.1	23	90
			2×10^{12}			

Table 2 Irradiation parameters; energy loss and ion range were calculated with SRIM2008 (Ziegler et al. 1985)

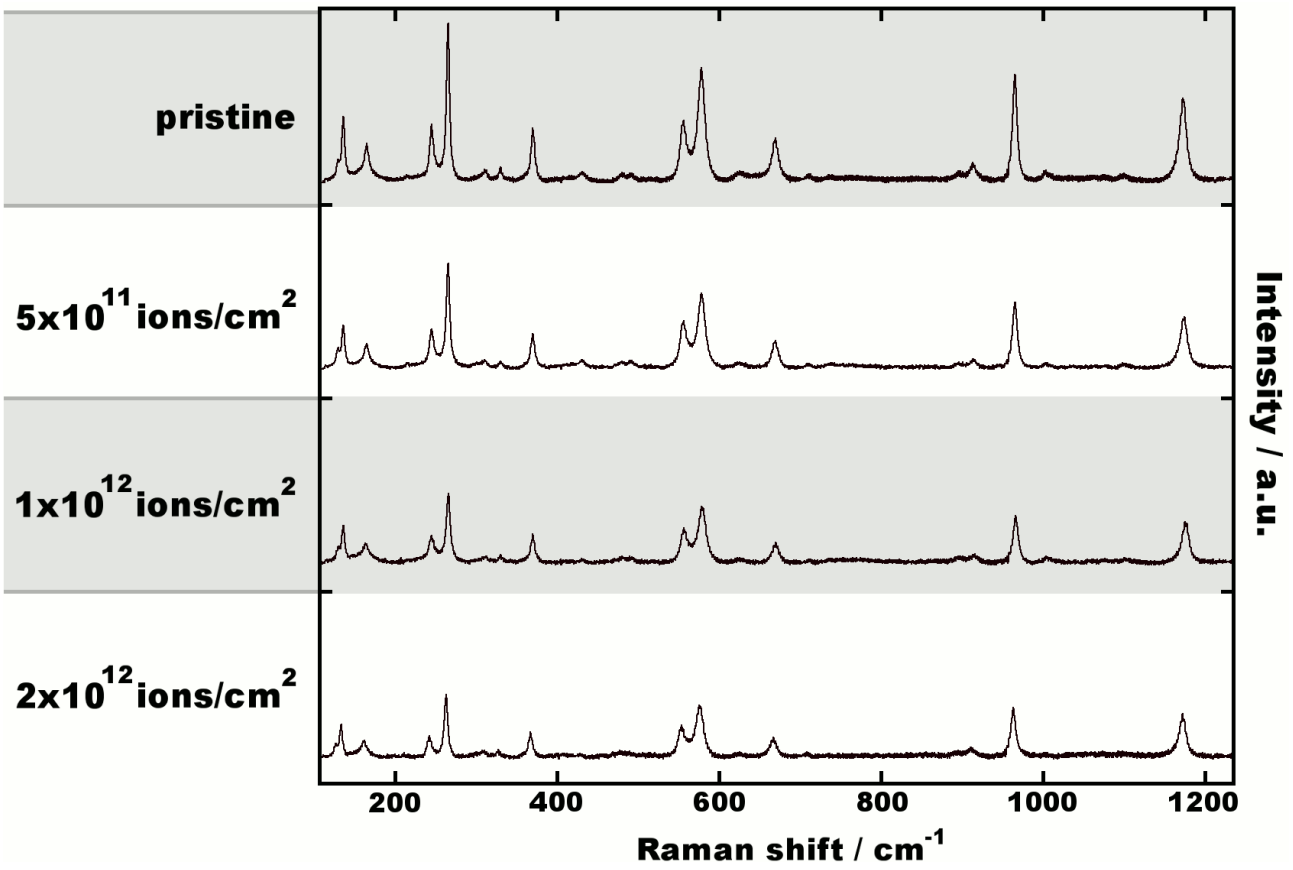

Fig. 1 Raman spectra of oriented cordierite sample CORMB1 irradiated parallel to [100] with different fluences of Pb ions (energy 1.6 GeV)

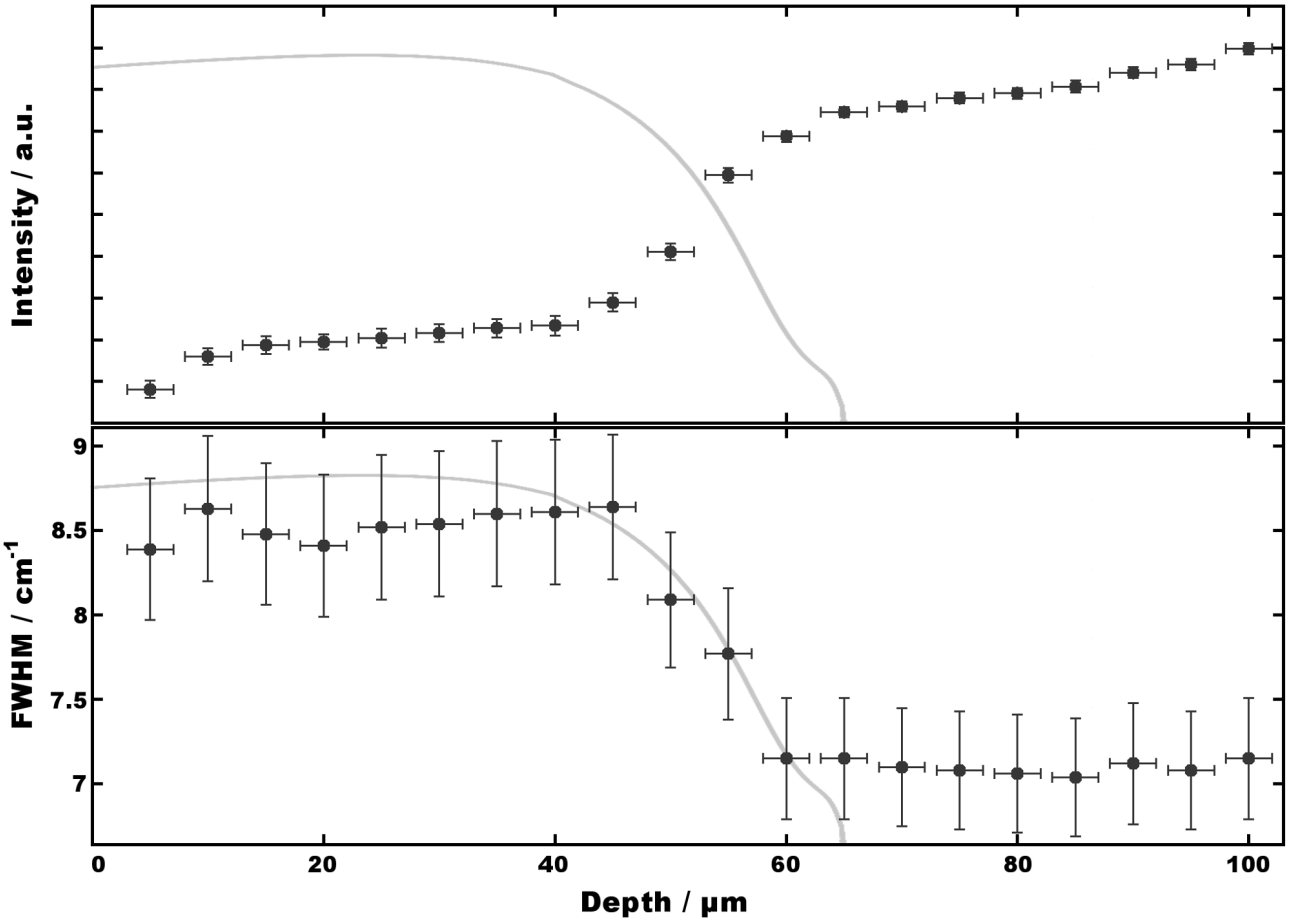

Fig. 2 Evolution of band area and FWHM of the ∼972 cm^{-1} band (probably SiO_4 stretching, Łodziński et al. 2005) as a function of depth (distance from the irradiated surface). The trends are similar for all bands. The sample (CORMB1) was irradiated with 1×10^{12} Pb ions/cm^2 (energy 1.6 GeV). Data points are mean values of several measurements, *error bars* show standard deviations. *Solid line* Electronic energy loss dE/dx of the ions calculated with SRIM2008

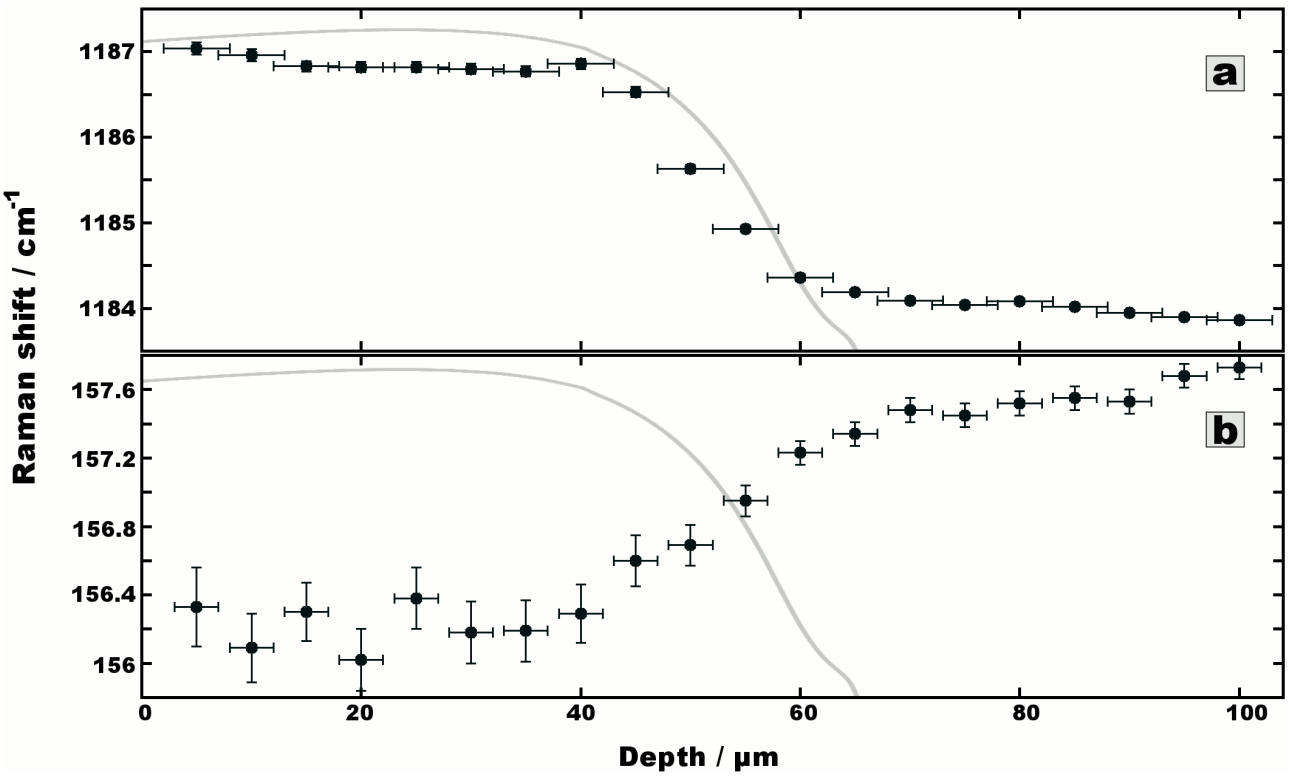

Fig. 3 Evolution of peak positions of **a** ∼1,184 cm^{-1} band, probably SiO_4 stretching, **b** ∼158 cm^{-1} band, possibly rotational (Łodziński et al. 2005) as a function of depth (distance from the irradiated surface), showing rather different trends. The sample (CORMB1) was irradiated with 1×10^{12} Pb ions/cm^2 (energy 1.6 GeV). Data points are mean values of several measurements, *error bars* show standard deviations. *Solid line* Electronic energy loss dE/dx of the ions calculated with SRIM2008

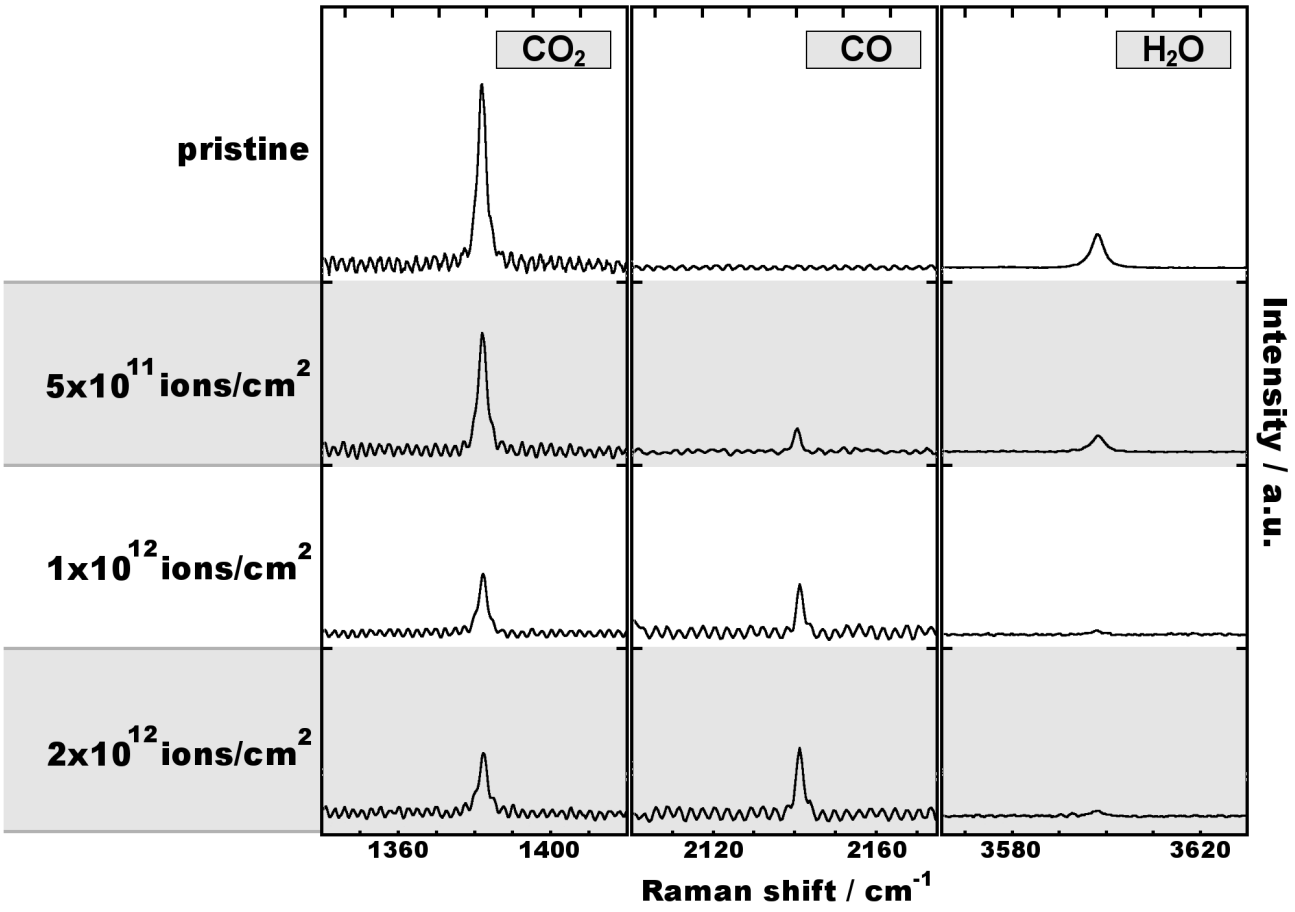

Fig. 4 Intensity of the symmetric stretching modes of CO_2 (1,382 cm^{-1}), CO (2,135 cm^{-1}) and class I H_2O (3,198 cm^{-1}) for different fluences. The loss of H_2O and CO_2 and the related increase of CO with increasing fluence are clearly visible. The intensity ratios of the bands are shown as they appear in the spectra. The sample (CORMB1) was irradiated with Pb ions (energy 1.6 GeV)

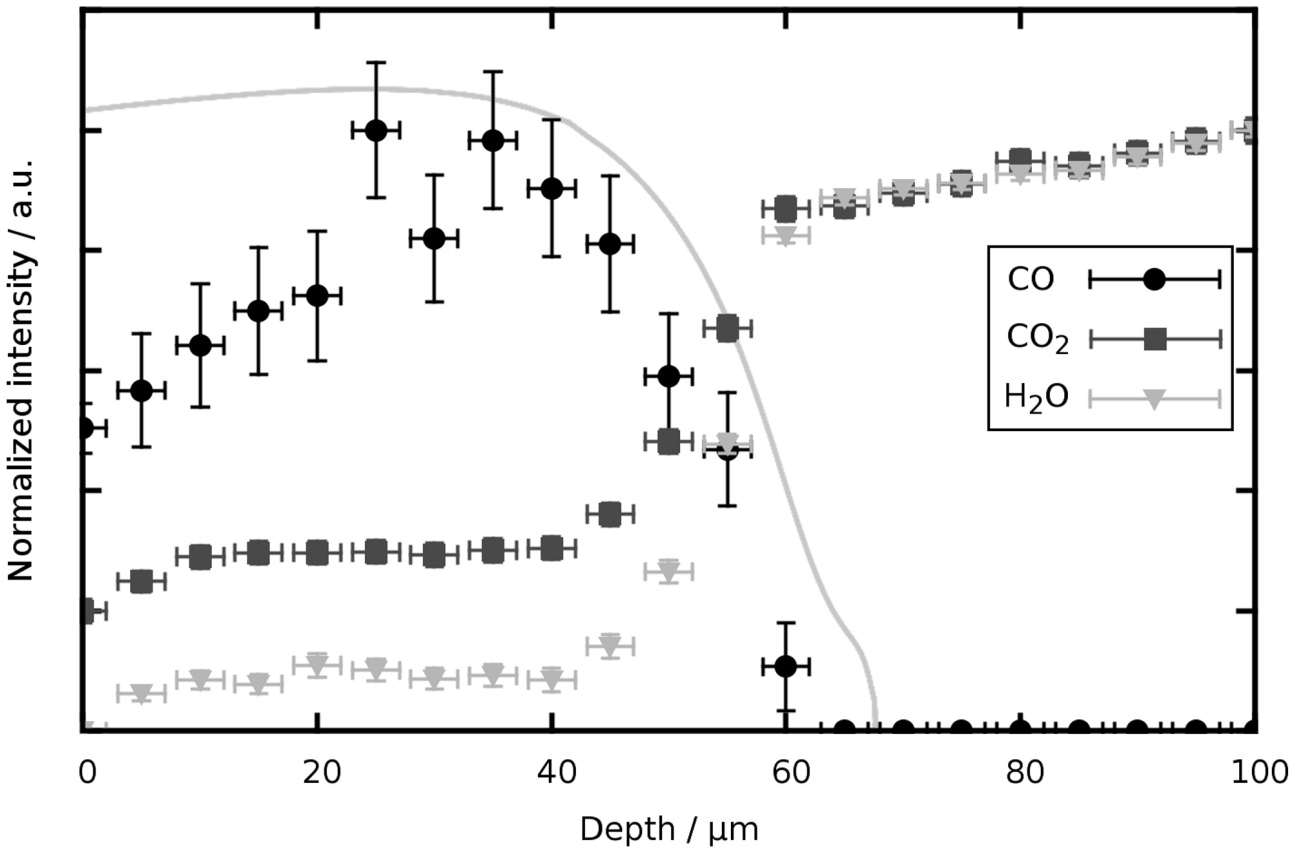

Fig. 5 Normalised intensity of the symmetric stretching modes of CO (2,135 cm^{-1}), CO_2 (1,382 cm^{-1}) and class I H_2O (3,198 cm^{-1}) as a function of depth (distance from the irradiated surface). The trends are similar for all fluences and orientations. The sample (CORMB1) was irradiated with 1×10^{12} Pb ions/cm^2 (energy 1.6 GeV). *Solid line* Electronic energy loss dE/dx of the ions calculated with SRIM2008

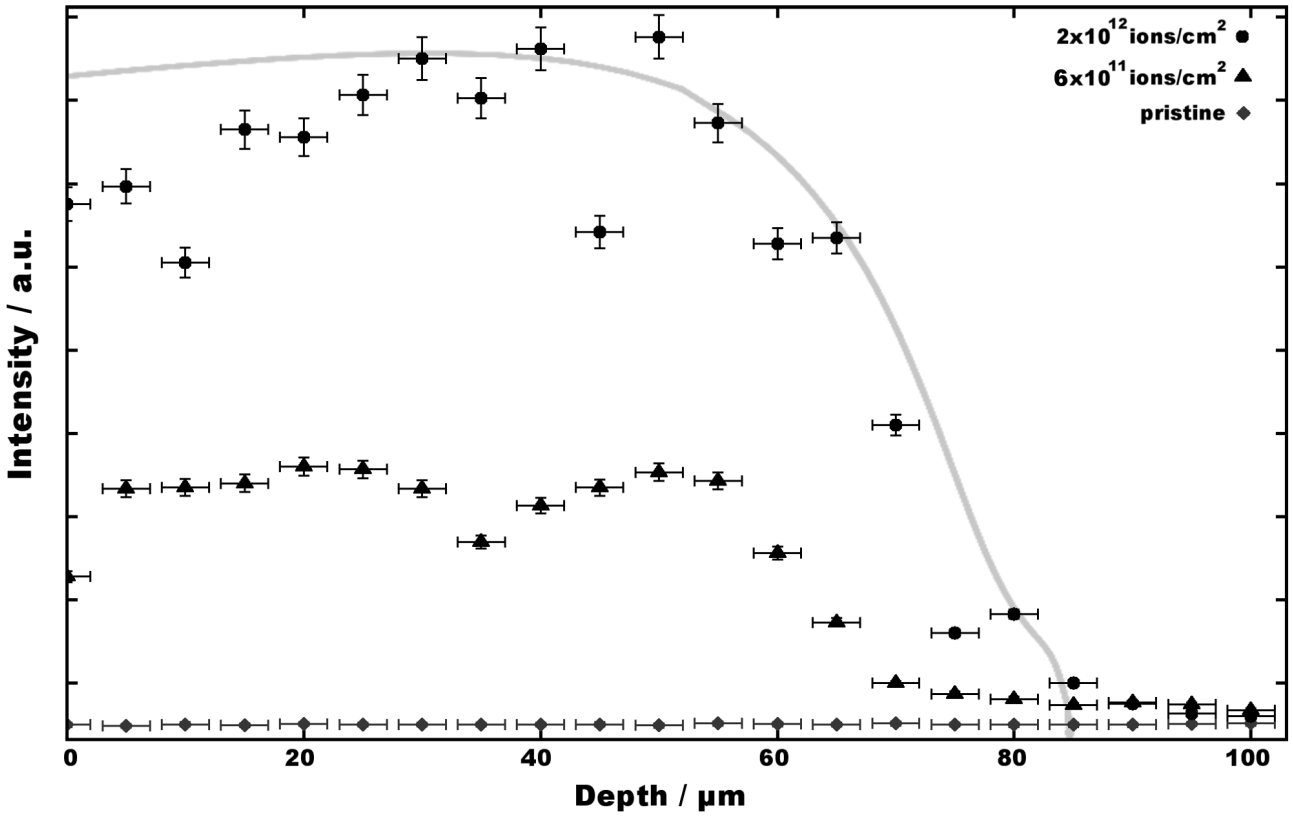

Fig. 6 Evolution of luminescence background (intensity at 830 nm) as a function of depth (distance from the irradiated surface) and different fluences. The data are presented as acquired, without any corrections or modifications. The sample (CORTS) was irradiated with Au ions (energy: 2.2 GeV). *Solid line* Electronic energy loss dE/dx of the ions calculated with SRIM2008

Appendix C

Publication III - Experimental heavy-ion irradiation in the Paris-Edinburgh press: first results (*abstract*)

C. Weikusat, M. Burchard, S. Klotz, R. Miletich, U.A. Glasmacher, C. Trautmann, R. Neumann (2009)

International Conference on High Pressure Science and Technology
Joint AIRAPT-22 & HPCJ-50, Odaiba, Tokyo, JAPAN
Review of High Pressure Science and Technology, Vol. 19

1. Introduction

Up to now, diamond anvil cells (DAC) have been used for irradiation experiments with swift heavy ions and the simultaneous application of high pressures (*e.g.* [1]). While allowing the application of spectroscopic measurements inside the cell, the drawback of the DAC is the extremely small maximum sample size (in the μm range). Various measurement techniques and also possible industrial applications require larger volumes of irradiated matrial. We hereby present the results of the first successful swift heavy ion irradiation inside a large volume Paris-Edinburgh press.

2. Experimental procedures

Zircon was chosen because of its well documented and reliable sensitivity for radiation induced damage, which can easily be detected by Raman spectroscopy [2]. The zircons were heated prior to the experiment to remove any traces of previous radiation damage. A pressure of $\sim$6 GPa was applied. The press was irradiated with Xe ions with kinetic energy of 300 MeV/u. The applied fluence was 1.5×10^{12} ions/cm^2. After the irradiation, the sample chamber was opened carefully and the crystals were extracted under an optical microscope. Raman spectra of the irradiated crystals and pristine zircons from the same batch were acquired with identical measurement parameters. Voigt functions were fitted to each band.

3. Results

Comparison of the Raman spectra of irradiated and pristine zircons (Fig. 1) reveals a significant decrease of band intensity after irradiation. Fitting of each band furthermore shows an increase of the band width while the band center is shifted to lower wavenumbers (Table 1). These are the characteristic signs of radiation damage in zircon [2]. We will present results of the spectroscopic measurements as well as details and planned further improvements of the experimental setup.

References

[1] U.A. Glasmacher, M. Lang, H. Keppler, F. Langenhorst, R. Neumann, D. Schardt, C. Trautmann, G.A. Wagner, Phys. Rev. Lett., 96, 195701 (2006).

[2] M. Zhang, E.K.H. Salje, I. Farnan, A. Graeme- Barber, P. Daniel, R.C. Ewing, A.M. Clark, H. Leroux, J. Phys.: Condens. Matter, 12, 1915 (2000).

pristine		irradiated	
Center	**FWHM**	**Center**	**FWHM**
201.6 cm^{-1}	2 cm^{-1}	201.2 cm^{-1}	3 cm^{-1}
213.8 cm^{-1}	3 cm^{-1}	213.3 cm^{-1}	5 cm^{-1}
224.5 cm^{-1}	3 cm^{-1}	224.2 cm^{-1}	6 cm^{-1}
356.3 cm^{-1}	4 cm^{-1}	355.4 cm^{-1}	10 cm^{-1}
439.7 cm^{-1}	6 cm^{-1}	439.2 cm^{-1}	7 cm^{-1}
974.8 cm^{-1}	2 cm^{-1}	974.3 cm^{-1}	8 cm^{-1}
1008.2 cm^{-1}	2 cm^{-1}	1007.4 cm^{-1}	8 cm^{-1}

Table 1. Comparison of band parameters

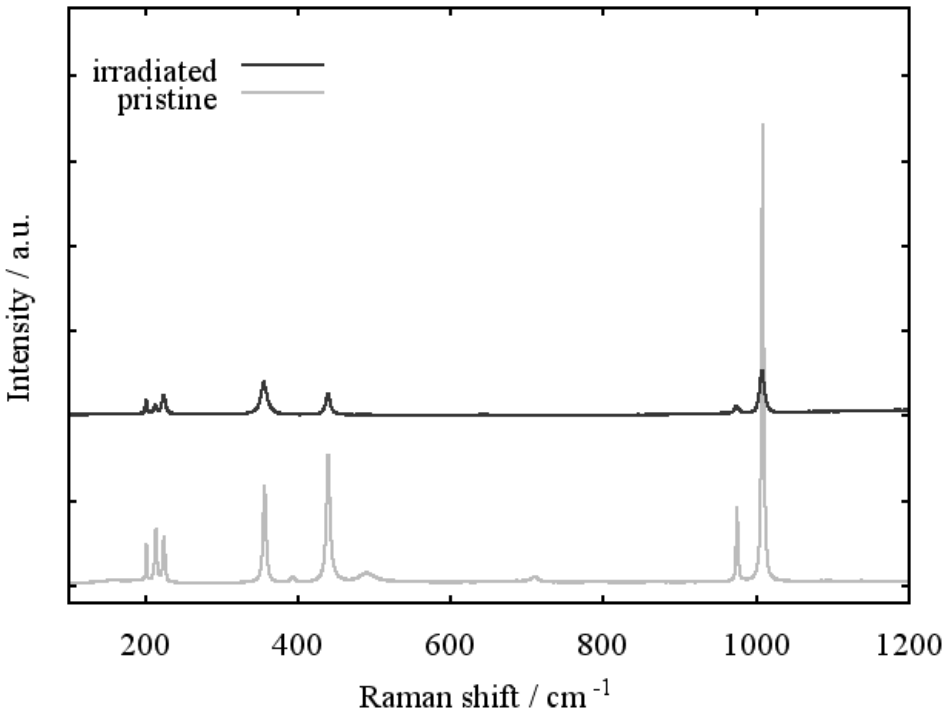

Figure 1. Raman spectra of zircon before and after irradiation

Appendix D

Publication IV - Raman study of apatite amorphised with swift heavy ions under various irradiation conditions

C. Weikusat, U.A. Glasmacher, R. Miletich, B. Schuster, C. Trautmann, R. Neumann (2010)
Submitted to Physics and Chemistry of Minerals, February 2010.

Abstract

Crystallographically oriented Durango fluorapatites were exposed to swift heavy ions (Xe, Ta, Au) at different irradiation conditions, focussing on the effect of fluence (10^9 - 10^{13} ions/cm^2), electronic energy loss on the sample surface (18 to 27 keV/nm), and hydrostatic pressures (3.6 - 11.5 GPa) applied during irradiation. In-situ high-pressure irradiation were performed in diamond anvil cells. Confocal Raman spectroscopy was used to trace the radiation-induced changes in the crystal lattice. Fragmentation of the crystal specimen was found to scale with energy loss and fluence. Apparently, it also depends on the orientation and sample thickness. In general, the radiation damage for irradiation along the c-axis was found to be larger than for the <hk0> direction, independent on the confining pressure. Observations on samples irradiated at high pressures indicate a stabilising effect, leading to a reduced amorphisation rate in comparison to the samples irradiated without pressure.

Introduction

The occurrence of fission tracks in natural apatite and the demand of understanding the conditions, which control formation of damages originating from relativistic particles, has motivated a series of studies on experimental irradiation. We now exposed pressurised natural fluorapatite crystals to various high-energy ions, complementing earlier experiments by Liu et al. (2008) by using strictly oriented crystals and ions of other energy losses. Two fluence series were acquired, ranging from 1×10^{11} ions/cm^2 to 1×10^{13} ions/cm^2 for irradiations with Xe ions and from 1×10^{9} ions/cm^2 to 1×10^{12} ions/cm^2 for irradiations with Ta ions. Additional irradiations with Au ions were undertaken to evaluate the influence of orientation on the damage production, as the morphology and physical properties of radiation-induced tracks are known to be sensitive to the crystallographic orientation (*e.g.* Donelick 1991, Barbarand et al. 2000). Reliable statements about any of these properties and, especially, comparisons of data acquired in several experiments with different samples therefore critically depend on a well-defined orientation of the starting material. Applying different swift heavy ions, the dE/dx values ranged from about 18 keV/nm (Xe) to 27 keV/nm (Au) on the sample surface. The electronic energy loss of the projectiles inside the target has been found to be of major importance for the mechanisms involved in track registration. Villa et al. (2000) found a critical threshold of 4.5 keV/nm for the first occurrence of etchable damage in apatite. Besides that, they could show that the damage morphology of the track also depends on dE/dx and that complete amorphisation, and thus a continuously etchable track, is achieved above an energy loss of 12 keV/nm. The track radii were found to increase with energy loss and ranged from r=0.9 nm (dE/dx=4.5 keV/nm) to r=6.3 nm (dE/dx=14 keV/nm) (Villa et al. 1999, 2000). The energies of all ion beams used in our present study were accordingly adjusted

to provide energy losses well above this amorphisation threshold.

Irradiations under high-pressure conditions were motivated by the possible benefits for the fission-track dating technique. Apatite from the iron-ore deposit at the Cerra de Mercado mine in Durango, Mexico is a widely accepted standard for fission-track dating (Young et al. 1969; Wagner and van den Haute 1992, and references therein), and as the energy of the swift heavy ions produced in modern accelerator facilities can be adjusted to match the energy of typical fission fragments, irradiation experiments can provide suitable beams to simulate fission track formation in natural minerals under well-controlled conditions, including the crystallographic orientation of the sample to the incident beam. In recent experimental setups, pressure and temperature have been added as additional parameters, aiming at the realistic simulation of naturally occurring track formation processes (*cf.* Lang et al. 2008a). While the pressure window for the occurrence of natural fission-tracks in apatite is rather narrow (as, under geologic conditions, a rise in pressure is always accompanied by rising temperatures, which cause healing of the tracks and other lattice defects, scaling with the duration of exposure (*e.g.* Bertel and Märk 1983; Green et al. 1985, 1986; Sandhu et al. 1990; Crowley et al. 1990, 1991; Carlson et al. 1999; Villa et al. 2000; Barbarand et al. 2003)), the combination of high-pressure techniques with the extremely high energies available from modern heavy-ion synchrotrons promises unprecedented possibilities for fundamental investigations utilising much wider ranges of pressure conditions. However, given the challenging experimental requirements, to date only few studies have investigated the effects of pressure during ion irradiation in a limited number of materials (*i.e.* apatite, graphite, pyrochlore, zircon and zirconia) (Glasmacher et al. 2006; Liu et al. 2008; Lang et al. 2008a, b, 2009a, b; Schuster et al. 2009). The external pressures applied in this study are much larger than the relevant geologic pressures. Although direct conclusions about natural track formation are therefore not possible, we hope to contribute to establishing reliable foundations for an advanced understanding of the interaction between high pressures and radiation-induced damage production in apatite. Another important field of research that will profit from a better understanding of radiative processes in apatite is nuclear waste management. The ongoing search for suitable materials for the long-term inactivation of radioactive wastes will certainly become even more important in the coming years. Due to the potential of incorporating actinide elements into their structure, apatite type minerals are promising candidates for a leastwise mid-term inactivation of radioactive substances. Apatite is also known to crystallise from calcium- and phosphorous-bearing glasses subjected to prolonged radiation. A better understanding of radiation-induced changes to the apatite lattice is crucial for a treatment of these problems. Several studies have therefore investigated amorphisation processes and other structural changes in apatite under well-defined ambient and high-temperature conditions (*e.g.* Wang et al. 1993; Weber et al. 1997, 1998, 2000).

In this study, we applied Raman spectroscopy as a fast and easy tool for the

evaluation of radiation-induced changes to the crystal lattice. Furthermore, we present some data about the combined effects of high pressures and heavy ion irradiation on apatite.

Experimental

The samples are natural yellow-coloured and macroscopically inclusion-free euhedral fluorapatite single crystals from the Cerro de Mercado Iron Deposit, Durango District, Mexico (Young et al. 1969). The selected specimen originate from the same sample batch used and analysed by Schouwink et al. (2009), corresponding to a 95 mol-% fluorapatite endmember composition with trace contents of Na, La, Ce, Nd, Si and S. All samples were oriented in either $(10\bar{1}0)$ or (0001) direction by optical methods and following occurring crystal faces. The oriented samples were polished to thicknesses of about 30 μm (DAC and vacuum conditions) and 5-10 mm (only vacuum conditions), respectively. While the former samples are thinner than the penetration depth of the ions, and are thus only affected by the electronic energy loss, the latter are substantially thicker and also experience atomic displacement cascades due to nuclear stopping at the end of the ion trajectory (see Table 1 for details). Prior to irradiation, all samples were annealed for 24 hours at 430 °C to remove lattice defects caused by natural irradiation (annealed samples are hereafter denoted as 'non-irradiated'). Samples for the in-situ irradiations at pressures of 3.6 GPa and 4.9 GPa were loaded into screw-driven HT-microscope DACs (modified Diacell μScope-DAC type, easyLab technologies Ltd, UK), for 11.5 GPa into an ETH type DAC (Miletich et al. 2000), using anvils with culet sizes of 600 and 300 μm, respectively. Stainless steel gaskets (initial thickness 250 μm) were preindented to 100 and 90 μm, the actual sample chambers had diameters of 200 and 150 μm. A 4:1 methanol-ethanol mixture was used as pressure medium and ruby chips were added for pressure calibration, which was accomplished by monitoring the pressure-induced shift of the ruby luminescence lines (*cf.* Mao et al. 1986). To check for the effects of crystal orientation on the damage production, two oriented fragments of polished crystal plates were loaded into each DAC, for beam incidences parallel $(10\bar{1}0)$ and parallel (0001).

All irradiation experiments were carried out at the GSI Helmholtz Centre for Heavy Ion Research in Darmstadt. Most samples were exposed to 11.1 MeV/u ions under vacuum conditions at the X0 beamline of the linear accelerator (UNILAC). All samples were irradiated at room temperature and under normal beam incidence. High-pressure irradiations were performed at Cave A with beams of initial energies of 155 MeV/u (Xe) and 175 MeV/u (U) at the heavy-ion synchrotron (SIS). Due to the limited beamtime available, especially at the SIS, fluences above 1×10^{12} ions/cm^2 could only be reached for few samples. The electronic energy losses and related penetration depths of the ions were calculated with the SRIM2008 code, providing an estimated accuracy of 10-20% (Ziegler et al. 1985). For the UNILAC experiments, the energy loss at the sample surface was about

18 keV/nm for Xe ions and 27 keV/nm for Au ions. In the case of irradiation of pressurised DACs, the ions have first to transverse about 50 cm of air (distance between beam exit window and DAC) and subsequently penetrate through the top diamond anvil before reaching the sample inside the pressure chamber. The initial beam energy was selected in such a way that the energy loss on the sample surface was about 18 keV/nm. This allows for direct comparison with the non-pressurised samples irradiated with Xe ions at the UNILAC (*cf.* Table 1). Fluences were monitored online with SETRAM secondary electron detectors, which were calibrated by the total charge of the ions measured in a Faraday cup. The flux of the irradiations was limited to prevent heating of the bulk sample.

Raman spectra in the range between 100 and 1600 cm^{-1} were recorded under backscattering geometry using a LabRam HR800 UV spectrometer equipped with an OLYMPUS BXFM-ILHS optical microscope, automated x-y stage, a grating with 1800 grooves per millimetre and Peltier-cooled CCD detector. The spectra were excited using the 632.8 nm line of a He-Ne laser. The lateral resolution was $\sim$1 μm, the wavenumber accuracy was 0.5 cm^{-1} and the spectral resolution was estimated below 2 cm^{-1}. Spectra of the pressurised samples inside the DACs where routinely acquired but showed no signs of possible phase transformations or breakdown reactions (*cf.* Xie et al. 2003; Konzett and Frost 2009). For quantitative comparison with reference samples irradiated under vacuum conditions, detailed spectra of the samples irradiated under pressure were recorded only after pressure release and extraction of the samples from the DACs. Parameters of the Raman bands, such as area, position and width (full width at half maximum, FWHM) were deduced by deconvolution and least-squares fitting of Voigt functions to each band.

Results and discussion

Visual observations

All samples irradiated without pressure and fluences around and above 1×10^{11} ions/cm^2 developed optically resolvable micro-cracks, caused by changes in lattice dimensions and associated strain gradients originating from the production of amorphous tracks along the ion trajectories (Miro et al. 2005; Liu et al. 2008; Schouwink et al. 2009). Sample fragmentation becomes more pronounced with higher energy loss and, for a given dE/dx, with increasing fluence. Starting at fluences of about 5×10^{11} ions/cm^2, the cracks become large enough to be macroscopically visible. At higher fluences, the crack density increases and the fractures tend to form networks, resulting in an increasingly inhomogeneous damage distribution. At about 1×10^{12} ions/cm^2, extensive cracking and domains of complete fragmentation can be seen throughout the sample (Fig. 1).

Samples substantially thicker than the penetration depth of the ions were additionally affected by direct atomic displacement damage due to nuclear stopping

towards the end of the ion trajectory. In those samples, cracks started to develop at lower fluences and ultimately lead to complete fragmentation. For the series irradiated with Ta ions (samples U-20 – U-24, 1×10^{9} – 1×10^{12} ions/cm^2, dE/dx≈24 keV/nm), macroscopic cracks already appeared at 1×10^{11} ions/cm^2. The sample irradiated with 1×10^{12} ions/cm^2 (U-24) suffered complete fragmentation and could not be recovered for further measurements.

All samples irradiated parallel to the c-axis are more damaged than samples irradiated perpendicular to the c-axis under otherwise identical conditions. This also holds true for the samples irradiated under pressure. Sample 17B-H pressurised at 11.5 GPa and irradiated parallel c with 1×10^{12} Xe ions/cm^2 (dE/dx≈18 keV/nm) suffered complete fragmentation, while the other orientation (beam perpendicular c) shows comparably small fragmentation with only few and very weak cracks. However, for a pressure of 4.91 GPa and irradiation with 1×10^{12} U ions/cm^2 (sample 17B-H, dE/dx≈18 keV/nm), both sample orientations are likewise completely fragmented and could not be separated for further analysis.

Raman spectroscopy

According to earlier Raman studies by researchers from many different fields of science (*e.g.* Kravitz et al. 1968; Boyer and Fleury 1974; Devarajan and Klee 1981; Tsuda and Arends 1994; Williams and Knittle 1996; Penel et al. 1998; Comodi et al. 2001; Zattin et al. 2007; Liu et al. 2008; Schouwink et al. 2009), the most prominent features in the Raman spectra of apatite are related to vibrations of the PO_4 tetrahedra. The bands can be attributed to the following phonon modes: ∼964 cm^{-1} to the ν_1 symmetric stretching vibration of phosphate anions (this is the most intense mode in the apatite spectrum, *cf.* Fig. 2), ∼430 and ∼453 cm^{-1} to the ν_2 symmetric out-of-plane bending modes, ∼1052 and ∼1081 cm^{-1} to the ν_3 antisymmetric stretching modes, and ∼591 and ∼608 cm^{-1} to ν_4 antisymmetric bending (*e.g.* Comodi et al. 2001). The very weak bands below 400 cm^{-1} are most probably related to lattice modes. In most cases, the increased luminescence background prevents the identification of these modes in the spectra of the irradiated samples. We therefore concentrated exclusively on the sufficiently intense vibrational modes of the phosphate tetrahedral units. Information about lattice imperfections, in particular related to crystal mosaicity, internal strain gradients and defects associated with the short-range order, can be obtained from widths and intensities of these modes. In general, intensity loss and broadening of bands compared to non-irradiated apatite are related to an increasing number of defects and simultaneously decreasing short-range order in the crystal. Accordingly, samples irradiated with fluences above 1×10^{11} U ions/cm^2 exhibit decreased intensities and broadened FWHMs. The evolutions of each parameter follow similar exponential trends when plotted against fluence (Fig. 3 and Fig. 4).

The exact peak positions may vary due to factors such as mechanical stress or chemical composition (*e.g.* O'Shea et al. 1974). Monitoring the peak shift

of the Raman bands, respective information about stress distributions inside a crystal lattice and the causative radiation damage become accessible. In many crystalline solids, ion-induced tracks consist of amorphous cylinders displaying a decreased mass density compared to the starting crystal. Sample swelling and the production of internal stress gradients are direct consequences of this volume mismatch (*e.g.* Weber et al. 1998; Trautmann et al. 2000, 2002; Jaskierowicz et al. 2004; Schouwink et al. 2009). The host lattice experiences more and more stress when the number of tracks increases. This causes the peak positions of the Raman bands to shift to lower wavenumbers. Figure 5 illustrates this trend for selected apatite Raman bands, showing the peak shifts as a function of fluence. While the trend is similar to the changes of intensity and band width described above, the interpretation of stress-induced peak shifts has to be approached carefully. The abundant mechanical cracking observed might lead to pressure release, significantly changing the internal stress distribution of the sample. Peak shift data acquired from partly fragmented samples might therefore be significantly biased. Fitting exponential functions to the data, the effects of intensity loss and peak broadening can be seen to follow a rather steep trend for fluences below 1×10^{12} ions/cm^2, after which they reach saturation at around 2×10^{12} ions/cm^2. The evaluation of these changes should allow for a direct quantification of the amount amorphised domains. Similar protocols have been used to model the increase of the amorphised surface rate with a Poisson's law, depending on fluence and the amorphisation effective radius R_e (Toulemonde 1995; Villa et al. 1999, 2000). Applying these calculations to the data of the xenon fluence series yields R_e values ranging from 3.3 nm to 4.5 nm.

Starting with fluences around 1×10^{11} ions/cm^2 for high dE/dx (>20 keV/nm) ions and with 5×10^{11} ions/cm^2 for lower dE/dx (<20 keV/nm) ions, a new broad band, centred at ~950 cm^{-1} can be detected. It grows with increasing fluence, while the intensity of the neighbouring ν_1 band (964 cm^{-1}) decreases accordingly (Fig. 2). This broad band has been interpreted as the spectral contribution of the amorphous cores of the ion-induced tracks (*cf.* "ν_{1b}" Liu et al. 2008; Schouwink et al. 2009). A thorough analysis of its growth could therefore be used to quantify the amount of amorphisation in the sample. However, the intensities of Raman bands in general depend on many factors (including *e.g.* crystallinity, surface quality and measurement conditions), rendering a direct comparison of absolute intensities of different Raman measurements unreliable. We therefore used the intensity ratio of the amorphous broad band ν_{1b} to the ν_1 symmetric stretching vibration of the phosphate anions at 964 cm^{-1} as a semi-quantitative approach for comparison between different samples. Figure 6 illustrates the results as a function of fluence. The role of electronic energy loss for amorphisation is directly evident by the dramatic increase of amorphisation for high dE/dx ions above fluences around 1×10^{12} ions/cm^2. The trends are similar for all samples, the amount of amorphisation scales with fluence and the energy loss of the incident ions. Nevertheless, even the sample irradiated with the highest fluence (17B-H, 1×10^{13} Xe

ions/cm^2, dE/dx≈18 keV/nm) still shows the Raman bands of crystalline apatite. In agreement with the results of previous studies, a complete radiation-induced amorphisation of apatites could not be achieved. This is probably due to small but distinct recrystallisation processes activated by beam-induced local heating of the sample (thermal spike) (Tisserand et al. 2004; Miro et al. 2005; Liu et al. 2008).

Irradiations at non-ambient pressures

For all pressurised samples, Raman band intensities are decreased after irradiation, although the magnitude of this decrease is small compared to the samples irradiated at vacuum conditions. The crystals irradiated parallel to the c-axis seem to show a slight trend for a higher degree of damage than the samples irradiated perpendicular to the c-axis, but, at least up to a fluence of 1×10^{12} ions/cm^2, the effect is not significant enough to be quantified. While peak positions and FWHMs of the irradiated samples display distinct differences when compared to the non-irradiated material, the changes do not seem to follow a systematic trend, but show rather arbitrary fluctuations.

The evaluation of amorphisation via the analysis of the ν_{1b} / ν_1 ratio (as described above) provides information about changes of the crystallinity. The samples irradiated at a pressure of 3.6 GPa (17B-H, dE/dx≈18 keV/nm, 1×10^{11} ions/cm^2) were below the critical fluence for the detection of the ν_{1b} broad band. Both samples pressurised to 4.91 GPa and irradiated with uranium ions (17B-H, 1×10^{12} ions/cm^2, dE/dx≈18 keV/nm) were completely fragmented during irradiation and could not be recovered from the sample chamber. Finally, the two samples pressurised to 11.5 GPa were irradiated with a fluence of 1×10^{12} Xe ions/cm^2 (17B-H, dE/dx≈18 keV/nm), which is well inside the range for the detection of the ν_{1b} band (*cf.* Fig. 6). The sample irradiated perpendicular to the c-axis (17B-H, dE/dx≈18 keV/nm, 1×10^{12} ions/cm^2) shows only weak fragmentation and, in stark contrast to the reference sample irradiated under vacuum conditions, no trace of the amorphous broad ν_{1b} band could be found (Fig. 6, inset). The crystal irradiated parallel c was completely fragmented after the experiment and could not be recovered.

Conclusion

The cracking observed in most samples and the increasing amount of macroscopic damage with increasing fluence seem to be associated with the strain due to the volume differences between the non-irradiated host lattice and amorphous ion tracks. Because of the additional damage from atomic collision cascades caused by nuclear stopping at the end of the ion trajectory, this effect is significantly enhanced, when the sample thickness exceeds the penetration depth of the ions and can ultimately

lead to complete and irreversible fragmentation of the sample. To avoid fragmentation at high fluences of swift heavy ions, it is therefore advisable to use samples with thicknesses not exceeding the penetration depth of the ions.

Raman spectroscopy has been shown to be a suitable tool for the detection of the decrease of short-range order induced by swift heavy ions. It is a sensitive method, able to detect radiation-induced structural changes at fluences even below 5×10^{11} ions/cm^2 (for dE/dx$\approx$18 keV/nm), where the distinct features of amorphisation (namely the appearance and growth of the ν_{1b} broad band at $\sim$950 cm^{-1}) are not yet detectable. The decay of band intensities and the broadening of the bands are reliable indicators for radiation-induced damage. The change of peak positions with increasing fluence (*i.e.* increasing number of tracks and thus increasing stress on the host lattice) can also be measured at low fluences, but may become rather unreliable for mechanically cracked samples, were the appearance of more and more micro- and macrocracks can release the internal strain gradients.

In general, the extensive decay of band intensity in the high-fluence samples makes the deconvolution of individual weaker bands rather difficult. The strongest band (ν_1, $\sim$964 cm^{-1}) remains detectable, at least up to a fluence of 1×10^{13} ions/cm^2. At fluences above 5×10^{11} ions/cm^2, the intensity of the ν_1 band conspicuously deteriorates, accompanied by the first appearance and subsequent growth of the amorphisation related ν_{1b} broad band. Applying calculations described by Villa et al. (1999), we found values for the amorphisation effective radius R$_e$ between 3.3 nm and 4.5 nm. Villa et al. (1999) gave evidence, that R$_e$ increases proportional to the energy loss and they calculated values of R$_e$=6.5 nm for ions with dE/dx=14 keV/nm. The discrepancy of our results is possibly due to an enhanced sensitivity of Raman spectroscopy to small-scale changes of the crystal lattice in zones not necessarily connected to the transition between track and apatite matrix. It seems that this protocol cannot be directly transferred to Raman spectroscopy. However, the evaluation of the ν_{1b}/ν_1 ratio can give at least a qualitative overview of the factors influencing amorphisability. It is clear from our results that an increase of electronic stopping power leads to an enhanced amorphisation rate. The application of external pressure during irradiation has the opposite effect of stabilising the lattice against radiation-induced damage. The possible orientation dependence of track production and annealing rates has often been discussed (*e.g.* Donelick 1991; Paul and Fitzgerald 1992; Carlson et al. 1999; Donelick et al. 1999; Barbarand et al. 2003). Recent observations by Schouwink et al. (2009) evidenced that irradiations along different crystallographic orientations provoke small but characteristic changes on the elastic behaviour of apatite crystals. Ion-track orientations parallel and perpendicular to the c-axis reveal differences in the anisotropic lattice expansion and tensile-strain distribution around the trajectories, which in turn has significant influence on the axial compressibilities. Moreover, a reduced Grüneisen parameter for the ν_{1b} ($\sim$950 cm^{-1}) compared to that of the ν_1 mode (964 cm^{-1}) indicates compressive strain on the amorphous cores as expected for the reported volume differences. The most im-

portant finding concerns the uniform compression of crystals with tracks aligned parallel to the c-axis, while the elastic behaviour for crystals with tracks parallel to <hk0> directions reveal stronger anisotropy. Nevertheless, the study gives no hint for anisotropy of the formation, which has been reported in previous analytical investigations (*e.g.* Paul and Fitzgerald 1992; Donnelick et al. 1999). Recent molecular dynamics simulations of the track production process could not show distinct effects of orientation (Rabone et al. 2008). While the results obtained in the scope of our study on different fragmentation behaviour even at high-pressure conditions point towards both anisotropy effects for the formation and apparent pressure effects on the orientation-dependent track production in apatite, further efforts are necessary. A more systematic study of the influences of pressure and crystal orientation on track production is currently under progress.

Acknowledgements

We thank Ilona Fin and Oliver Wienand for the careful preparation of the polished crystal sections. Financial support within the BMBF Verbundprojekt (project grant 05KK7VH1) and GSI research grant (project HDGLAS) is acknowledged. Background correction and mathematical fitting of the bands was done with the free software FITYK 0.89 (http://www.unipress.waw.pl/fityk/).

References

Barbarand J, Carter A, Wood I, Hurford T (2003) Compositional and structural control of fission-track annealing in apatite . Chem Geol 198:107-137

Bertel E, Märk TD (1983) Fission Tracks in Minerals: Annealing Kinetics, Track Structure and Age Correction. Phys Chem Miner 9:197-204

Boyer LL, Fleury PA (1974) Determination of interatomic interactions $Ca_{10}(PO_4)_6F_2$ (fluorapatite) from structural and lattice-dynamical data. Phys Rev B 9:2693-2700

Carlson WD, Donelick RA, Ketcham RA (1999) Variability of apatite fission-track annealing kinetics: I Experimental results. Am Miner 84:1213-1223

Comodi P, Liu Y, Frezzotti ML (2001) Structural and vibrational behaviour of fluorapatite with pressure. Part II: in situ micro-Raman spectroscopic investigation. Phys Chem Miner 28:225-231

Crowley KD, Cameron M, Schaefer RL (1990) Annealing of etchable fission-track damage in F-, OH-, Cl- and Sr-apatite: 1. Systematics and preliminary interpretations. Nucl Tracks Rad Meas 17:409-410

Crowley KD, Cameron M, Schaefer RL (1991) Experimental studies of annealing of etched fission tracks in fluorapatite. Geochimica et Cosmochimica Acta 55:1449-1465

Devarajan V, Klee WE (1981) A Potential Model for Fluorapatite. Phys Chem Miner 7:35-42

Donelick RA (1991) Crystallographic orientation dependence of mean etchable fission track length in apatite: An empirical model and experimental observations. Am Mineral 76:83-91

Donelick RA, Ketcham RA, Carlson WD (1999) Variability of apatite fission track annealing kinetics: II Crystallographic orientation effects. Am Mineral 84:1224-1234

Glasmacher UA, Lang M, Keppler H, Langenhorst F, Neumann R, Schardt D, Trautmann C, Wagner GA (2006) Phase Transitions in Solids Stimulated by Simultaneous Exposure to High Pressure and Relativistic Heavy Ions. Phys Rev Let 96:195701

Green PF, Duddy IR, Gleadow AJW, Tingate PR, Laslett GM(1985) Fission-track

annealing in apatite: track length measurements and the form of the Arrhenius plot. Nucl Trac 10:323-328

Green PF, Duddy IR, Gleadow AJW, Tingate PR, Laslett GM (1986) Thermal annealing of fission tracks in apatite: 1. A Qualitative Description. Chem Geol 59:237-253

Jaskierowicz G, Dunlop A, Jonckheere R (2004) Track formation in fluorapatite irradiated with energetic cluster ions. Nucl Instrum Methods Phys Res, Sect B 222:213-227

Konzett J, Frost DJ (2009) The High P-T Stability of Hydroxyl-apatite in Natural and Simplified MORB – an Experimental Study to 15 GPa with Implications for Transport and Storage of Phosphorus and Halogens in Subduction Zones. J Petrol 50:2043-2062

Kravitz LC, Kingsley JD, Elkin EL (1968) Raman and Infrared Studies on Coupled PO_4-Vibrations. J Chem Phys 49:4600-4610

Lang M, Lian J, Zhang F, Hendriks BWH, Trautmann C, Neumann R, Ewing RC (2008a) Fission tracks simulated by swift heavy ions at crustal pressures and temperatures. Earth and Planetary Science Letters, 274:355-358

Lang M, Zhang F, Lian J, Trautmann C, Neumann R, Ewing RC (2008b) Irradiation-induced stabilization of zircon ($ZrSiO_4$) at high pressure. Ear Plan Sci Lett 269:291-295

Lang M, Zhang F, Lian J, Trautmann C, Neumann R, Ewing RC (2009a) Combined high pressure and heavy-ion irradiation a novel approach. J Synch Rad 16:773-777

Lang M, Zhang F, Zhang J, Wang J, Schuster B, Trautmann C, Neumann R, Becker U, Ewing RC (2009b) Nanoscale manipulation of the properties of solids at high pressure with relativistic heavy ions. Nat Mater 8:793-797

Liu J, Glasmacher UA, Lang M, Trautmann C, Voss K-O, Neumann R, Wagner GA, Miletich R (2008) Raman spectroscopy of apatite irradiated with swift heavy ions with and without simultaneous exertion of high pressure. Appl Phys A 91:17-22

Mao H, Xu J, Bell P (1986). Calibration of the ruby gauge to 800 kbar under quasihydrostatic conditions. J Geophys Res 91:4673–4676

Miletich R, Allan D, Kuhs W (2000) High-pressure single-crystal techniques. Rev Mineral Geochem 41:445–519

Miro S, Grebille D, Chateigner D, Pelloquin D, Stoquert J-P, Grob J-J, Costantini J-M, Studer F (2005) X-ray diffraction study of damage induced by swift heavy ion irradiation in fluorapatite. Nucl Instrum Methods Phys Res, Sect B 227:306-318

O'Shea DC, Bartlett ML, Young RA (1974) Compositional analysis of apatites with laser-raman spectroscopy: (OH,F,CL) apatites. Archs Oral Biol 19:995-1006

Paul TA, Fitzgerald PG (1992) Transmission electron microscopic investigation of fission tracks in fluorapatite. Am Miner 77:336-344

Penel G, Leroy G, Rey C, Bres E (1998) MicroRaman Spectral Study of the PO_4 and CO_3 Vibrational Modes in Synthetic and Biological Apatites. Calcif Tissue Int 63:475–481

Rabone JAL, Carter A, Hurford AJ, de Leeuw NH (2008) Modelling the formation of fission tracks in apatite minerals using molecular dynamics simulations. Phys Chem Mineral 35:583-596

Sandhu AS, Singh L, Ramola RC, Singh S, Virk HS (1990) Annealing kinetics of heavy ion radiation damage in crystalline materials. Nucl Instrum Methods Phys Res, Sect B 46:122-124

Schouwink P, Miletich R, Ullrich A, Glasmacher UA, Trautmann C, Neumann R, Kohn BP (2009) Ion tracks in apatite at high pressures. The effect of crystallographic track orientation on the elastic properties of fluorapatite under hydrostatic compression. Phys Chem Mineral, doi:10.1007/s00269-009-0340-0

Schuster B, Lang M, Klein R, Trautmann C, Neumann R, Benyagoub A (2009) Structural phase transition in ZrO_2 induced by swift heavy ion irradiation at high-pressure. Nucl Instrum Methods Phys Res, Sect B 267:964-968

Tisserand R, Rebetez M, Grivet M, Bouffard S, Benyagoub A, Levesque F, Carpena J (2004) Comparative amorphization quantification of two apatitic materials irradiated with heavy ions using XRD and RBS results. Nucl Instrum Methods Phys Res, Sect B 215:129-136

Toulemonde M (1995) Defect Creation by Swift Heavy Ions: Material Modifications in the Electronic Stopping Power Regime. Appl Radiat Isot 46:375-81

Trautmann C, Boccanfuso M, Benyagoub A, Klaumünzer S, Schwartz K, Toule-

monde M (2002) Swelling of insulators induced by swift heavy ions. Nucl Instrum Methods Phys Res, Sect B 191:144-148

Trautmann C, Toulemonde M, Costantini JM, Grob JJ, Schwartz K (2000) Swelling effects in lithium fluoride induced by swift heavy ions. Phys Rev B 62:13-16

Tsuda H, Arends J (1994) Orientational Micro-Raman Spectroscopy on Hydroxyapatite Single Crystals and Human Enamel Crystallites. J Dent Res 73:1703-1710

Villa F, Grivet M, Rebetez M, Dubois C, Chambaudet A, Chevarier N, Martin P, Brossard F, Blondiaux G, Sauvage T, Toulemonde M (1999) Damage morphology of Kr ion tracks in apatite: Dependence on dE/dx. Rad Meas 31:65-70

Villa F, Grivet M, Rebetez M, Dubois C, Chambaudet A, Chevarier N, Blondiaux G, Sauvage T, Toulemonde M (2000) Damage morphology of Kr ion tracks in apatite: Dependence on thermal annealing. Nucl Instrum Methods Phys Res, Sect B 168:72-77

Wagner GA, van den Haute P (1992) Fission track dating. Ferdinand Enke Verlag, Stuttgart

Wang LM, Cameron M, Weber WJ, Crowley KD, Ewing RC (1993) In situ TEM observation of radiation induced amorphization of crystals with apatite structures. Spring Meeting of the Materials Research Society, San Francisco, USA

Weber WJ, Ewing RC, Meldrum A (1997) The kinetics of alpha-decay-induced amorphization in zircon and apatite containing weapons-grade plutonium or other actinides. J Nucl Mater 250:147-155

Weber WJ, Ewing RC, Catlow CRA, Diaz de la Rubia T, Hobbs LW, Kinoshita C, Matzke Hj, Motta AT, Nastasi M, Salje EKH, Vance ER, Zinkle SJ (1998) Radiation effects in crystalline ceramics for the immobilization of high-level nuclear waste and plutonium. Mater Res 13, 6:1434-1484

Weber WJ (2000) Models and mechanisms of irradiation-induced amorphization in ceramics. Nucl Instrum Methods Phys Res, Sect B 98:166-167

Wendt AS, Vidal O, Chadderton LT (2002) Experimental evidence for the pressure dependence of fission track annealing in apatite. Earth and Planetary Science Letters 201:593-607

Williams Q, Knittle E (1996) Infrared and Raman spectra of $Ca_5(PO_4)_3F$-Fluorapatite at high pressures: compression-induced changes in phosphate site and Davydov

splitting. J Phys Chem Solids 57: 417-422

Young EJ, Myers AT, Munson EL, Conklin NM (1969) Mineralogy and geochemistry of fluorapatite from Cerro de Mercado, Durango, Mexico. US Geol Survey Prof Paper 650-D: D84- D93

Zattin M, Bersani D, Carter A (2007) Raman microspectroscopy: A non-destructive tool for routine calibration of apatite crystallographic structure for fission-track analyses. Chem Geol 240:197-204

Ziegler JF, Biersack JP, Littmark U (1985) The Stopping and Range of Ions in Solids. Pergamon, New York

Xie X, Minitti ME, Chen M, Mao H-K, Wang D, Shu J, Fei Y (2003) Tuite, γ-$Ca_3(PO_4)_2$: a new mineral from the Suizhou L6 chondrite. Eur J Miner 15:1001-1005

Sample	Orientation	Thickness / µm	Ion	Energy / MeV/u	dE/dx / keV/nm	penetration depth / µm	Ions/cm^2	Pressure / GPa	Fragmentation
09-H	$(10\bar{1}0)$	5000	^{197}Au	11.1	27	~85	6x10^{11} 1x10^{12}	-	weak strong
09-X	(0001)	5000	^{197}Au	11.1	27	~85	6x10^{11}	-	moderate
21-H	$(10\bar{1}0)$	5000	^{197}Au	11.1	27	~85	6x10^{11} 1x10^{12}	-	weak strong
U-20	$(10\bar{1}0)$	10000	^{180}Ta	11.1	24	~83	1x10^{9}	-	-
U-21	$(10\bar{1}0)$	10000	^{180}Ta	11.1	24	~83	1x10^{10}	-	-
U-22	$(10\bar{1}0)$	10000	^{180}Ta	11.1	24	~83	5x10^{10}	-	-
U-23	$(10\bar{1}0)$	10000	^{180}Ta	11.1	24	~83	1x10^{11}	-	moderate
U-24	$(10\bar{1}0)$	10000	^{180}Ta	11.1	24	~83	1x10^{12}	-	complete
17B-H	$(10\bar{1}0)$	30	^{124}Xe	11.1	18	~73	1x10^{11} 5x10^{11} 1x10^{12} 5x10^{12} 1x10^{13}	-	- weak moderate strong strong
17B-H	$(10\bar{1}0)$ (0001)	30	^{124}Xe	155	18	n.a.	1x10^{11}	3.6	- weak
17B-H	$(10\bar{1}0)$ (0001)	30	^{124}Xe	155	18	n.a.	1x10^{12}	11.5	weak complete
17B-H	$(10\bar{1}0)$ (0001)	30	^{238}U	175	18	n.a.	1x10^{12}	4.91	complete complete

Table 1 Details of irradiation parameters and samples. ***Fragmentation*:** The visible amount of mechanical damage to the sample (***weak:*** few sporadic cracks, ***moderate:*** abundant large cracks, starting to form networks, ***strong:*** extensive cracking throughout the sample, domains of complete fragmentation, ***complete:*** sample completely destroyed and could not be recovered for measurements)

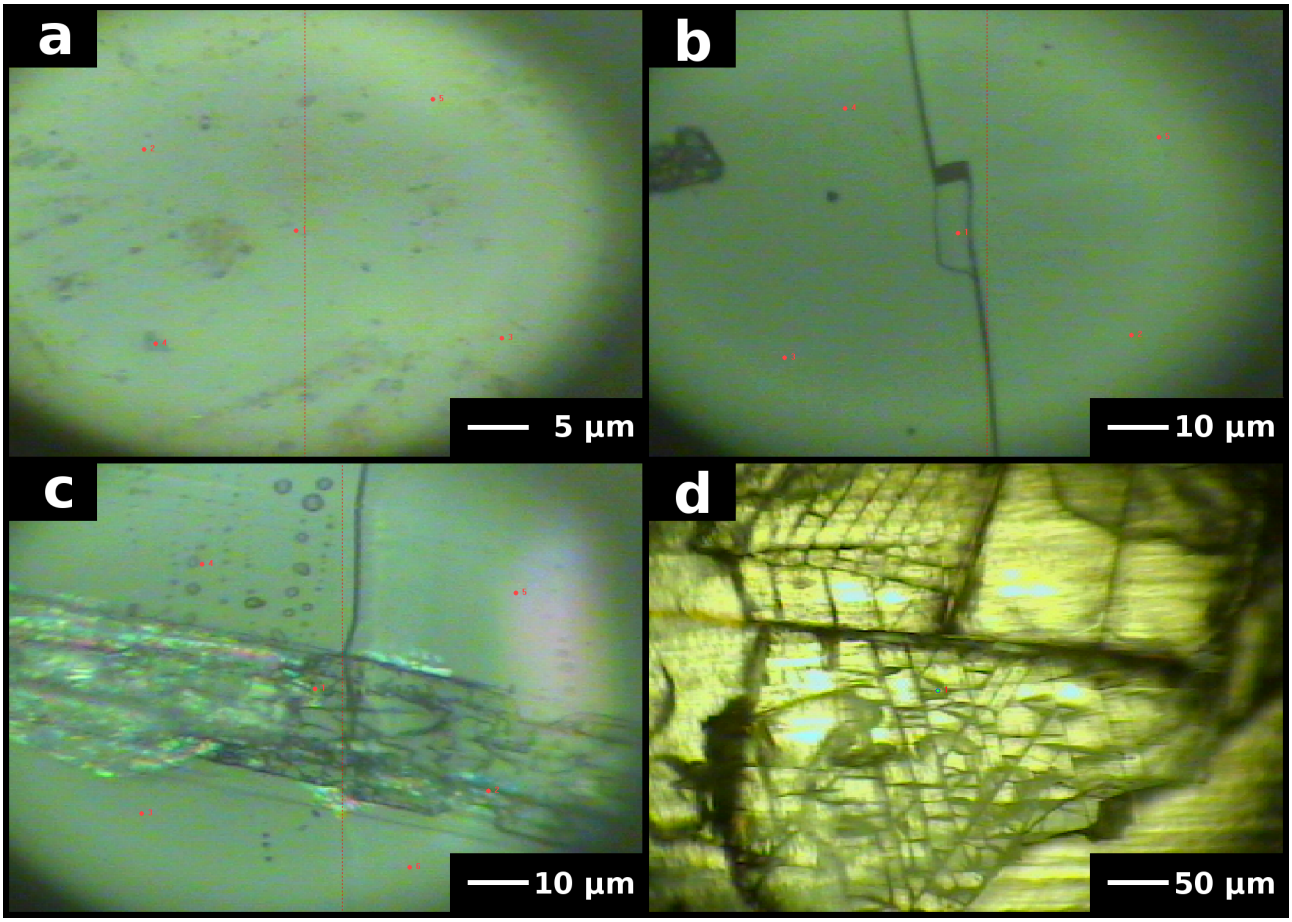

Fig. 1 Examples of different grades of fragmentation: a none (sample 17B-H, 1×10^{11} ions/cm^2), b weak (sample 09-H, 6×10^{11} ions/cm^2), c moderate (sample 09-X, 6×10^{11} ions/cm^2), d strong (sample 17B-H, 5×10^{12} ions/cm^2). Red markers indicate points of Raman measurements

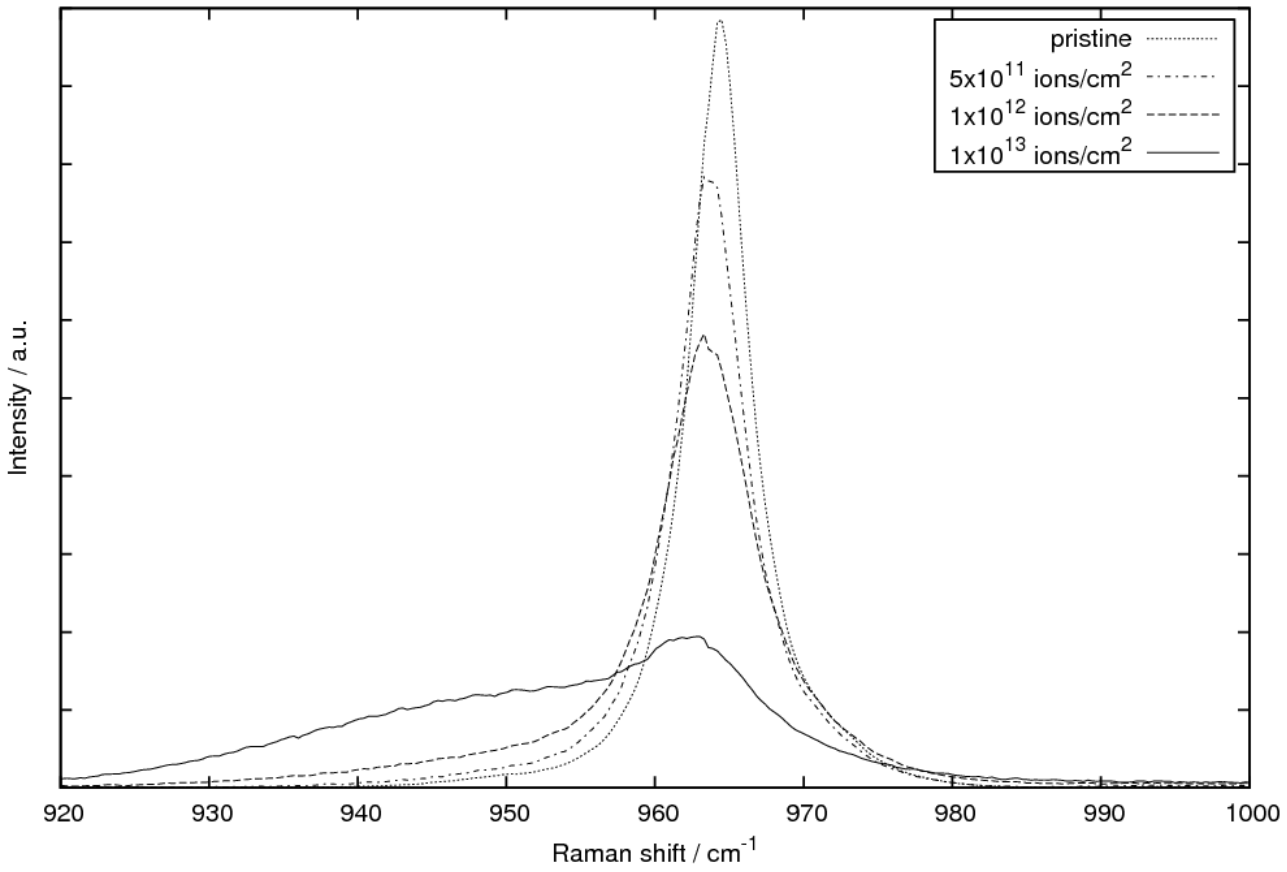

Fig. 2 Raman spectra of the main ν_1 band (964 cm^{-1}) in apatites irradiated with different fluences. Decay of this band and growth of the radiation-induced amorphous broad ν_{1b} band (950 cm^{-1}) can be seen (sample 17B-H, irradiation with Xe, dE/dx ≈18 keV/nm)

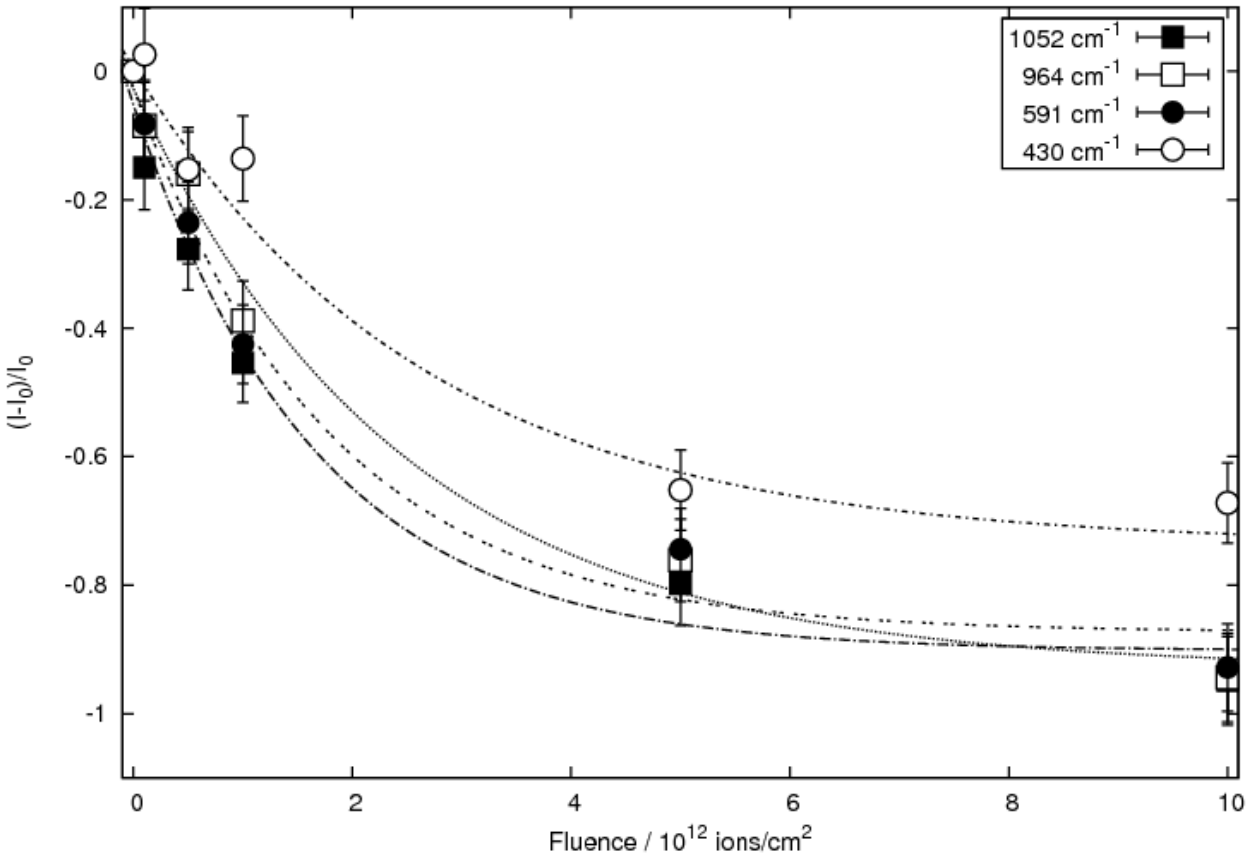

Fig. 3 Decay of band intensities after irradiation for selected apatite Raman bands as a function of fluence (sample 17B-H, irradiation with Xe, dE/dx≈18 keV/nm). Trends are similar for all bands. The lines represent exponential fits to the data

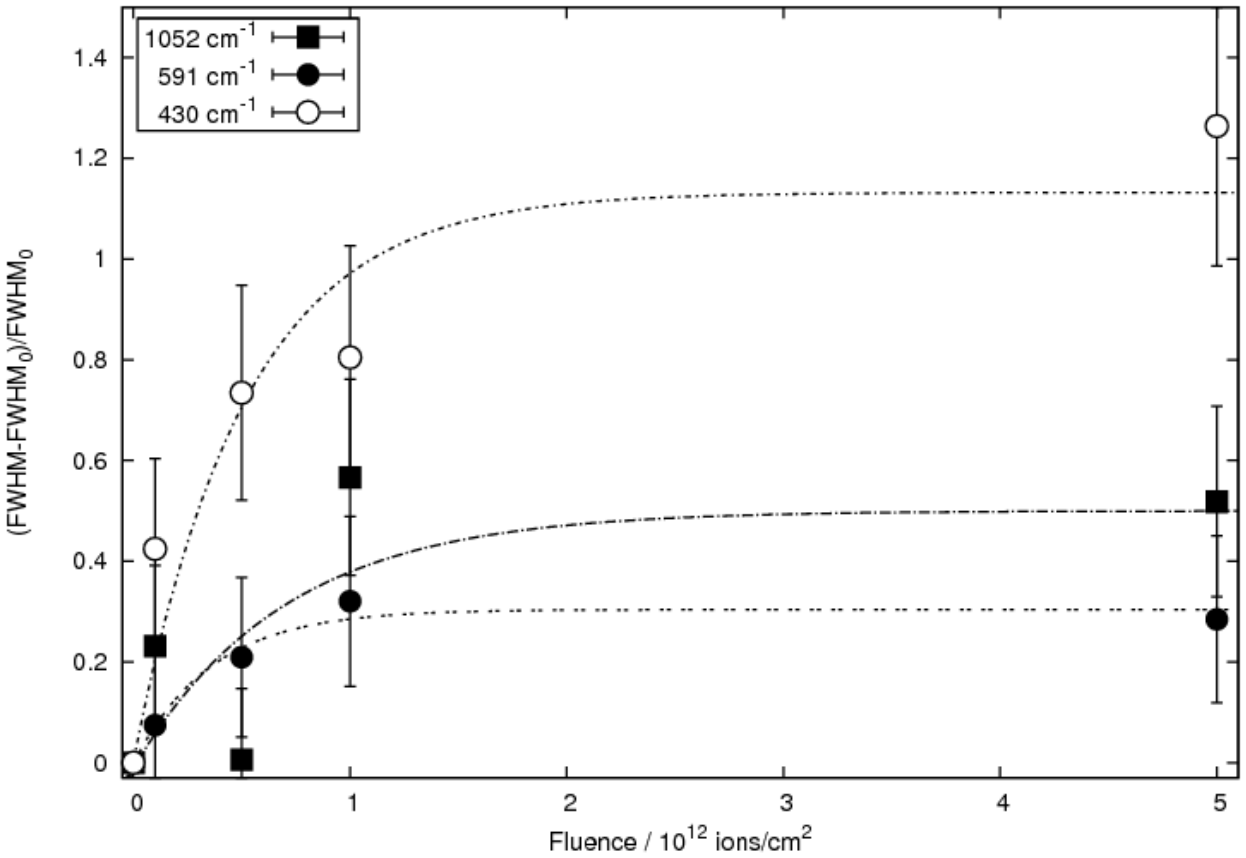

Fig. 4 Increasing FWHMs after irradiation for selected Raman bands as a function of fluence (sample 17B-H, irradiation with Xe, dE/dx≈18 keV/nm). Trends are similar for all bands. The lines represent exponential fits to the data

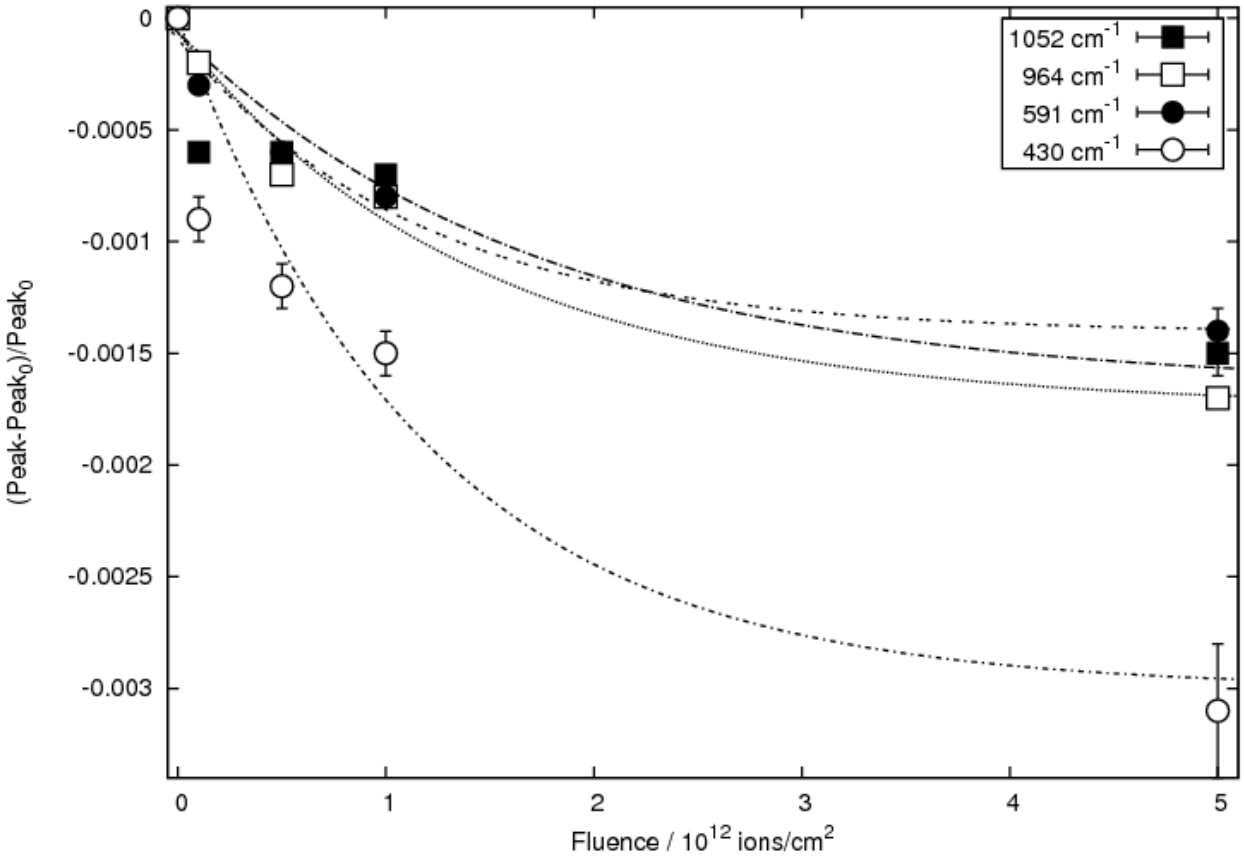

Fig. 5 Change of peak positions after irradiation for selected apatite Raman bands as a function of fluence (sample 17B-H, irradiation with Xe, dE/dx≈18 keV/nm). Trends are similar for all bands. The lines represent exponential fits to the data

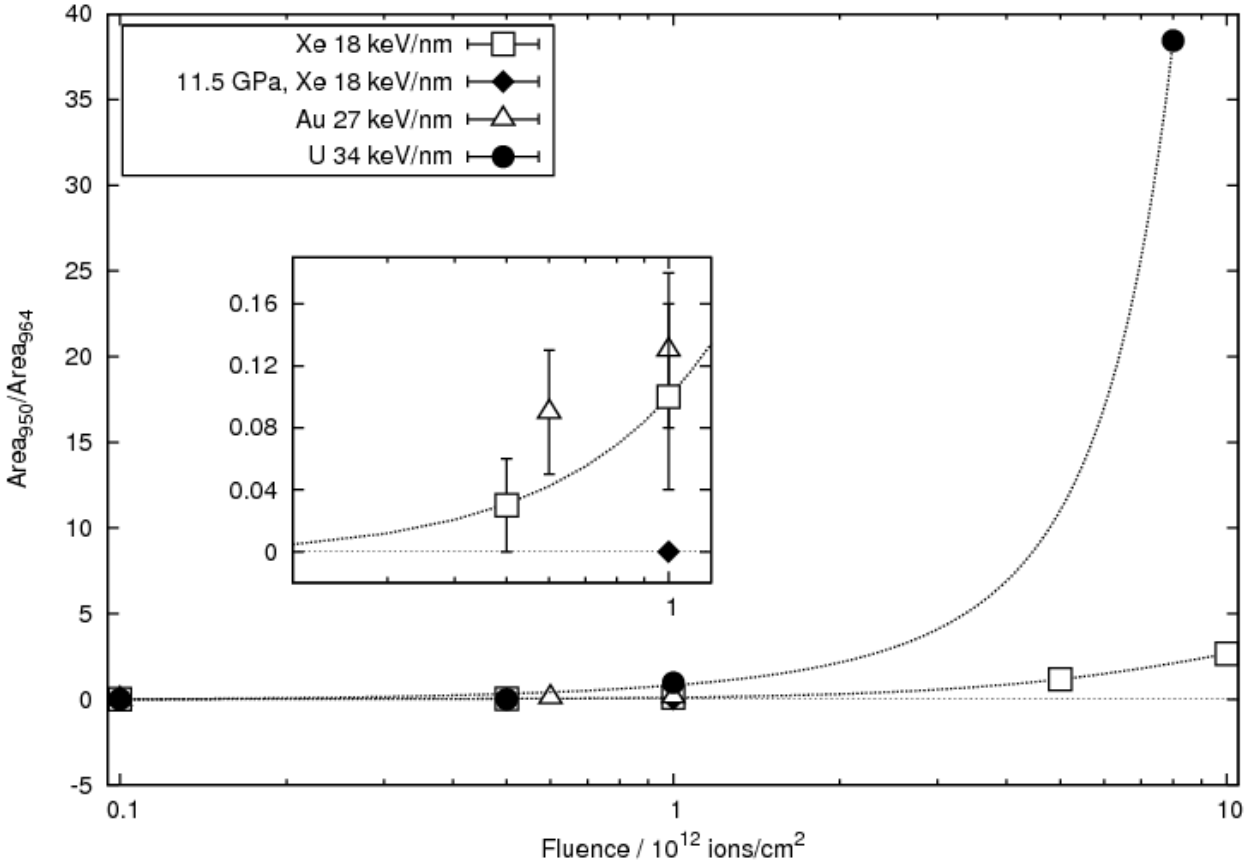

Fig. 6 Area ratio of the radiation-induced broad ν_{1b} band (950 cm^{-1}) to the ν_1 band (964 cm^{-1}) as a function of fluence and energy loss (samples: 17B-H (Xe):, 09-H (Au)). Data of irradiation with U is taken with kind permission from Liu et al. (2008). Some error bars are smaller than the data symbols. Inset: Irradiations under pressure show no sign of the ν_{1b} band up to a fluence of 1×10^{12} ions/cm^2. The lines are visual guides

Appendix E

Publication V - Lattice compression and structural behavior of $NaVSi_2O_6$ clinopyroxene to 11 GPa

A. Ullrich, R. Miletich, F. Nestola, C. Weikusat, H. Ohashi (2009)
American Mineralogist, Vol. 94, pp. 557-564.

Abstract

High-pressure behavior of a synthetic single crystal of the *C2/c* clinopyroxene $NaVSi_2O_6$ was investigated using X-ray diffraction and Raman spectroscopy in combination with diamond-anvil cell techniques. Lattice-parameters, single-crystal intensity data, and Raman spectra were collected up to pressures of about 11 GPa, revealing no discontinuity in the evolution of the lattice with increasing pressure. The fit of a third-order Birch-Murnaghan equation of state to the pressure-volume data yields a bulk modulus of $K_0 = 114.7$ (1.8) GPa with its pressure derivative $K' = 5.4$ (4). Strain analysis reveals compressional anisotropy with unit strain axial ratios of 1:2.9:3.1. The direction of largest compression was found to be perpendicular to the $(\bar{3}02)$ plane, which matches closely the direction of largest interlayer spacing between oxygen monolayers forming the structure of clinopyroxenes. The relatively large pressure dependency of the bulk modulus, compared to that of isostructural transition-metal compounds, was related to an increase in stiffness of the M2 polyhedron occurring above 4.6 GPa.

Introduction

Because pyroxenes are important phases of the Earth's crust and upper mantle, the systematics of their structural behavior under varying pressure, temperature, and/or chemical substitution has been subject of various studies (Yang and Prewitt 2000; Thompson and Downs 2004; Thompson et al. 2005). An important issue is the influence of incorporation of transition metal cations such as Fe^{3+}, Ti^{3+}, Cr^{3+}, and V^{3+} as well as divalent cations (Arlt et al. 1998; Ross and Reynard 1999; Ross and Sowerby 1999; Redhammer et al. 2003).

Common characteristics of all clinopyroxenes (cpx) are the chains of corner-sharing tetrahedra running parallel the crystallographic c axis, and these Si_2O_6 chains are linked laterally via bonding through the M1 and M2 cation sites. Hence the structural stability is determined mainly by the sizes of the M1 and M2 cations, and also the energy contributions from the d-electron configuration, i.e., the influence of crystal-field stabilization energy, which has been shown to be one important parameter that determines the structural stability of cpx (e.g., Arlt et al. 1998). Comparative high-pressure investigations on various $CaM^{2+}Si_2O_6$ and $NaM^{3+}Si_2O_6$ cpx, with and without incorporation of transition-metal cations, excluded a simple linear inverse relationship between bulk modulus, K, and unit-cell volume, as has been found for many isostructural series (Hazen et al. 2000 and references therein). The compression behavior of clinopyroxenes depends to a great extent on the pressure derivative of the bulk modulus -dK/dP, or K', which deviates in many cases significantly from 4. Whereas the bulk modulus seems to depend on the M1 site, K' seems to be mainly controlled by the size of the cation on the M2 site (Nestola et al. 2006). In addition a higher stiffness has been found in cpx with transition metal elements than without these elements (Origlieri et

al. 2003; Zhang et al. 1997; Nestola et al. 2005) evidencing that not only the size of the M1 cation determines the bulk modulus, but also the valence electron character plays an important role for the compression behavior of cpx.

The subject of this study is the transition-metal compound $NaVSi_2O_6$, which is the end-member composition with trivalent vanadium on the M1 site. The crystal structure of the C2/c cpx was first determined by Ohashi et al. (1994), followed by several studies on (Na,Ca)(V,Mg)Si_2O_6 and (Na,Ca)(V,Mn)Si_2O_6 solid solutions (Ohashi et al. 2003a, 2003b) investigating the electronegativity and the 3d-electron distribution. It has been found that because of electron-electron repulsion between the d-electrons and the surrounding O atoms the V^{3+}-ion occupies a small distorted M1 site in the (Na,Ca)(V,Mg)Si_2O_6 system, whereas it can occupy a larger and less distorted site in (Na,Ca)(V,Mn)Si_2O_6. Recent studies on $NaVSi_2O_6$ and other quasi-one-dimensional vanadium-based (S = 1) chain compounds with pyroxene structure have been focused on the low-temperature behavior revealing the formation of a long-range three-dimensional Néel order (Vasiliev et al. 2004; Popović et al. 2006; Pedrini et al. 2007). Hence the question arises whether an analogous transition occurs with increasing pressure.

The present study aims to complement the low-pressure structural data on the end-member $NaVSi_2O_6$ with comparable investigations at high pressure. Apart from the measurements of structural changes for comparative crystal chemistry, high- precision data on lattice compression has been collected in order do determine EOS parameters and the unit-strain ellipsoid. A comparison of the recent data to isostructural C2/c cpx completes the investigation.

Experimental Methods

Sample material and high-pressure conditions

Sample crystals are the same as those used in Ohashi et al. (1994). The crystals were synthesized by a solid-state reaction from a stoichiometric mixture of powder $Na_2Si_2O_5$, V_2O_3, and SiO_2 sealed in a platinum capsule. A belt-type high-pressure apparatus was used to maintain the capsule for 20 h at pressures of 6 GPa and temperatures of 1773 K. All of the crystals are of light green color and crystals of about $150 \times 70 \times 30$ μm in size were chosen for the measurements in diamond-anvil cells (DACs).

All high-pressure investigations were carried out in opposed-anvil DACs, equipped with X-ray transparent beryllium-disk backing plates and a 12° optical port suitable for the spectroscopy applications. Sample crystal was loaded in an ETH-type DAC with standard geometry (height 1.4 mm, table 2.8 mm, girdle 3.0 mm) and culets of 600 μm diameters. Stainless steel gaskets provided the sample chamber of 200-250 μm in diameter with a thickness of about 90 μm. A 4:1 methanol:ethanol mixture was used as pressure-transmitting medium to achieve hydrostatic pressure conditions up to ∼11 GPa. Since X-ray and Raman measurements were carried

out on the same DAC loading, a quartz crystal and a ruby sphere were used as internal pressure markers.

Single-crystal X-ray diffraction

Lattice-parameter measurements at room pressure and 10 high pressures up to 10.70 GPa have been carried out on a Huber four-circle diffractometer using unmonochromatized Mo-radiation. Constrained lattice parameters of $NaVSi_2O_6$ and of the quartz crystal have been refined at each pressure from the positions of 20 Bragg reflections determined by the method of eight-position diffracted-beam centering (King and Finger 1979). By peak profile fitting the lattice parameters were refined with constraint to monoclinic and hexagonal, respectively, using the program SINGLE04 (Ralph and Finger 1982; Angel et al. 2000a). The pressure was monitored from the refined unit-cell volume of quartz, using the equation of state of quartz (Angel et al. 1997). Full intensity data sets were collected on a STOE STADI4 four-circle diffractometer (monochromatized MoK radiation), equipped with an Oxford Diffraction CCD detector, to $2\theta_{max} = 60°$ using an exposure time of 40 s and an ω-scan of 0.2°. The sample-to-detector distance was 60 mm. The CrysAlis RED program (Oxford Diffraction) was used to integrate the intensity data, applying a Lorentz-polarization correction. The absorption correction for the crystal, DAC, and gasket shadowing was performed using the program Absorb 6.0 (Angel 2004). Weighted isotropic structure refinements were done using the SHELX-97 package (Sheldrick 1997), starting from the atomic coordinates of $NaAlSi_2O_6$ cpx (Nestola et al. 2008) with space group C2/c, since no violation of the space group symmetry was detected. Experimental details are given in Table 1.

Raman spectroscopy

Raman spectra between 100 and 1100 cm^{-1} were obtained at five pressures between 1.7 and 9.1 GPa using a LabRam HR800UV spectrometer equipped with an OLYMPUS BXFM-ILHS optical microscope, automated x-y stage, a grating with 1800 grooves per millimeter, a Peltier-cooled CCD detector, and a 100× objective (numerical aperture 0.90). The 632.8 nm line of a He-Ne laser was used as the excitation source. The spectra were recorded in backscattered geometry with a lateral resolution of <1.5 μm, the wavenumber accuracy was 0.5 cm^{-1}, and the spectral resolution was 1 cm^{-1}. Pressures were determined by the ruby fluorescence method (Miletich et al. 2000 and references therein) using the He-Ne laser of the Raman spectrometer. The error in the observed pressure is estimated to be about 0.05 GPa.

Results

Equations of state and strain analysis

Unit-cell data at ambient and high pressures determined in this study and the zero-pressure lattice-parameters determined by Ohashi et al. (1994) are given in Table 2. Although our crystal derives from the same sample material, there are small differences in lattice-parameter values, within about 5 to 6 times the e.s.d. values, that may be explained either from aberrations of the different instruments or material changes occurring during storage over 13 years. Figure 1a displays the change of the unit- cell volume with pressure. Within the e.s.d. values, the data sets collected during compression and decompression are consistent and no discontinuity is apparent, suggesting continuous compression behavior. The fit of a single third-order Birch-Murnaghan equation of state (EOS; EOSFIT, Angel et al. 2000b) to the data set weighted according to the experimental uncertainties yields the parameters V_0 = 427.35 (10) Å^3, K_0 = 114.7 (1.8) GPa, and K' = 5.4 (4).

Regarding the compressibilities of the individual unit-cell axes (Fig. 1b), fits of linearized third-order Birch-Murnaghan EOS to their variations with pressure reveal compressional anisotropy [a_0 = 9.6408 (18) Å, K_0 = 105 (5) GPa with K' = 11.5 (1.6), b_0 = 8.7448 (11) Å, K_0 = 105 (2) GPa with K' = 2.3 (4) and c_0 = 5.2985 (5) Å, K_0 = 107.6 (1.6) GPa with K' = 3.6 (3)]. In particular, the EOS parameters obtained for the crystallographic a axis show large errors indicating an inappropriate use of the EOS-formulation to describe the significant curvature in the pressure-dependent variation of the a axis. The STRAIN software by Ohashi (Hazen and Finger 1982) has been used to determine the major deformation directions. A unit-strain ellipsoid calculated for the compression between 1 bar and 9.54 GPa reveals ratios of 1:2.9:3.1 for the principle axes, with the most compressible direction at an angle of 28.98° from the crystallographic c axis (according to the conventionally symmetry-constrained orienta- tion of the strain ellipsoid).

Structure refinement

The results of structure refinements on the single-crystal intensity data are summarized in Tables 3 and 4. The zero-pressure lattice-parameters differ slightly from the ones determined during the lattice-parameter data collection, which could be due to the use of different sample crystals, although the zero-pressure structure determined in this study is consistent with the one described by Ohashi et al. (1994). According to the site symmetry 2 of the M1 and M2 sites (position 4e), there are three pairs of symmetrically equivalent M-O distances in both the M1 octahedron and the M2 polyhedron. Depending on whether two additional M2-O3 bonds (2.81 Å at 1 bar) are considered, the coordination of the M2 cation is described as 6 or 6+2 fold. The M2 site, which corresponds to the equivalent site of

eightfold-coordinated M2 in other silicate cpx, can be considered highly distorted to accommodate these additional bonds (Fig. 2).

For the $NaVSi_2O_6$ cpx at ambient pressure three pairs of M2-O distances between 2.39 and 2.42 Å and two M2-O bonds at a distance of 2.81 Å (Na-O3c2/d2) suggest a distorted octahedral coordination, which is also supported by bond-valence arguments. The individual M2-O bond lengths decrease continuously with the largest shortening rate observed in M2-O2c2/d2 (Fig. 3a) resulting in a slight increase in BLD from 0.4(2) to 1.3(3)%. The M2-O3c2/d2 bonds, which determine the coordination change from 6 to 6+2, show a linear decrease without any obvious rate changes of bond-length compression.

The M1 site forms a more regular octahedron with three pairs of symmetrically equivalent bonds between 1.947 and 2.070 Å (Fig. 3b). The polyhedral distortion corresponds to a 2 + 4 distortion similar to a typically Jahn-Teller distorted uniaxially compressed octahedron, which is indicative of the distribution of the two d electrons in the non-bonding orbitals of the d^2-configuration of the V^{3+} cations (Ohashi et al. 2003b). Within the experimental errors, all of the bond lengths decrease almost linearly on compression. Accordingly, there is no significant change in BLD parameter observed, implying the continuous regularization of the $M1O_6$ octahedron on increasing pressure, as also expressed by other distortion parameters (Table 4). Almost insignificant changes can be observed for the polyhedral geometry of the SiO_4 group. By comparing the variations in polyhedral volumes (Fig. 3c), the largest compression is found for the M2 polyhedron, revealing a bulk modulus of 53(5) GPa compared to 184(13) and 333(44) GPa determined for the polyhedral compression of the M1 octahedron and the Si tetrahedron, respectively. Whereas all of the polyhedral volumes decrease continuously, the M2 polyhedron reveals an increase in stiffness above 4.6 GPa that coincides with the crossover of the M2-O1a1/b1 and the M2-O2c2/d2 bond lengths. However, as observed for the individual M-O bond lengths, the M1-M2 distance decreases continuously at a rate of 0.9% in the investigated pressure range (Fig. 3d). The geometric mismatch occurring between the M2-polyhedra and the M1-octahedra due to different compressibilities is accommodated by the kinking of the SiO_4 chain (Fig. 4a). The O3-O3-O3 angle is O-rotated, and decreases by 4%. The observed increase in tetrahedral chain kinking is accompanied by a rotation of the SiO_4 tetrahedra around the normal to the tetrahedral basal plane, which is expressed by a 3% decrease in the Si-O3-Si angle (Fig. 4b). The O2 atoms interconnect the chains of tetrahedra and the chains of octahedra along b, and the O1 atoms connect the tetrahedra with the M1 octahedra along a. The increase in kinking and also in the tilt angle of the Si-O chains can be associated with a large decrease in O-O distances shared with the M2 polyhedra.

Raman spectra

Selected Raman spectra are depicted in Figure 5, revealing continuous change during the process of loading pressure. The bands have been assigned according to the spectra of structurally isomorphous $NaTiSi_2O_6$ (Popović et al. 2005; Konstantinović et al. 2004), where 29 of 30 phonon modes expected from factor-group analysis have been recorded. The spectra of $NaTiSi_2O_6$ and $NaVSi_2O_6$ agree to a large extent, although not all of the bands have been found in the latter. This can be ascribed mainly to strong background luminescence that creates a low signal-to-noise ratio and suppresses low intensity peaks. A significant increase in background, especially in the low-frequency region, is observed between 0.49 and 5.34 GPa, which indicates the occurrence of a pressure-induced structural disorder. In the low wavenumber region assigned to complex lattice vibrations due to Si-O bending and M-O interactions, peak ν_{13}, related to (O_1-V-O_1) bending vibrations, seems to split into ν_{13} and ν_{14} with increasing pressure. But considering that the FWHM of ν_{13} is 13.70 cm^{-1} at 0.49 GPa and that the peaks ν_{13} and ν_{14} are expected to be only 5.78 cm^{-1} apart at this pressure, it appears that ν_{13} consists of both peaks, separating with pressure. The wavenumber range between 900 and 1100 cm^{-1} attributed to Si-$O_{1,2}$ and V-$O_{1,2}$ stretching vibrations is dominated by the occurrence of very broad and overlapping peaks thus rendering impossible the unambiguous determination of peak positions. The high wavenumber phonon lines become even broader with increasing pressure, indicating an increase in bond fluctuations in the VO_6 octahedra, whereas no change has been observed in the region of Si-O_3 stretching vibrations between 600 and 900 cm^{-1}. At 11 pressures up to 9.9 GPa, band positions of selected vibrational modes have been obtained from fits of Lorentzian polynomials to the measured data, and their pressure dependent shifts are presented in Figure 6. Apart from the separation of ν_{13} into ν_{13} and ν_{14} all of the peaks shift continuously toward higher wavenumbers with pressure.

Discussion

By comparing the results of this study with existing high-pressure data on cpx, it was found that the high-pressure behavior of $NaVSi_2O_6$ confirms previous observations on cpx compression in general to a large extend. By analogy to studies in other cpx, the value determined for K' deviates significantly from 4 ($K' = 5.4$) confirming that the effect of K' has to be taken into account in the comparison of compressibilities of cpx. Hence the V/V_0 ratio has been calculated from the EOS of various cpx. A comparison of the compressibility of $NaVSi_2O_6$ to other transition-metal containing $NaM^{3+}Si_2O_6$ cpx, has shown a linear dependence between V/V_0 and the ionic radius of the M1 cation (Fig. 7), whereas the EOS determined for $NaAlSi_2O_6$ reveals, as expected, a larger compressibility. Principle axes and the orientation of the unit-strain ellipsoid determined for $NaVSi_2O_6$ are similar to those calculated for diopside, hedenbergite (Zhang et al. 1997), aegirine

(Downs et al. 2006), jadeite (Nestola et al. 2006), and kosmochlor (Origlieri et al. 2003). In all of these C2/c pyroxenes the SiO_4 chain is O-rotated (O3-O3-O3 < 180°) and their compressional anisotropy can be understood by considering these cpx structures as based on cubic closest packing (ccp) of O atoms (Thompson and Downs 2003) with stacking directions perpendicular to (100), $(\bar{1}01)$, (131), and $(1\bar{3}1)$. Room-pressure $NaVSi_2O_6$ reveals an O3-O3-O3 angle of 173.2° at zero pressure, i.e., O-rotated SiO_4 chains show cubic closest packing of O atoms, and the distances between the oxygen monolayers have been determined to be 2.31, 2.56, 2.36, and 2.36 Å, respectively. Hence the highest compression that has been found perpendicular to the $(\bar{3}02)$ plane matches closely with the direction of largest interlayer spacing and approaches it as pressure is increased. Movement of the O atoms toward ideal ccp is indicated by the O3-O3-O3 angle decreasing with a slope of -0.72. This is consistent with the pressure-dependent kinking observed in the SiO_4 chains in kosmochlor, revealing a similar zero pressure O3-O3-O3 angle of 172.8 decreasing with a slope of -0.69. By comparing the zero pressure structure of $NaVSi_2O_6$ to the structure of kosmochlor, not only similar values for the SiO_4 kinking angle have been found, but also the zero pressure tilt angles of the SiO_4 chains are similar. The difference between the ionic radii of V^{3+} (0.64) and Cr^{3+} (0.615) results only in slight differences in the M1 and M2 polyhedral volumes [$V(NaO_6)$ = 11.826 Å^3 and $V(CrO_6)$ = 10.422 Å^3 in kosmochlor], hence also in the polyhedral compressibilities. Whereas the VO_6 octahedron (K_0 = 184 GPa) reveals a significantly larger stiffness than the CrO_6 octahedron (K_0 = 90 GPa), the bulk modulus of the NaO_6 polyhedron reveals larger compressibility for $NaVSi_2O_6$ (K_0 = 53 GPa, as opposed to 70 GPa for kosmochlor). A smaller overall bulk modulus has been found for $NaVSi_2O_6$, compared to K_0 = 134 GPa, which has been determined for kosmochlor. However in addition a significant pressure dependency has been found for the bulk modulus of $NaVSi_2O_6$ ($K' = 5.6$ compared to $K' = 2.0$ determined for kosmochlor). This can be ascribed to the compression behavior of the M2 polyhedron revealing an increase in stiffness above 4.6 GPa.

In conclusion, the cpx $NaVSi_2O_6$ has been found to fit approximately the compression trend observed for other transition-metal- containing cpx, and in addition it reveals a similar orientation of the unit-strain ellipsoid. However, due to an increase in stiffness of the main compressibility-determining structural unit (the M2 polyhedron), the bulk modulus shows a relatively large pressure dependency that has to be taken into account by comparing the compressibility of $NaVSi_2O_6$ to other cpx.

Acknowledgements

This research was supported by the Deutsche Forschungsgemeinschaft (DFG) Grant no. MI 605/2-2. Special thanks are also due to the GSI, Gesellschaft für Schwerionenforschung mbH, Darmstadt (Materials Research Group) for providing the possibility to use the Raman spectrometer.

References cited

Angel, R.J. (2004) Absorption corrections for diamond-anvil cells implemented in the software package Absorb 6.0. Journal of Applied Crystallography, 37, 486-492.

Angel, R.J., Allan, D.R., Miletich, R., and Finger, L.W. (1997) The use of quartz as an internal pressure standard in high-pressure crystallography. Journal of Applied Crystallography, 30, 461-466.

Angel, R.J., Downs, R.T., and Finger, L.W. (2000a) High-temperature–high-pressure diffractometry. In R.M. Hazen and R.T. Downs, Eds., High-Temperature and High-Pressure Crystal Chemistry, 41, p. 559-596. Reviews in Mineralogy and Geochemistry, Mineralogical Society of America and Geochemical Society, Chantilly, Virginia.

— (2000b) Equations of state. In R.M. Hazen and R.T. Downs, Eds., High-Temperature and High-Pressure Crystal Chemistry, 41, p. 35-60. Reviews in Mineralogy and Geochemistry, Mineralogical Society of America and Geochemical Society, Chantilly, Virginia.

Arlt, T., Angel, R.J., Miletich, R., Armbruster, T., and Peters, T. (1998) High-pressure P21/c-C2/c phase transition in clinopyroxenes: Influence of cation size and electronic structure. American Mineralogist, 83, 1176-1181.

Burnham, C.W., Clark, J.R., Papike, J.J., and Prewitt, C.T. (1967) A proposed crystallographic nomenclature for clinopyroxene structures. Zeitschrift für Kristallographie, 125, 109-119.

Downs, R.T. and Singh, A.K. (2006) Analysis of deviatoric stress from nonhy- drostatic pressure on a single crystal in a diamond anvil cell: The case of monoclinic aegirine, $NaFeSi_2O_6$. Journal of Physics and Chemistry of Solids, 67, 1995-2000.

Hazen, R.M. and Finger, L.W. (1982) Comparative Crystal Chemistry, 231 p. Wiley, New York.

Hazen, R.M., Downs, R.T., and Prewitt, C.T. (2000) Principles of comparative crystal chemistry. In R.M. Hazen and R.T. Downs, Eds., High-Temperature and High-Pressure Crystal Chemistry, 41, p. 1-34. Reviews in Mineralogy and Geochemistry, Mineralogical Society of America and Geochemical Society, Chantilly, Virginia.

King, H.E. and Finger, L.W. (1979) Diffracted beam crystal centering and its application to high-pressure crystallography. Journal of Applied Crystallography,

12, 374-378.

Konstantinović, M.J., van den Brink, J., Popović, Z.V., Moshchalkov, V.V., Isobe, M., and Ueda, Y. (2004) Orbital dimerization in $NaTiSi_2O_6$: An orbital analogue of the spin-Peierls phase transition. Physical Review, B69, 020409.

Miletich, R., Allan, D.R., and Kuhs, W.F. (2000) High-pressure single-crystal techniques. In R.M. Hazen and R.T. Downs, Ed., High-Temperature and High-Pressure Crystal Chemistry, 41, p. 445-520. Reviews in Mineralogy and Geochemistry, Mineralogical Society of America and Geochemical Society, Chantilly, Virginia.

Nestola, F., Boffa-Ballaran, T., Tribaudino, M., and Ohashi, H. (2005) Compressional behaviour of $CaNiSi_2O_6$ clinopyroxenes: bulk modulus systematic and cation type in clinopyroxenes. Physics and Chemistry of Minerals, 32, 222-227.

Nestola, F., Boffa-Ballaran, T., Liebske, C., Bruno, M., and Tribaudino, M. (2006) High-pressure behavior along the jadeite $NaAlSi_2O_6$-aegirine $NaFeSi_2O_6$ solid solution up to 10 GPa. Physics and Chemistry of Minerals, 33, 417-425.

Nestola, F., Boffa-Ballaran, T., Liebske, C., Thompson, R., and Downs, R.T. (2008) The effect of the hedenbergitic substitution on the compressibility of jadeite. American Mineralogist, 93, 1005-1013.

Ohashi, H., Osawa, T., and Sato, A. (1994) $NaVSi_2O_6$. Acta Crystallographica, C50, 1652-1655.

— (2003a) Crystal structures of (Na,Ca)(V,Mn)Si_2O_6 pyroxenes. In H. Ohashi, Ed., X-ray study on Si-O bonding, 59 p. Maruzen Publishing Service Center, Tokyo.

— (2003b) Crystal structures of (Na,Ca)(V,Mg)Si_2O_6 pyroxenes. In H. Ohashi, Ed., X-ray Study on Si-O Bonding, 72 p. Maruzen Publishing Service Center, Tokyo.

Origlieri, M.J., Downs, R.T., Thompson, R.M., Pommier, C.J.S., Bonner Denton, M., and Harlow, G.E. (2003) High-pressure crystal structure of kosmochlor, $NaCrSi_2O_6$, and systematics of anisotropic compression in pyroxenes. American Mineralogist, 88, 1025-1032.

Pedrini, B., Gavilano, J.L., Ott, H.R., Kazakov, S.M., and Karpinski, J. (2007) Quenching of the Haladane gap in $LiVSi_2O_6$ and related compounds. The European Physical Journal B: Condensed Matter and Complex Systems, 55, 219-228.

Popović, Z.V., Konstantinović, M.J., Dohević-Mitrović, Z., Isobe, M., and Ueda, Y. (2006) Orbital and lattice dynamics in pyroxenes. Physica B, 378, 1072-1074.

Popović, Z.V., Konstantinović, M.J., Popov, V.N., Cantarero, A., Dohević-Mitrović, Z., Isobe, M., and Ueda, Y. (2005) Optical phonons in the $NaTiSi_2O_6$ oxide with S = 1/2 spin chains. Physical Review B, 71, 224302.

Ralph, R.L. and Finger, L.W. (1982) A computer program for refinement of crystal orientation matrix and lattice constants from diffractometer data with lattice symmetry constraints. Journal of Applied Crystallography, 15, 537-539.

Redhammer, G.J., Ohashi, H., and Roth, G. (2003) Single-crystal structure refinement of $NaTiSi_2O_6$ clinopyroxene at low temperatures ($298 < T < 100$ K). Acta Crystallographica B, 59, 730-746.

Renner, B. and Lehmann, G. (1986) Correlation of angular and bond length distortion in TO_4 units in crystals. Zeitschrift für Kristallographie, 175, 43-59.

Ross, N.L. and Reynard, B. (1999) The effect of iron on the P21/c to C2/c transition in (Mg,Fe)SiO_3 clinopyroxenes. European Journal of Mineralogy, 11, 585-589.

Ross, N.L. and Sowerby, J.R. (1999) High-pressure crystal-field spectra of single-crystal clinoferrosilite. European Journal of Mineralogy, 11, 791-801.

Sheldrick, G.M. (1997) SHELX, programs for Crystal Structure Analysis. University of Göttingen, Germany.

Thompson, R.M. and Downs, R.T. (2003) Model pyroxenes I: Ideal pyroxene topologies. American Mineralogist, 88, 653-666.

— (2004) Model pyroxenes II: Structural variations as a function of tetrahedral rotation. American Mineralogist, 89, 614-628.

Thompson, R.M., Downs, R.T., and Redhammer, G.J. (2005) Model pyroxenes III: Volume of C2/c pyroxenes at mantle P, T and x. American Mineralogist, 90, 1840-1851.

Vasiliev, A.N., Ignatchik, O.L., Isobe, M., and Ueda, Y. (2004) Long range Néel order in quasi-one-dimensional vanadium-based (S=1) pyroxenes (Li, Na) V(Si,Ge)$_2O_6$. Physical Review, B70, 132415.

Yang, H. and Prewitt, C.T. (2000) Chain and layer silicates at high tempera-

tures and pressures. In R.M. Hazen and R.T. Downs, Ed., High-Temperature and High-Pressure Crystal Chemistry, 41, 211 p. Reviews in Mineralogy and Geochemistry, Mineralogical Society of America and Geochemical Society, Chantilly, Virginia.

Zhang, L., Ahsbahs, H., Hafner, S.S., and Kutoglu, A. (1997) Single-crystal compression and crystal-structure of clinopyroxene up to 10 GPa. American Mineralogist, 82, 245-258.

Pressure (GPa)	0.0001	1.52	3.47	7.18	9.39	10.93	7.62	4.61	6.10
a (Å)	9.644(6)	9.614(8)	9.566(9)	9.496(10)	9.469(9)	9.453(9)	9.483(9)	9.545(8)	9.519(8)
b (Å)	8.749(6)	8.706(8)	8.659(8)	8.568(9)	8.521(8)	8.490(8)	8.565(8)	8.634(7)	8.598(7)
c (Å)	5.304(2)	5.278(4)	5.252(4)	5.201(4)	5.169(5)	5.150(5)	5.193(5)	5.233(4)	5.208(5)
β (°)	106.96(5)	106.86(5)	106.82(8)	106.25(8)	105.99(8)	105.89(8)	106.13(11)	106.59(9)	106.31(11)
V (Å^3)	428.06 4	422.78 4	416.42 4	406.26 4	400.93 4	397.52 4	405.18 4	413.31 4	409.09 4
Z	4	4	4	4	4	4	4	4	4
No. measured reflections	244	247	237	235	225	224	228	231	228
Unique reflections ($\|F_o\| > 4\theta$)	198	177	174	171	168	163	163	171	161
R_{int}	0.0271	0.0637	0.0524	0.0514	0.0487	0.0462	0.0458	0.0541	0.0529
Max. 2θ(°)	58.35	58.68	58.74	59.24	58.86	59.09	58.58	59.29	59.66
Range of *hkl*	$-10 < h < 9$ $0 < k < 9$ $0 < l < 7$	$-10 < h < 9$ $0 < k < 9$ $0 < l < 7$	$-10 < h < 9$ $0 < k < 9$ $0 < l < 7$	$-10 < h < 9$ $0 < k < 9$ $0 < l < 7$	$-10 < h < 9$ $0 < k < 9$ $0 < l < 7$	$-10 < h < 9$ $0 < k < 9$ $0 < l < 7$	$-10 < h < 9$ $0 < k < 9$ $0 < l < 7$	$-10 < h < 9$ $0 < k < 9$ $0 < l < 7$	$-10 < h < 9$ $0 < k < 9$ $0 < l < 7$
Refinement									
$R1(\|F_o\| > 4\sigma)$	0.0428	0.0465	0.0459	0.0437	0.0443	0.0439	0.0427	0.0421	0.0433
*wR*2	0.0983	0.1257	0.1308	0.1074	0.0971	0.1100	0.0970	0.0970	0.1092
GooF	1.107	1.017	1.052	1.038	1.025	1.066	1.020	1.089	1.069
Parameters refined	30	22	22	22	22	22	22	22	22

Note: Data listed in order of collection, reliability factors have been determined according to: $R_{int} = \Sigma|F_o^2 - F_o^2(\text{mean})|/\Sigma[F_o^2]$, $R1 = \Sigma||F_o| - |F_c||/\Sigma|F_o|$, $wR2 = \{\Sigma[w(F_o^2 - F_c^2)^2]/\Sigma[w(F_o^2)^2]\}^{1/2}$, and $\text{GooF} = \{\Sigma[w(F_o^2 - F_c^2)^2]/(n-p)\}^{1/2}$, where n = number of reflections and p = total number of parameters refined.

Table 1 Experimental details of the intensity-data collection and the structure refinement of $NaVSi_2O_6$

P (GPa)	V_{Qtz} (Å^3)	a (Å)	b (Å)	c (Å)	β (°)	V (Å^3)
0.0001*	112.994(10)	9.6339(4)*	8.7413(2)*	5.2960(3)*	106.905(2)*	426.72(3)*
0.0001	109.268(8)	9.6385(8)	8.7443(7)	5.2976(8)	106.915(9)	427.17(8)
1.376(3)	107.079(8)	9.6019(3)	8.7073(5)	5.2764(3)	106.747(4)	422.43(4)
2.343(4)	106.052(6)	9.5777(4)	8.6823(6)	5.2616(4)	106.634(4)	419.22(4)
2.844(3)	101.211(7)	9.5645(3)	8.6689(4)	5.2545(3)	106.578(3)	417.55(3)
5.674(5)	102.200(6)	9.5037(4)	8.5983(5)	5.2138(4)	106.231(4)	409.07(4)
5.026(4)	102.479(7)	9.5155(5)	8.6119(7)	5.2223(4)	106.307(4)	410.73(4)
4.850(4)	98.535(5)	9.5206(5)	8.6154(7)	5.2245(4)	106.331(4)	411.25(4)
7.636(4)	95.077(8)	9.4685(5)	8.5499(7)	5.1879(5)	106.016(5)	403.68(5)
10.696(8)	96.294(19)	9.431(3)	8.469(4)	5.1492(14)	105.663(18)	396.01(14)
9.544(17)	97.151(8)	9.446(3)	8.500(4)	5.1637(14)	105.812(17)	398.89(16)
8.783(7)		9.4477(7)	8.5243(3)	5.1732(3)	105.882(5)	400.72(4)

* Data collected by Ohashi et al. (1994).

Table 2 Unit-cell parameters of $NaVSi_2O_6$ as a function of pressure

	Multiplicity Wykoff letter Site symmetry	Parameter	0.0001 GPa	1.52 GPa	3.47 GPa	7.18 GPa	9.39 GPa	10.93 GPa	7.62 GPa	4.61 GPa	6.10 GPa
Na	4*e* 2	*y*	0.3017(5)	0.3021(6)	0.3049(6)	0.3064(6)	0.3081(6)	0.3097(7)	0.3068(6)	0.3049(7)	0.3055(7)
		U	0.0147(16)	0.0165(12)	0.0151(13)	0.0134(11)	0.0134(11)	0.0121(12)	0.0145(11)	0.0158(11)	0.0142(12)
V	4*e* 2	*y*	0.9050(2)	0.9056(2)	0.9059(3)	0.9068(3)	0.9078(3)	0.9076(3)	0.9072(3)	0.9062(3)	0.9067(3)
		U	0.0062(6)	0.0078(6)	0.0072(7)	0.0074(6)	0.0062(6)	0.0059(6)	0.0069(6)	0.0069(6)	0.0061(6)
Si	8*f* 1	*x*	0.2913(2)	0.2918(3)	0.2921(3)	0.2922(3)	0.2921(3)	0.2920(3)	0.2921(3)	0.2918(3)	0.2920(3)
		y	0.0909(3)	0.0916(3)	0.0918(3)	0.0930(3)	0.0934(3)	0.0937(3)	0.0928(3)	0.0926(3)	0.0923(3)
		z	0.2390(3)	0.2393(4)	0.2397(5)	0.2401(4)	0.2399(4)	0.2400(4)	0.2399(4)	0.2398(4)	0.2400(4)
		U	0.0076(6)	0.0076(6)	0.0076(7)	0.0067(6)	0.0062(6)	0.0067(6)	0.0069(5)	0.0065(6)	0.0061(6)
O1	8*f* 1	*x*	0.1159(6)	0.1153(7)	0.1143(8)	0.1157(6)	0.1150(6)	0.1153(6)	0.1154(6)	0.1148(6)	0.1148(6)
		y	0.0790(6)	0.0802(6)	0.0823(7)	0.0831(7)	0.0845(7)	0.0844(7)	0.0829(7)	0.0809(7)	0.0817(7)
		z	0.1446(8)	0.1439(10)	0.1451(11)	0.1455(9)	0.1457(9)	0.1459(9)	0.1457(9)	0.1448(8)	0.1453(9)
		U	0.0080(10)	0.0066(12)	0.0076(13)	0.0061(12)	0.0055(11)	0.0043(12)	0.0062(11)	0.0045(11)	0.0052(12)
O2	8*f* 1	*x*	0.3605(7)	0.3602(8)	0.3605(9)	0.3596(8)	0.3601(8)	0.3605(8)	0.3615(7)	0.3613(7)	0.3610(8)
		y	0.2577(6)	0.2574(7)	0.2590)7)	0.2605(7)	0.2612(7)	0.2607(8)	0.2594(7)	0.2581(7)	0.2582(7)
		z	0.3058(9)	0.3098(11)	0.3123(12)	0.3183(11)	0.3220(11)	0.3238(11)	0.3200(10)	0.3153(10)	0.3170(11)
		U	0.0113(12)	0.0110(14)	0.0110(15)	0.0102(13)	0.0092(13)	0.0096(15)	0.0087(13)	0.0077(13)	0.0077(14)
O3	8*f* 1	*x*	0.3519(7)	0.3525(7)	0.3528(8)	0.3553(7)	0.3550(7)	0.3563(8)	0.3558(8)	0.3543(8)	0.3550(8)
		y	0.0090(6)	0.0113(7)	0.0133(8)	0.0168(7)	0.0188(7)	0.0193(8)	0.0176(7)	0.0137(7)	0.0155(7)
		z	0.0135(9)	0.0101(10)	0.0091(12)	0.0044(10)	0.0021(10)	0.0005(11)	0.0037(10)	0.0076(10)	0.0047(10)
		U	0.0097(11)	0.089(12)	0.0101(14)	0.0090(12)	0.0083(12)	0.0082(12)	0.0095(11)	0.0098(12)	0.0086(12)

Table 3 Pressure-dependent variation of atom positions and atomic displacement factors determined for $NaVSi_2O_6$

	0.000 GPa	1.52 GPa	3.47 GPa	7.18 GPa	9.39 GPa	10.93 GPa	7.62 GPa	4.61 GPa	6.1 GPa
					M2 (Na)				
M2-O1a1,b1	2.392(6)	2.373(7)	2.359(8)	2.344(7)	2.320(7)	2.336(8)	2.345(7)	2.346(6)	2.351(8)
M2-O2c2,d2	2.405(6)	2.379(7)	2.366(7)	2.339(7)	2.330(7)	2.309(7)	2.324(7)	2.364(7)	2.337(7)
M2-O3c1,d1	2.420(6)	2.427(7)	2.410(8)	2.406(7)	2.405(8)	2.389(8)	2.407(8)	2.405(8)	2.410(8)
M2-O3c2,d2	2.811(6)	2.769(6)	2.724(7)	2.637(6)	2.598(6)	2.565(7)	2.621(6)	2.697(7)	2.658(7)
$<M2\text{-}O>_6$	2.406(3)	2.393(4)	2.388(5)	2.373(4)	2.352(4)	2.344(4)	2.359(4)	2.372(4)	2.366(4)
$V(M2)_6$	12.15(4)	11.71(5)	11.37(5)	10.86(5)	10.65(5)	10.55(5)	10.78(5)	10.98(5)	10.87(5)
$BLD\ (\%)_6$	0.4(2)	0.9(2)	1.0(3)	1.3(2)	1.5(2)	1.3(3)	1.4(3)	0.9(2)	1.2(3)
$<M2\text{-}O>_8$	2.507(3)	2.487(3)	2.500(4)	2.432(3)	2.413(3)	2.400(4)	2.424(4)	2.453(3)	2.439(4)
$V(M2)_8$	26.05(11)	25.49(13)	24.91(14)	24.02(12)	23.54(12)	23.16(13)	23.76(12)	24.52(13)	24.14(13)
$BLD\ (\%)_8$	6.07(17)	5.67(19)	5.9(2)	4.7(2)	3.8(2)	3.4(2)	4.1(2)	5.0(2)	4.5(2)
					M1 (V)				
M1-O2c1,d1	1.947(6)	1.954(7)	1.939(7)	1.934(6)	1.930(6)	1.927(6)	1.930(6)	1.940(6)	1.939(6)
M1-O1a2b2	2.060(5)	2.052(6)	2.045(7)	2.029(6)	2.017(6)	2.012(6)	2.021(6)	2.031(6)	2.023(6)
M1-O1a1b1	2.070(5)	2.057(6)	2.049(6)	2.045(5)	2.036(5)	2.033(6)	2.044(5)	2.047(5)	2.044(6)
<M1-O>	2.026(3)	2.021(3)	2.011(4)	2.003(3)	1.994(3)	1.991(3)	1.998(3)	2.006(3)	2.002(3)
<M1-O1>	2.065(3)	2.054(4)	2.047(5)	2.037(4)	2.026(4)	2.022(4)	2.033(4)	2.039(4)	2.034(4)
V_{M1}	10.96(2)	10.88(5)	10.72(5)	10.59(4)	10.46(4)	10.41(5)	10.54(4)	10.64(4)	10.59(5)
BLD (%)	2.6(2)	2.2(2)	2.4(3)	2.3(2)	2.2(3)	2.1(3)	2.3(2)	2.2(2)	2.1(2)
OAV $(°)^2$	26.1(7)	25.2(9)	25.9(1.0)	23.8(9)	23.3(9)	22.4(9)	21.5(8)	23.9(8)	22.9(9)
<O-O>	2.861(2)	2.855(2)	2.840(2)	2.829(2)	2.817(2)	2.812(2)	2.823(2)	2.833(2)	2.828(2)
ELD (%)	2.98(10)	2.93(11)	2.89(12)	2.89(11)	2.82(11)	2.81(11)	2.75(10)	2.93(11)	2.89(11)
$<O\text{-}O>_{shared}$	2.817(3)	2.800(4)	2.776(4)	2.773(4)	2.756(4)	2.753(4)	2.764(3)	2.771(4)	2.768(4)
$<O\text{-}O>_{unshared}$	2.893(3)	2.893(3)	2.886(3)	2.868(3)	2.861(3)	2.855(3)	2.865(3)	2.877(3)	2.871(3)
e_u/e_s	1.0272(14)	1.0332(17)	1.0397(19)	1.0342(17)	1.0381(17)	1.0371(18)	1.0365(15)	1.0380(16)	1.0374(17)
					Si				
Si-O2	1.601(6)	1.585(6)	1.589(7)	1.578(7)	1.578(7)	1.569(7)	1.578(6)	1.578(7)	1.575(7)
Si-O1	1.622(6)	1.627(7)	1.630(8)	1.612(7)	1.615(6)	1.609(7)	1.612(6)	1.623(6)	1.621(7)
Si-O3	1.641(5)	1.644(6)	1.635(7)	1.635(6)	1.631(6)	1.626(7)	1.636(6)	1.638(6)	1.630(7)
Si-O3	1.652(5)	1.644(6)	1.640(7)	1.642(5)	1.635(5)	1.643(6)	1.642(5)	1.646(5)	1.646(6)
<Si-O>	1.629(3)	1.625(3)	1.624(4)	1.617(3)	1.615(3)	1.612(3)	1.617(3)	1.621(3)	1.618(3)
$d_{br\text{-}nbr}$	0.035(5)	0.038(6)	0.028(7)	0.043(6)	0.037(6)	0.046(7)	0.044(6)	0.041(6)	0.040(7)
$V_{tetrahedron}$	2.205(7)	2.190(8)	2.187(9)	2.159(8)	2.150(8)	2.136(8)	2.158(8)	2.174(8)	2.161(9)
BLD (%)	1.1(3)	1.2(3)	1.1(3)	1.3(3)	1.1(3)	1.4(3)	1.4(3)	1.3(3)	1.3(3)
TAV $(°)^2$	16.5(1.0)	15.8(1.2)	12.6(1.2)	13.4(1.0)	13.5(1.0)	16.1(1.2)	16.2(1.1)	17.9(1.2)	16.2(1.2)
O1-Si-O2	117.2(3)	116.9(3)	116.1(4)	116.0(3)	115.9(3)	116.3(4)	116.8(3)	117.3(3)	116.9(3)
Si-O3-Si	139.8(3)	139.5(5)	139.2(5)	137.1(5)	136.7(5)	135.6(5)	136.5(5)	138.0(5)	137.2(5)
O3-O3-O3	173.2(4)	171.5(5)	170.0(6)	167.4(5)	165.9(5)	165.5(6)	166.8(5)	169.7(5)	168.3(5)
M1-O1-M1	98.5(2)	98.3(3)	98.0(3)	97.0(2)	96.6(2)	96.4(3)	97.0(2)	98.0(2)	97.5(3)
M1-M2	3.210(3)	3.199(4)	3.198(4)	3.178(4)	3.172(4)	3.168(4)	3.178(4)	3.189(4)	3.180(4)
M1-M1	3.130(3)	3.109(3)	3.091(3)	3.052(3)	3.025(3)	3.015(3)	3.044(3)	3.077(3)	3.059(3)

Table 4 Selected bond lengths (Å), polyhedral volumes ($Å^3$), angles (°), and distortion parameters (Renner and Lehmann 1986) determined at different pressures

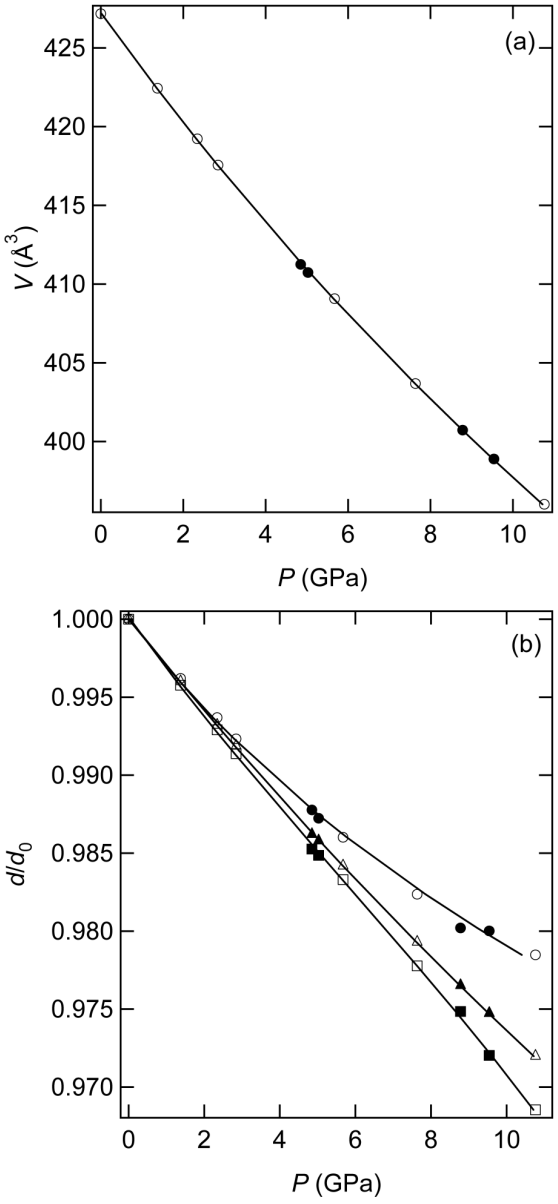

Figure 1 Compression behavior of the unit cell (open symbols show the data collected during compression, solid symbols the data collected during decompression, e.s.d. values are smaller than symbols). (**a**) Change of the unit-cell volume with pressure (the solid line represents the t of a third-order Birch Murnaghan EOS to the measured data using the EOS parameters given in the text). (**b**) Change of the lattice parameters with pressure (a/a_0, b/b_0, and c/c_0 are represented by circles, squares, and triangles, respectively).

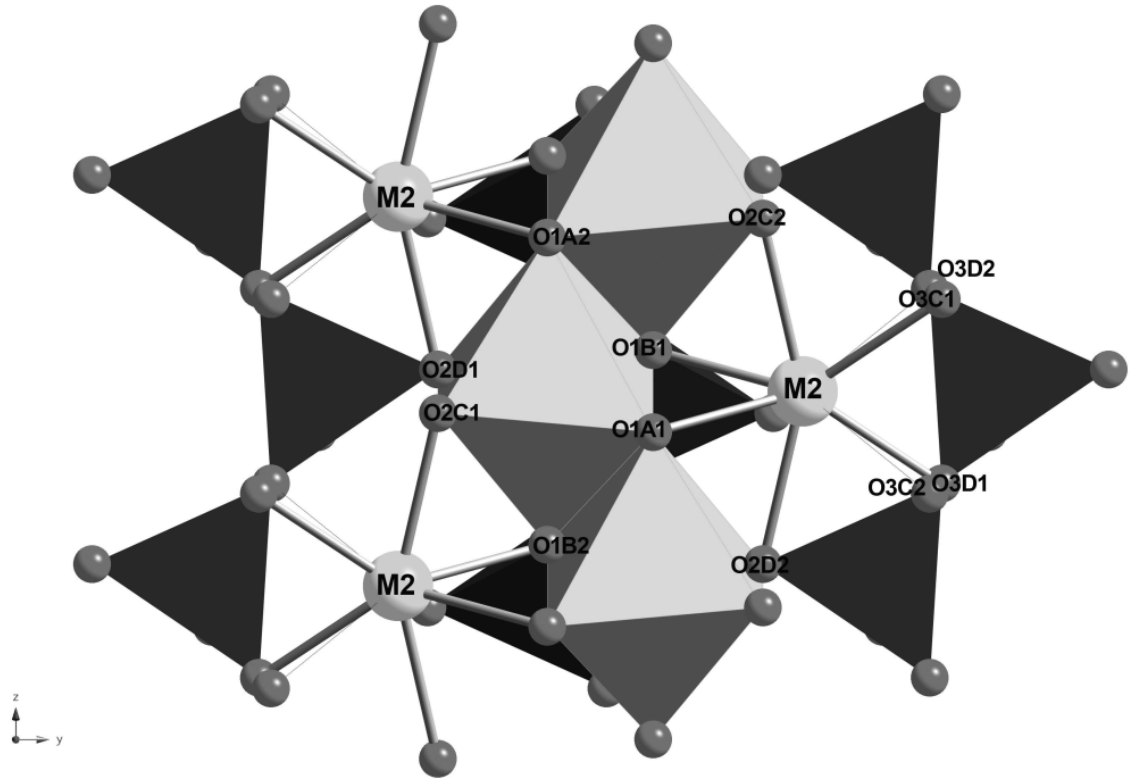

Figure 2 The structure of $NaVSi_2O_6$ viewed down the crystallographic *a*-axis. The SiO_4-tetrahedra and the VO_6-octahedra are shown as polyhedra. The O atoms are labeled after Burnham et al. (1967).

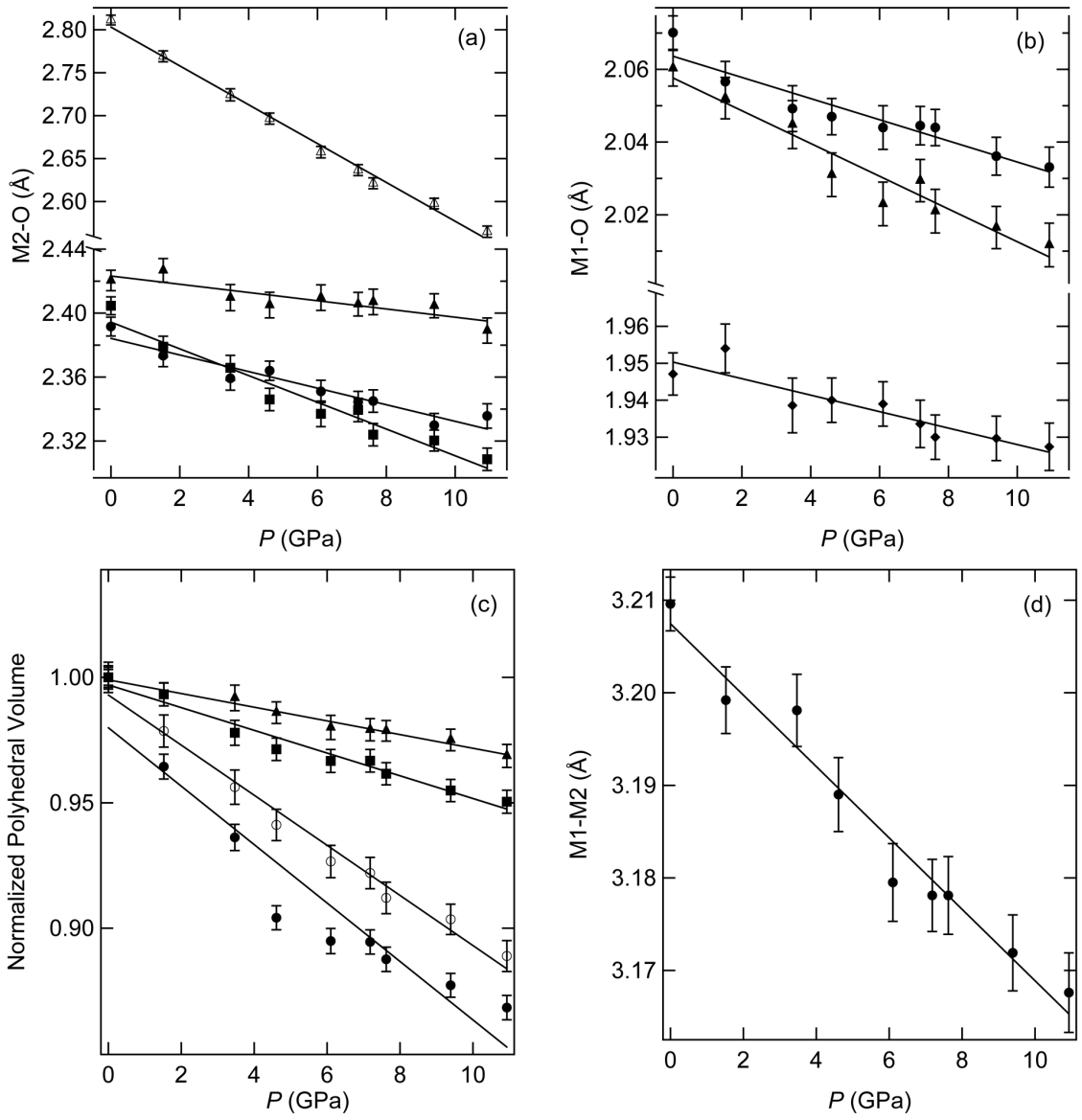

Figure 3 Variation in bond lengths, polyhedral volumes, and M1-M2 distances with pressure: lines represent linear ts to the data. (**a**) Pressure-dependent change of the individual Na-O bond lengths (M2-O1a1/b1 bonds are represented by circles, M2-O2c2/d2 by squares, M2-O3c1/d1 by solid triangles, and M2-O3c2/d2 by open triangles). (**b**) Variation of V-O distances (M1-O1a1/b1, M1-O1a2b2, and M1-O2c1/d1 bond lengths are shown by circles, squares, and triangles). (**c**) Normalized polyhedral volumes of NaO_6 (closed circles), NaO_8 (open circles), VO_6 (squares), and SiO_4 (triangles). Bulk moduli determined from linear ts to the measured data are given in the text. (**d**) Interatomic distance between M1 and M2 cations.

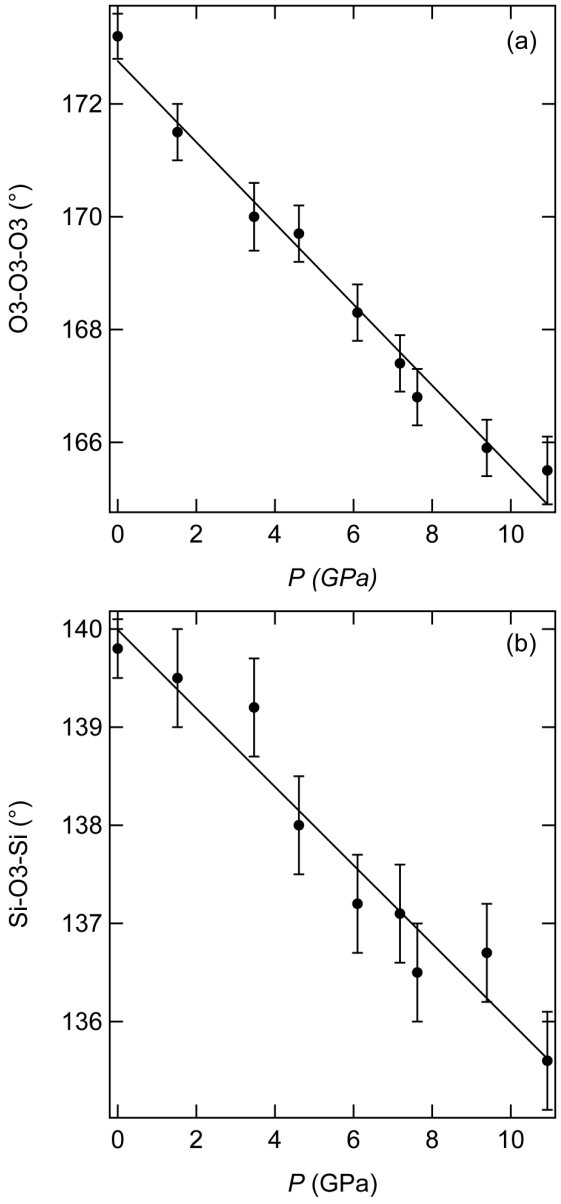

Figure 4 Changes in tetrahedral chain geometry with pressure. (**a**) Increase in tetrahedral chain kinking. (**b**) Rotation of the SiO_4 tetrahedra around the normal to the tetrahedral basal plane.

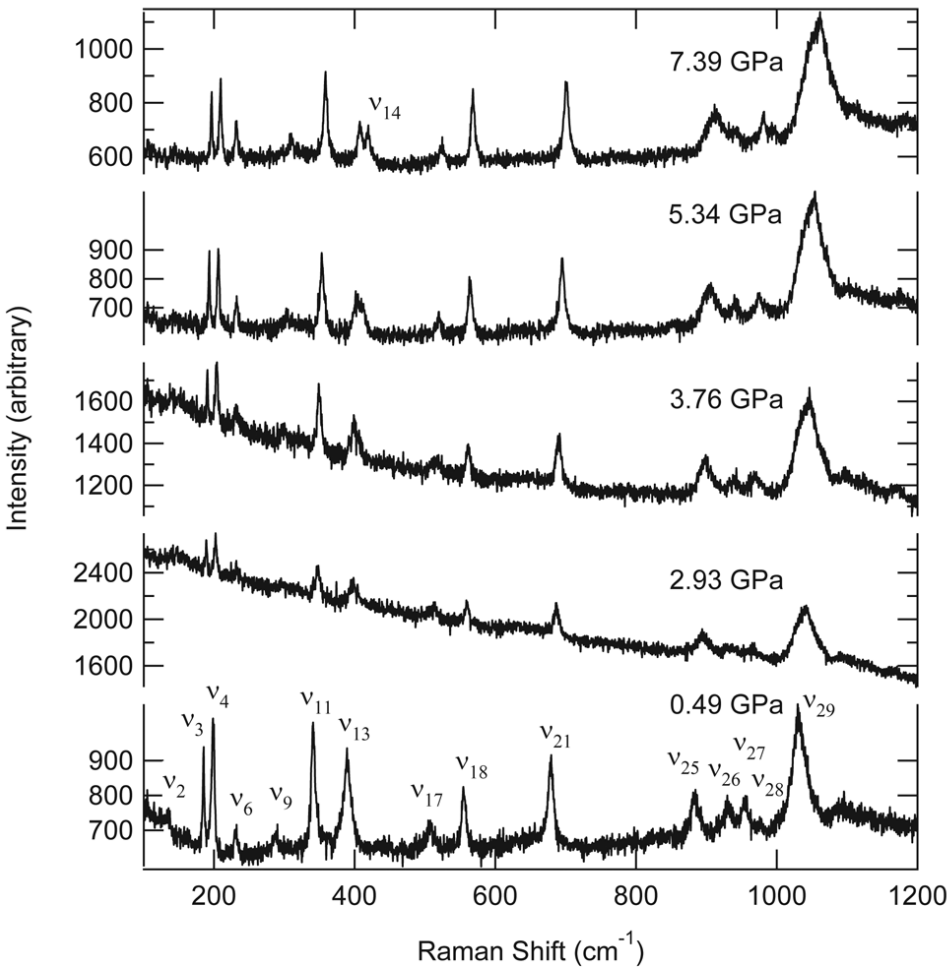

Figure 5 Selected Raman spectra of $NaVSi_2O_6$ varying with pressure; peaks have been labeled according to the isostructural $NaTiSi_2O_6$ cpx (Popović et al. 2005; Konstantinović et al 2004).

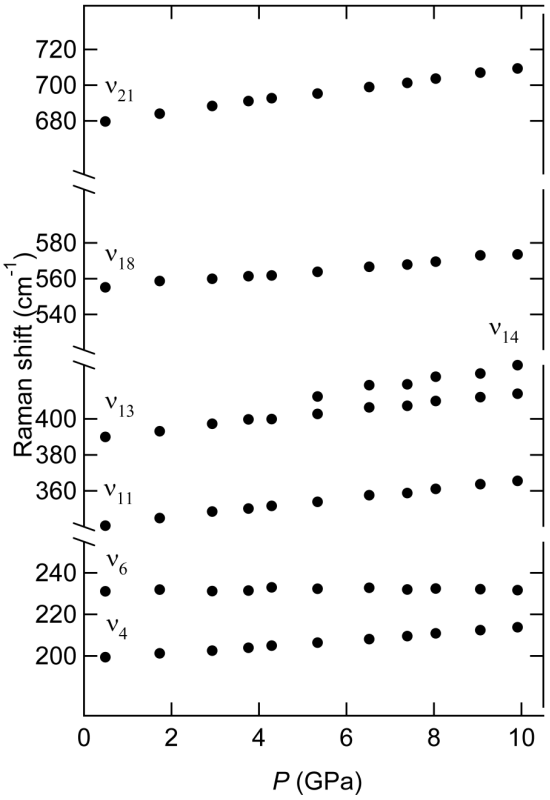

Figure 6 Continuous change of selected vibrational modes with pressure.

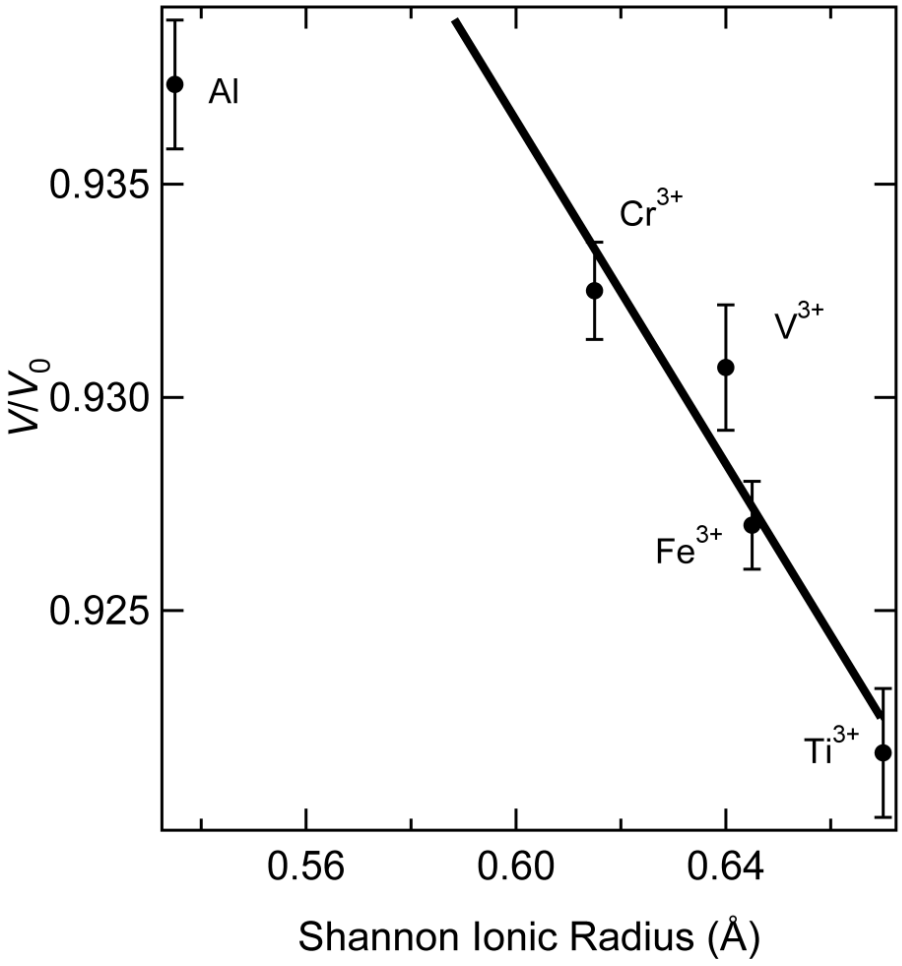

Figure 7 V/V_0 ratio at 10 GPa calculated from the Birch-Murnaghan EOS of various $NaM^{3+}Si_2O_6$ clinopyroxenes plotted vs. Shannon Ionic Radius of the M^{3+} cation: $NaVSi_2O_6$ (this study), C2/c-$NaTiSi_2O_6$ (Ullrich et al. 2008), kosmochlor (Origlieri et al. 2003), aegirine (Downs and Singh 2006), and jadeite (Nestola et al. 2006).

Appendix F

Table of Irradiated Samples

UNILAC

2007

Material	Probe	Orient.	Ion	Fluenz [Ionen/cm²]	Energie [MeV/u]	dE/dx [keV/nm]	Strahlzeit
Titanit	SED4X02		^{208}Pb	1e11	11.1	15	03/2007
Apatit	DUR17B-H/1	(10-10)	^{128}Xe	1e11	11.1	18	09/2007
	DUR17B-H/1	(10-10)	^{128}Xe	5e11	11.1	18	09/2007
	DUR17B-H/1	(10-10)	^{128}Xe	1e12	11.1	18	09/2007
	DUR17B-H/1	(10-10)	^{128}Xe	5e12	11.1	18	09/2007
	DUR17B-H/1	(10-10)	^{128}Xe	1e13	11.1	18	09/2007
Cordierit	COR01		^{128}Xe	1e8	11.1	15	09/2007
	COR01		^{128}Xe	1e9	11.1	15	09/2007
	COR01		^{128}Xe	1e10	11.1	15	09/2007
	COR01		^{128}Xe	1e12	11.1	15	09/2007
	COR01		^{238}U	1e10	10.1	25	06/2007
	COR01		^{238}U	5e10	10.1	25	06/2007
	COR01		^{238}U	1e11	10.1	25	06/2007
	COR01		^{238}U	7e11	10.1	25	06/2007
Cordierit Keramik	CoKe01		^{238}U	1e10	10.6	22	06/2007
	CoKe01		^{238}U	5e10	10.6	22	06/2007
	CoKe01		^{238}U	1e11	10.6	22	06/2007
	CoKe01		^{238}U	7e11	10.6	22	06/2007

2008

Material	Probe	Orient.	Ion	Fluenz [Ionen/cm²]	Energie [MeV/u]	dE/dx [keV/nm]	Strahlzeit
Apatite	DUR09-X	(0001)	^{197}Au	6e11	11.1		08/2008
	DUR09-H	(10-10)	^{197}Au	6e11	11.1		08/2008
	DUR09-H	(10-10)	^{197}Au	1e12	11.1		08/2008
	DUR09-H	(10-10)	^{197}Au	6e11	11.1		08/2008
	DUR21-H	(10-10)	^{197}Au	1e12	11.1		08/2008
	DUR21-H	(10-10)	^{197}Au	6e11	11.1		08/2008
	DUR21-H	(10-10)	^{197}Au	1e12	11.1		08/2008
Cordierit	CORMB1	(100)	^{208}Pb	2e11	8	25	01/2008
	CORMB1	(100)	^{208}Pb	5e11	8	25	01/2008
	CORMB1	(100)	^{208}Pb	7e11	8	25	01/2008
	CORMB1	(100)	^{208}Pb	1e12	8	25	01/2008
	CORMB1	(100)	^{208}Pb	2e12	8	25	01/2008
	CORTS1	(100)	^{197}Au	6e11	11.1	23	04/2008
	CORTS1	(100)	^{197}Au	2e12	11.1	23	04/2008
	CORTS2	(010)	^{197}Au	6e11	11.1	23	04/2008
	CORTS2	(010)	^{197}Au	2e12	11.1	23	04/2008
	CORTS3	(001)	^{197}Au	6e11	11.1	23	04/2008
	CORTS3	(001)	^{197}Au	2e12	11.1	23	04/2008
	CORMB1	(100)	^{64}Ni	2e12	11.1	5	09/2008

2009

Material	Probe	Orient.	Ion	Fluenz [Ionen/cm²]	Energie [MeV/u]	dE/dx [keV/nm]	Strahlzeit
Cordierit	CORD#126231	(100)	^{197}Au	1e12	11.1	24	02/2009
	CORD#133770	(100)	^{197}Au	1e12	11.1	24	02/2009
	CORDTS3_X1	(100)	^{197}Au	1e12	11.1	24	02/2009
	CORDTS3_X2	(100)	^{197}Au	1e12	11.1	24	02/2009
	CORDTS3_C	(001)	^{197}Au	1e12	11.1	24	02/2009
Rubin			^{197}Au	1e10 1e11 1e12 5e12	11.1	35	03/2009

SIS

2007

Material	Probe	Orient.	Druck [GPa]	Ion	Fluenz [Ionen/cm^2]	Energie [MeV/u]	dE/dx0 [keV/nm]	Zelle	Strahlzeit
Titanit	SED4X01	(100)		^{208}Pb	1e11	164	20	UAG3	03/2007
	SED1X05	(100)	4 GPa	^{208}Pb	1e11	164	20	UAG1	03/2007
	SED1X04	(100)	6.3 GPa	^{208}Pb	1e11	164	20	UAG4	03/2007
	SED2X01	(100)	10.5 GPa	^{208}Pb	1e11	164	20	UAG2	03/2007
	SED1X06	(100)	6.5 – 7 GPa	^{208}Pb	1e11	164	20	ETH007	03/2007
	SED2X02	(100)	12.2 – 14 GPa	^{208}Pb	1e11	164	20	ETH000	03/2007
	SED2	(100)	-	^{238}U	1.5e11	178	22	UAG3	06/2007
	SED2	(100)	2.8 - 3.1 GPa	^{238}U	1.5e11	178	22	UAG2	06/2007
	SED2	(100)	2.7 - 3.5 GPa	^{238}U	1.5e11	178	22	UAG4	06/2007
	SED1	(100)	2.7 GPa	^{238}U	1.5e11	178	22	UAG1	06/2007
	SED1	(100)	*11.9 GPa*	^{238}U	1.5e11	178	22	ETH000	06/2007
Cordierit	COR02	(100)	-	^{238}U	1.5e11	178	20	UAG3	06/2007
	COR02	(100)	4.8 GPa	^{238}U	1.5e11	178	20	ETH007	06/2007
Apatit	KOL1	(10-10)	8.8 GPa	^{208}Pb	2e11	195	25	ETH007	07/2007
	KOL2	(0001)	8.8 GPa	^{208}Pb	2e11	195	25	ETH007	07/2007
	KOL1	(10-10)		^{208}Pb	2e11	195	25	UAG4	07/2007
	KOL2	(0001)		^{208}Pb	2e11	195	25	UAG4	07/2007

2008

Material	Probe	Orient.	Druck [GPa]	Ion	Fluenz [Ionen/cm²]	Energie [MeV/u]	dE/dx0 [keV/nm]	Zelle	Strahlzeit
Cordierit	CORMB1	(100)	9.15	^{124}Xe	1e12	155	12	UAG2	03/2008
	CORMB1	(100)	2.55	^{124}Xe	1e12	155	12	UAG4	03/2008
	CORMB1	(100)	5.4	^{124}Xe	1e11	155	12	ETH007	03/2008
	CORMB1	(100)	8.1	^{238}U	3.7e12	178	15	UAG2	05/2008
	CORMB1	(100)	4.65	^{238}U	1e12	178	15	UAG4	05/2008
	CORMB1	(100)	-	^{238}U	3.7e12	178	15	ETH007	05/2008
cBN	cBN anvil		-	^{124}Xe	2.15e12	200		-	03/2008
Apatite	DUR17-1B/H	(10-10)	3.6	^{124}Xe	1e11	155	18	UAG1	03/2008
	DUR17-1B/H	(0001)	3.6	^{124}Xe	1e11	155	18	UAG1	03/2008
	DUR17-1B/H	(10-10)	11.5	^{124}Xe	1e12	155	18	ETH000	03/2008
	DUR17-1B/H	(0001)	11.5	^{124}Xe	1e12	155	18	ETH000	03/2008
Zircon	Zircon in silicon		~6	^{132}Xe	2e12	340		PE Presse	07/2008

2009

Material	Probe	Orient.	Druck [GPa]	Ion	Fluenz [Ionen/cm²]	Energie [MeV/u]	dE/dx0 [keV/nm]	Zelle	Strahlzeit
Apatit	DUR17B-H	(0001) (10-10)	4.91	^{238}U	1e12	175	20	UAG1	09/2009
	DUR17B-H	(10-10)	-	^{238}U	1e12	175	20	½ UAG2	09/2009
HOPG	+ 1e18 H+ / cm2	(0001)	4.95	^{197}Au	5e11	144	15	UAG2	02/2009
	+ 1e18 H+ / cm2	(0001)	7.00	^{197}Au	5e11	144	15	UAG4	02/2009
	+ 1e18 H+ / cm2	(0001)	4.95	^{197}Au	+5e11	144	15	UAG2	03/2009
	+ 1e18 H+ / cm2	(0001)	7.00	^{197}Au	+5e11	144	15	UAG4	03/2009
Zircon	ORNL2002		~7 GPa	^{197}Au	5e11	350	25	PE II	02/2009